TÉCNICO LISBOA

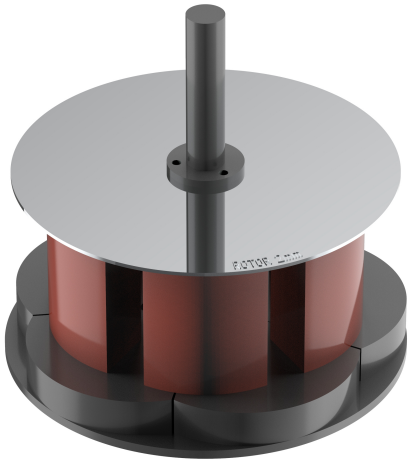

Electromagnetic Design Improvements of the Single-Sided Disk-Rotor Induction Motor for the FST In-Wheel Traction

Nuno Miguel Santos Silva Macara

Thesis to obtain the Master of Science Degree in

Electrical and Computer Engineering

Supervisor(s): Prof. Paulo José da Costa Branco
IDMEC Researcher Francisco Ferreira da Silva

Examination Committee

Chairperson: Prof. Célia Maria Santos Cardoso de Jesus
Supervisor: Prof. Paulo José da Costa Branco
Member of the Committee: Prof. Luís Guilherme Barbosa Rolim

September 2021

Declaration

I declare that this document is an original work of my own authorship and that it fulfills all the requirements of the Code of Conduct and Good Practices of the Universidade de Lisboa.

To all who made me who I am.

Acknowledgments

A special thanks to my supervisors, Professor Paulo Branco and Master Francisco Silva, and the Electrical Machine's Laboratory team for all the help and time invested in me and my project.

To my family and friends who supported me during this endeavor, thank you so much, without their support none of this could have happened. To João, thank you for all your knowledge and lunch breaks company, and to my other discord friends for the emotional support.

Finally, to my parents and my grandparents for raising me this way, and paving the way to all my successes, and to my brother and sister for laughing at my jokes. To all who made me who I am,

Thank you.

Resumo

Com o aumento da popularidade de veículos elétricos e a necessidade de máquinas mais eficientes, a otimização dos motores elétricos é muito importante. O objetivo desta tese consiste na caracterização exata de uma máquina de indução axial, seguida da elaboração de um modelos de elementos finitos da máquina. Esta máquina foi desenhada como motor ”in-wheel” de um automóvel elétrico.

Após o desenvolvimento do modelo físico, vários testes eletromagnéticos foram realizados, e a geometria da máquina otimizada. O comportamento térmico da máquina também foi medido experimentalmente, e depois modelado de acordo com os dados.

Os resultados obtidos demonstram uma melhoria na prestação eletromagnética da máquina, apesar da pouca eficiência global, sendo o torque produzido muito inferior ao requerido. Porém, o modelo FEM demonstrou ser muito preciso em simulações estacionárias, e a sua aplicação muito promissora noutros tipos diferentes de máquinas.

Palavras-chave: Máquina indução; Geometria axial; Rotor em disco; Modelação de máquinas elétricas; Fluxo magnético; Correntes induzidas

Abstract

With the increase in popularity of electrical vehicles and the need for more efficient machines, the optimization of electrical motors is of great importance. The aim of this thesis is to accurately characterize an axial induction machine, followed by the development of a finite element method model of the machine. This induction machine is intended to be an in-wheel motor for a vehicle.

After the development of the model, several electromagnetic tests were performed, and the machine's geometry was optimized. The thermal behavior of the machine was also measured experimentally, and a thermal model of the machine was created.

The results obtained show an improvement in the electromagnetic performance of the machine, despite its overall inefficiency for its purpose, with a much lower torque than needed. However, the FEM model proved to be very accurate for stationary simulations, and its application also very promising in different types of machine.

Keywords: Induction machine; Axial geometry; Disk rotor; Electrical machines' modelling; Magnetic flux; Induced currents

Contents

List of Tables

List of Figures

Nomenclature

Greek symbols

α'	Temperature coefficient.
α	Used parameter for the vector potential solution equation calculation.
δ	Skin depth.
μ	Magnetic permeability.
μ_0	Magnetic permeability of free space.
μ_{eq}	Equivalent relative permeability.
μ_r	Magnetic relative permeability.
ω	Angular frequency.
ϕ	Magnetic flux.
Ψ	Magnetic flux linkage.
ρ'	Density.
ρ	Electrical resistivity.
σ	Electrical conductivity.
τ	Torque.
θ	Cylindrical angle coordinate.
φ	Phase difference.

Roman symbols

$\mathbf{A}$	Magnetic vector potential.
$\mathbf{B}$	Magnetic flux density vector.
$\mathbf{D}$	Displacement current vector.
$\mathbf{E}$	Electrical field vector.

$\mathbf{F}$	Lorentz force vector.
$\mathbf{H}$	Magnetic field strength vector.
$\mathbf{I}$	Current vector.
$\mathbf{J}$	Current density vector.
$\mathbf{v}$	Velocity vector.
$\mathbf{v}_\mathsf{x}$	Velocity vector.
$\mathbf{e}_{coil}$	Coil mean path direction unity vector.
$\mathbf{q}$	Conductive heat flux.
a, b, c	Orthogonal coordinates.
B_{eff}	RMS flux density.
H_{eff}	RMS field strength.
H_{eq}	Equivalent field strength.
J_e	Stator linear current density.
J_m	Stator linear current density amplitude.
k	Thermal conductivity.
P	Power.
P_{Joule}	Joule losses.
P_{mech}	Mechanical power.
Q	Heat.
r	Cylindrical radius coordinate.
T	Sinusoidal wave period.
V	Volume.
V_m	Magnetic scalar potential.
W_m	Magnetic energy.
z	Cylindrical height coordinate.
$\jmath$	Imaginary number: $\sqrt{-1}$
$\mathbf{u}_\mathsf{x}$	Unity vector with x axis direction.
$\mathbf{u}_\mathsf{y}$	Unity vector with y axis direction.

$\mathbf{u}_z$ Unity vector with z axis direction.

C_1 Coefficient 1 of the vector potential solution equation.

C_2 Coefficient 2 of the vector potential solution equation.

C_p Heat capacity.

e Nepper number.

F_{mm} Magnetomotive force.

h Rotor height.

h_d Linear stator tooth height.

I Phase current amplitude.

i Current.

i_A Phase A current.

i_B Phase B current.

i_C Phase C current.

L Coil inductance.

l Length.

L_d Horizontal distance between linear stator teeth.

n Number of coils per phase.

N_t Coil number of turns.

R Electrical resistance.

s Characteristic equation solution.

S, *S* Area.

T Temperature.

t Time.

u Voltage.

x Horizotal distance.

Subscripts

x, y, z Cartesian components.

rms Root mean square.

Chapter 1

Introduction

1.1 Motivation

As society shifts into a more efficient and sustainable world, the need for electrical machines has never been greater, so new types of machines with different geometries have been created. These new machines tend to be smaller and more efficient, as electrical vehicles become more popular. The induction machine, due to its simplicity, is the most used type of electrical machine.

So, in 2017 student João Guilherme designed and modelled an axial flux induction machine for the formula student electric vehicle competition, [1]. The motor's purpose was the propulsion of the electrical car, and intended to drive each wheel independently, using a total of 4 motors. This way, each motor can produce only 25% of the total power, and therefore can be smaller than one single large motor. As axial machines are shorter than "normal" ones, this type of design is ideal for this use, as the motors can be mounted inside the wheels, visible in fig. 1.1.

Figure 1.1: Protean in-wheel 100 HP electric motor [2].

With the competition rules and the desired performance specifications for the vehicle, table 1.1, it was calculated each motor nominal torque to be 208,35 Nm, for a 20 cm rotor diameter. Each motor would be powered by independent 3-phase 50 Hz sinusoidal currents, and all motors to be 1 pair of poles machines.

Maximum velocity	120 km/h
Maximum acceleration	9,26 m/s^2
Vehicle mass	300 kg

Table 1.1: Vehicle specifications.

After the motor specifications created, both a mathematical and a physics simulation model were developed for the motor. The electromagnetic performance of the machine was analyzed, and then compared between both mathematical and simulation models. Due to the high complexity of the physics model, FEM, these simulations were only performed with a blocked rotor in the frequency domain. Figure 1.2 plots the comparison between both models, and both models show a very similar behavior. However, the results are far from the desired torque for the machine, 208,25 Nm. This difference mainly comes from the type of simulation, as the blocked rotor test transfers no torque to the axle, as the name indicates, the rotor is blocked.

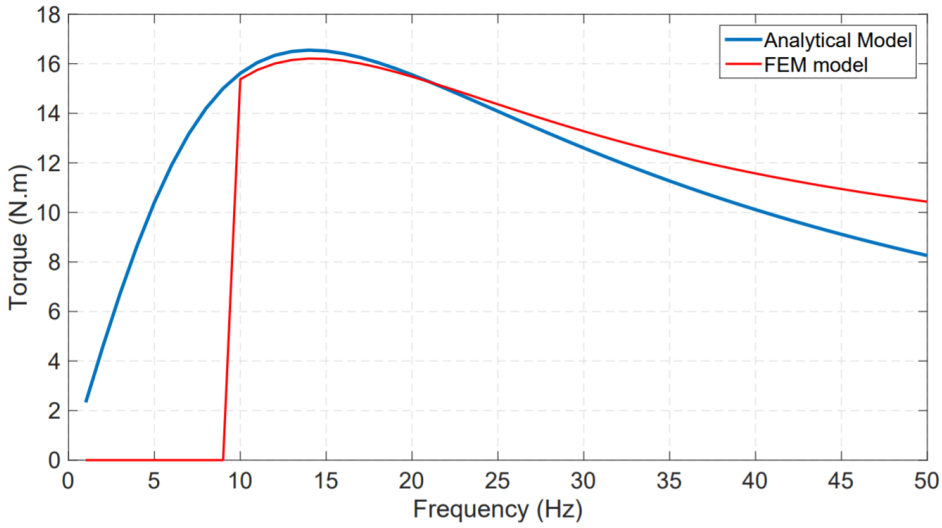

Figure 1.2: Torque/Frequency response with blocked rotor, for both analytical and FEM models.

Due to this, time-dependent tests were made, however the results also proved to be unsatisfying, with the final conclusion being the machine not working for its main purpose: the propulsion of the electrical vehicle. However, this motor could serve other applications, where the torque needed is lower. So, in 2019 student Francisco Fernandes built and tested the physical machine, [3] and fig. 1.3. The machine used the same geometry developed in [1], and a very promising new type of material, the Somaloy® soft composite metal alloy.

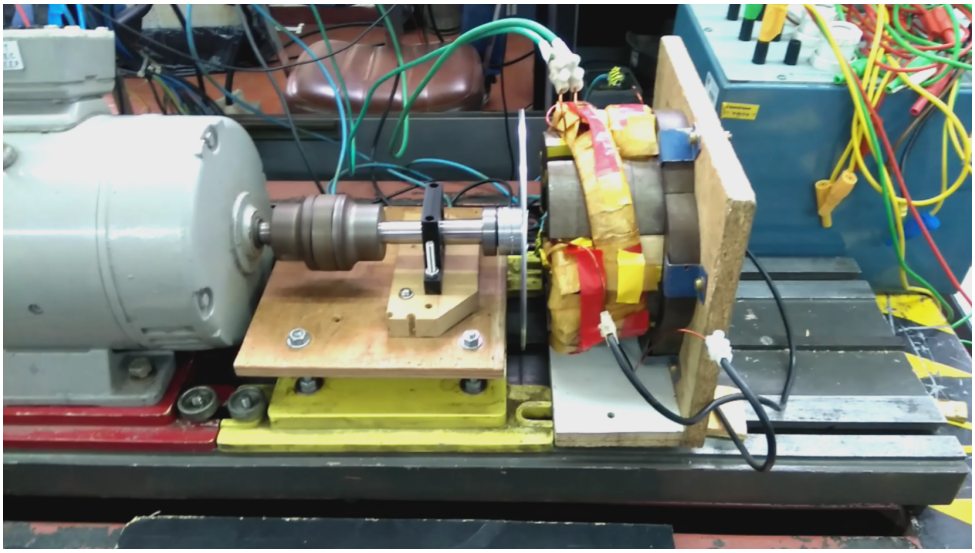

Figure 1.3: Axial induction motor test setup at IST's electrical machines' laboratory [3].

After the machine was built, it was tested in the electrical machines' laboratory at Instituto Superior Técnico in Lisbon, and the results showed the motor performance to be very low, much lower than the theoretical simulations. The source for this low performance is not trivial, since both models developed in [1] considered perfect materials and conditions, whereas in reality this does not occur. Due to this, a deeper analysis of this machine was necessary to better comprehend it.

1.2 Objectives

The aim of this master thesis is to better characterize the axial induction motor, and to develop a new accurate finite element method model of the machine. The machine is analyzed through a series of electromagnetic experiments, and with the data a new 3D FEM model will be created. This model will allow more complex simulations, and consequently the acquisition of more complete data. This data will then be used to optimize and further comprehend the full behavior of the machine. The thermal behavior of the machine will also be experimentally measured and a new thermal FEM model will be designed.

1.3 Thesis Outline

Chapter 2 contains the theoretical background behind the functioning of the machine. It begins with the description of the simplified linear model of the machine, followed by the electromagnetic principles behind the functioning of the motor. After, the analytical model of the linear motor is explained and solved, and a few preliminary simulations are solved with this model to better comprehend and visualize the electromagnetic quantities involved in the machine.

Chapter 3 describes the characterization process of the stator of the machine. Firstly, the motives for this characterization are presented, and the experimental process is outlined. Then with the experimental data, the magnetic curve for the stator is calculated and then compared with the manufacturer's data. This curve is of great importance to create an accurate FEM model.

Chapter 4 focuses on the development of the FEM model of the machine and the physics involved in the model. It also describes the types of studies used, and their particularities. Chapter 5 presents the validation steps of the model. After the experiments are outlined, both experimental and simulated data is compared, and finally the simulation model parameters are adjusted, and the final model is validated.

Chapter 6 presents the simulations obtained with the physics model. These simulations include both stationary and rotary studies, in the frequency and time domains. Different stator, coil and rotor geometries are then simulated and some preliminary conclusions about the motor are drawn. Chapter 7 shows the thermal experimental results of the machine, both experimental and model simulations. The laboratory experiment is presented and, similarly to chapter 5, the FEM model is created with and adjusted with the experimental data.

Finally, chapter 8 summarizes the work done during the thesis and presents the drawn conclusions. It also suggests the next steps for the future work with motor, and how it can be improved.

Chapter 2

Theoretical Background

2.1 Linear model

In the first work, [1], the induction motor was designed and modelled in a steady-state, and then it was built and tested in the Electrical Machines Laboratory, [3]. However, with several discrepancies in behavior, a new model is desirable. So the first step for this model is a simple mathematical model.

With the motor being cylindrical and with an axial symmetry, the mathematical model for this exact configuration would be very complex, as a cylindrical coordinate system is better than an orthogonal *a,b,c* system. Figure 2.1 shows both the cylindrical motor and both coordinate systems.

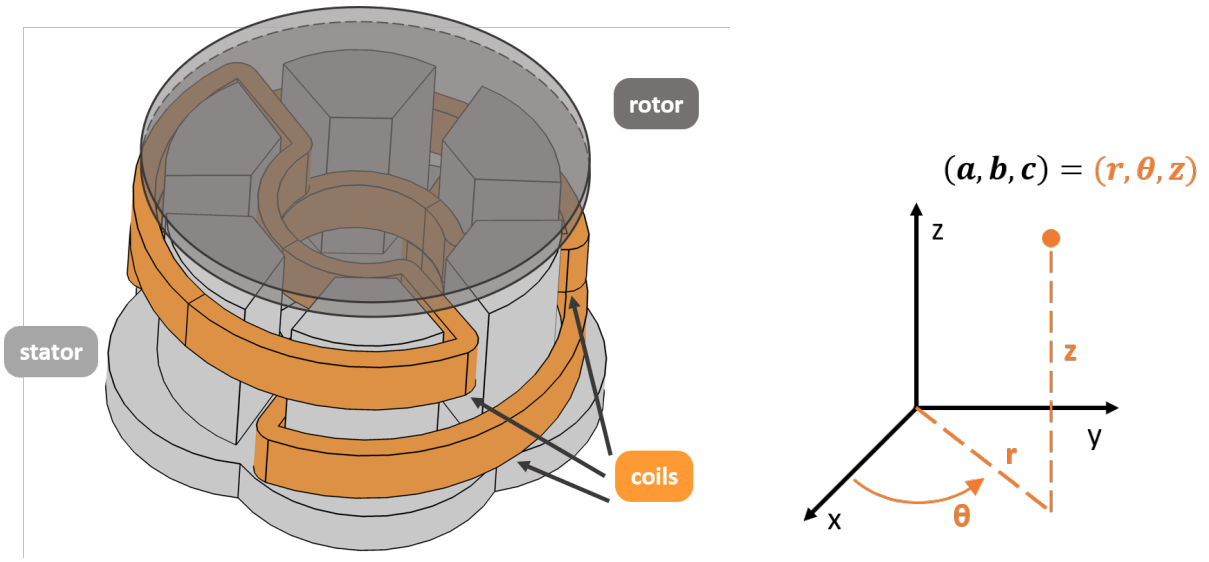

(a) cylindrical motor model

(b) cylindrical and orthogonal coordinate systems

Figure 2.1: (a) Geometrical model representation of the cylindrical axial-flux induction machine, (b) coordinate systems.

Using the new cylindrical coordinate system, the axial-induction machine can be approximated by a linear one, fig. 2.2, where the cylindrical coordinates are transformed into new orthogonal ones. This new machine has now a linear stator with 6 teeth and 3 coils, the same as the real circular motor, and a rectangular rotor with the same length. In this new model, the depth of all components is the same.

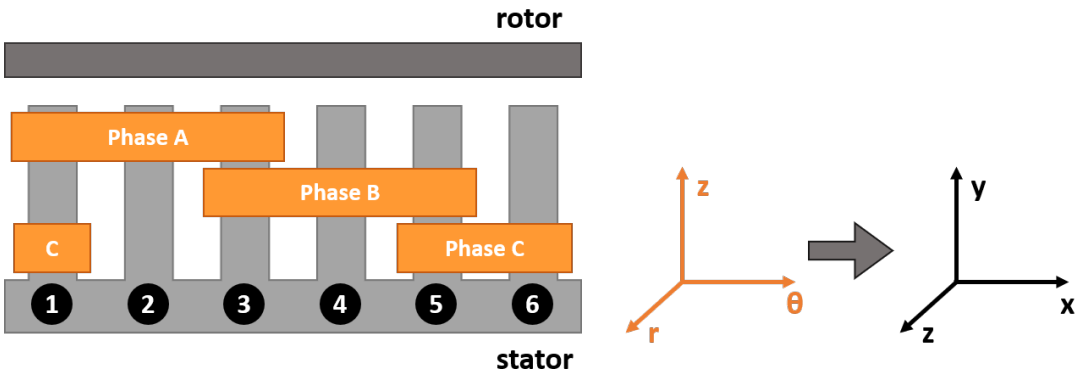

Figure 2.2: Equivalent linear motor and new coordinate system.

Now, with this linear representation, a simplified mathematical model can be created more easily. This model however will not be an exact model due to all made assumptions, instead, it is a qualitative electromagnetic model, whose purpose is to show the main characteristics present in the motor.

2.2 Electromagnetic Principles

This induction motor is composed of 3 main components: the stator, the coils, and the rotor. These components work together to create a rotating force, torque, that will drive a load. The functioning principle of every induction motor is the same, fig. 2.3: a stator made of a ferromagnetic material is surrounded by electromagnetic coils; when an alternating current, $\mathbf{I}$, circulates through the coils, it creates a rotating magnetic flux density in the stator, $\mathbf{B}$, will induce an electric current density inside the rotor, $\mathbf{J}$. The interaction between the magnetic flux density and the induced current density will generate a force, $\mathbf{F}$, *Lorentz force* [4].

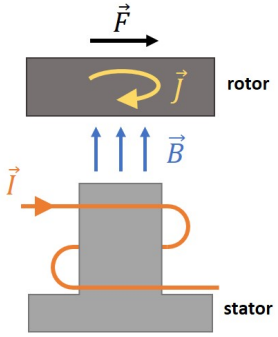

Figure 2.3: Induction machine principle.

With a linear machine considered, some further considerations need to be made as to simplify the analytical model. These considerations are both related to the geometry of the machine and the electromagnetic quantities present. This model was based on the linear motor developed in [5].

The first consideration regards the air gap of the machine, as it is supposed to be as small as possible, the machine is modelled with no magnetic leakage.

The second assumption made considers the magnetic flux density generated by the stator decays completely inside the rotor disk. This will cause the rotor top surface to have no flux and consequently no induced currents. This approximation and the previous ones then cause the machine to have no magnetic leakage, which is not true; despite this, it causes the model to be much simpler, as both together create the boundary conditions necessary to solve the analytical model, section 2.3.3.

The third consideration regards the coil positioning in between the stator teeth. In the linear stator model, represented in fig. 2.4, the coil windings are distributed along the z-axis, so the current density inside them is also assumed to be in the same axis. Due to this, we consider the rotor induced currents to have the same orientation, and therefore are no *x* and *y* components, eq. (2.1a). As a consequence, the magnetic field and flux density in the rotor at the same *z* coordinate are also zero, eq. (2.1b),

$$J_x = 0, J_y = 0 \tag{2.1a}$$

$$H_z = 0 \Rightarrow B_z = 0. \tag{2.1b}$$

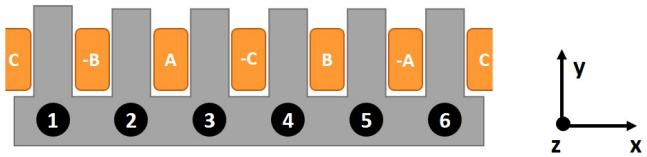

Figure 2.4: Linear stator with coil orientation.

The final consideration regards the stator of the machine. This stator is then reduced to an equivalent rectangular block, and the stator current is then represented by a current slab at its top surface. This new equivalent current density, eq. (2.42) is resultant from the 3-phase currents inside the coils. J_e is then a travelling wave with electrical frequency ω, and k the machine's wavenumber,

$$J_e = J_m \cdot e^{j(\omega t - \mathrm{kx})} \tag{2.2}$$

2.3 Analytical Model

2.3.1 Bi-dimensional model

Due to all the considerations made, the *z*-axis component of both magnetic field and flux density is null, simplifying the model. Consequently, with no magnetic *z* component, the rotor developed electromagnetic force will also not have this component as well. This will cause the machine's torque to have only *x* and *y* components, as seen in eqs. (2.3a) to (2.3c):

$$\mathbf{F} = \mathbf{J} \times \mathbf{B} \tag{2.3a}$$

$$\mathbf{J} \times \mathbf{B} = \underbrace{(J_y B_z - J_z B_y)}_{F_\mathrm{x}}\mathbf{u_x} \; + \; \underbrace{(J_z B_x - J_x B_z)}_{F_\mathrm{y}}\mathbf{u_y} \; + \; \underbrace{(J_x B_y - J_y B_x)}_{F_\mathrm{z}}\mathbf{u_z} \tag{2.3b}$$

$$\mathbf{F} = -J_z B_y \; \mathbf{u_x} \; + \; J_z B_x \; \mathbf{u_y}. \tag{2.3c}$$

With a null component for the rotor developed force, the z component of the velocity created by it is also null, and consequently the only quantity with a *z*-axis component is the current density. As a result, all values will only depend on both *x* and *y* components, as well as the time, *t*, which refers to the time instant after the system's initial conditions.

2.3.2 Vector potential

The first step towards solving the electromagnetic model is defining the magnetic field distribution in the rotor. For this we use the magnetic vector potential concept, [6], as to better define the magnetic field density $\mathbf{B}$, eq. (2.4),

$$\mathbf{B} = \nabla \times \mathbf{A} \tag{2.4}$$

From this concept now the magnetic field intensity $\mathbf{H}$, defined through the constitutive relation in eq. (2.5a), can be written with the help of eq. (2.4), in eq. (2.5b)

$$\mathbf{B} = \mu \mathbf{H} \tag{2.5a}$$

$$\mathbf{H} = \frac{\nabla \times \mathbf{A}}{\mu}. \tag{2.5b}$$

The current density $\mathbf{J}$, obtained through the Ampère's Law, eq. (2.6a), is also defined with eq. (2.5b) in eq. (2.6b)

$$\mathbf{J} = \nabla \times \mathbf{H} \tag{2.6a}$$

$$\mathbf{J} = \frac{\nabla \times \nabla \times \mathbf{A}}{\mu}. \tag{2.6b}$$

With the current density and magnetic field defined, the force density in the rotor in eq. (2.3a) can be rewritten as eq. (2.7)

$$\mathbf{F} = \mathbf{J} \times \nabla \times \mathbf{A}. \tag{2.7}$$

Vector Potential distribution

To obtain the vector potential distribution in the rotor, it needs to be defined as a function of the independent variables: time and position, *t*, *x* and *y*. As a starting point, the Maxwell differential equations for a quasi-static system are defined in eq. (2.8a) to eq. (2.8d)

$$\nabla \times \mathbf{H} = \mathbf{J} \tag{2.8a}$$

$$\mathbf{J} = \sigma[\mathbf{E} + (\mathbf{v} \times \mathbf{B})] \tag{2.8b}$$

$$\nabla \times \mathbf{E} = -\frac{\partial \mathbf{B}}{\partial t} \tag{2.8c}$$

$$\nabla \cdot \mathbf{B} = 0. \tag{2.8d}$$

With the vector potential definition in eq. (2.4) the electric field in eq. (2.8c) can be written as eq. (2.9)

$$\mathbf{E} = \frac{\partial \mathbf{A}}{\partial t}, \tag{2.9}$$

Equation (2.8a) with the help of the relation eq. (2.10a), is reduced to

$$\nabla \times \nabla \times \mathbf{A} = \nabla(\nabla \cdot \mathbf{A}) - \nabla^2 \mathbf{A} \tag{2.10a}$$

$$\frac{1}{\mu}[\nabla(\nabla \cdot \mathbf{A}) - \nabla^2 \mathbf{A}] = \mathbf{J} \tag{2.10b}$$

In every electromagnetic system, according to eq. (2.8d), the magnetic flux density divergence is always null, and consequently, the vector potential divergence in said system will also be null, eq. (2.11a). With this simplification, eq. (2.10b) can be reduced to

$$\nabla \cdot \mathbf{A} = 0. \tag{2.11a}$$

$$-\frac{\nabla^2 \mathbf{A}}{\mu} = \mathbf{J}. \tag{2.11b}$$

The vector potential distribution equation, the one modelling the system, can now be obtained through by replacing eq. (2.4), eq. (2.11a) and eq. (2.11b) in eq. (2.8b). Equation (2.12) characterize this distribution,

$$\frac{\nabla^2 \mathbf{A}}{\mu\sigma} = \frac{\partial \mathbf{A}}{\partial t} - \mathbf{v} \times (\nabla \times \mathbf{A}). \tag{2.12}$$

Equation (2.12) can also be simplified further when considering the assumptions made in section 2.2 and the model geometry itself. With no *z* component for the flux density in the rotor, $\mathbf{B}$ can be written as eq. (2.13),

$$\mathbf{B} = \frac{\partial A_z}{\partial y}\,\mathbf{u_x} - \frac{\partial A_z}{\partial x}\,\mathbf{u_y}. \tag{2.13}$$

Furthermore, with null x and y components of the potential vector, it can be reduced to only its z-axis component, eq. (2.14), further simplifying eq. (2.12).

$$A_x = 0\,, A_y = 0 \;\rightarrow\; \mathbf{A} = A_z\,\mathbf{u_z} \tag{2.14}$$

Finally, the potential vector distribution can be reduced to eq. (2.15) depending only on the position coordinates, *x* and *y*, time, *t*, and velocity, v_x; the last being a function of the position and the time as well.

$$\frac{\partial^2 A_z}{\partial x^2} + \frac{\partial^2 A_z}{\partial y^2} - \mu\sigma v_x \frac{\partial A_z}{\partial x} - \mu\sigma \frac{\partial A_z}{\partial t} = 0 \tag{2.15}$$

Solution to vector potential equation

With the vector potential distribution defined in eq. (2.15), the other quantities can now be obtained,$\mathbf{B}$, $\mathbf{H}$, $\mathbf{J}$ and $\mathbf{F}$. This vector potential distribution can be assumed to have a similar distribution to magnetic flux density and stator current density, eq. (2.42), so it can be written in a similar form, eq. (2.16)

$$A_{\mathsf{z}}(\mathsf{x},\mathsf{y},t) = \hat{A}(\mathsf{y})\, \mathsf{e}^{\jmath(\omega t - k\mathsf{x})} \tag{2.16}$$

Based on this new equation form, the partial derivatives in eq. (2.15) can be replaced by eq. (2.17a) to eq. (2.17d).

$$\frac{\partial^2 A_{\mathsf{z}}}{\partial \mathsf{x}^2} = -\mathsf{k}^2 \hat{A}\, \mathsf{e}^{\jmath(\omega t - \mathsf{kx})} \tag{2.17a}$$

$$\frac{\partial^2 A_{\mathsf{z}}}{\partial \mathsf{y}^2} = \frac{\partial^2 \hat{A}}{\partial \mathsf{y}^2}\, \mathsf{e}^{\jmath(\omega t - \mathsf{kx})} \tag{2.17b}$$

$$\frac{\partial A_{\mathsf{z}}}{\partial \mathsf{x}} = -\jmath \mathsf{k}\, \hat{A}\, \mathsf{e}^{\jmath(\omega t - \mathsf{kx})} \tag{2.17c}$$

$$\frac{\partial A_{\mathsf{z}}}{\partial \mathsf{x}} = -\jmath \mathsf{k}\, \hat{A}\, \mathsf{e}^{\jmath(\omega t - \mathsf{kx})}. \tag{2.17d}$$

Now, replacing the new partial derivatives in eq. (2.15) and eliminating the common factor $e^{j(\omega t - kx)}$ we have the simplified eq. (2.18),

$$\frac{\partial^2 \hat{A}}{\partial \mathsf{y}^2} - [\mathsf{k}^2 + \jmath\mu\sigma(\omega - \mathsf{kv_x})]\hat{A} = 0. \tag{2.18}$$

Equation (2.18) is now a second order derivative equation, whose characteristic equation is the following, eq. (2.19).

$$s^2 - [\mathsf{k}^2 + \jmath\mu\sigma(\omega - \mathsf{kv_x})] = 0. \tag{2.19}$$

By substituting the 0 degree coefficient by α^2, eq. (2.19) can be written as eq. (2.20), and finally eq. (2.21). The roots of this equation are then α and $-\alpha$.

$$s^2 - \alpha^2 = 0 \tag{2.20}$$

$$\alpha = \sqrt{\mathsf{k}^2 + \jmath\mu\sigma(\omega - \mathsf{kv_x})}. \tag{2.21}$$

Equation (2.18) general solution will then have the form eq. (2.22). Coefficients C_1 and C_2 values have now to be calculated from the model's boundary conditions.

$$\hat{\mathbf{A}}(y) = C_1 e^{\alpha y} + C_2 e^{-\alpha y} \tag{2.22}$$

$$\mathbf{A} = (C_1 e^{\alpha y} + C_2 e^{-\alpha y})\, \mathbf{e}^{\,j(\omega t - kx)}\ \mathbf{u_z}. \tag{2.23}$$

2.3.3 Boundary conditions

With the vector potential distribution equation defined, the last step for solving it is the model's boundary conditions. These are a set of conditions that model the electromagnetic behavior of the system, and, in this case, 2 boundary conditions are necessary to solve eq. (2.23). These conditions come from the two first simplifications in the section 2.2, at the rotor's bottom and top surfaces. With 2 unknown constants in the vector potential distribution equation, C_1 and C_2, at least 2 boundary conditions are needed.

First boundary condition: *y* = 0

The first boundary condition is then at *y*=0, the boundary between the stator and the rotor, the air-gap of the linear motor is neglected, as we want its thickness to be the smallest. When compared to the other dimensions, stator and rotor thickness, the air-gap is much smaller. In this surface we already now the value of the current density here, J_e as it was characterized in eq. (2.42).

Despite knowing the current density in the stator's top surface, we do not know its distribution inside the rotor. At *y*=0, $\mathbf{H}$ can be obtained through Ampère's circuital law in the integral form, eq. (2.24)

$$\oint \mathbf{H} \cdot d\mathbf{l} = \int_S \mathbf{J} \cdot \mathbf{n}\, ds. \tag{2.24}$$

According to this law, any current density $\mathbf{J}$ crossing a section with area S creates a magnetic field with intensity $\mathbf{H}$ in a closed path, with length l. This law is now applied in the linear stator model, and fig. 2.5 shows the closed path [abcd] and the current density slab $\mathbf{J_e}$.

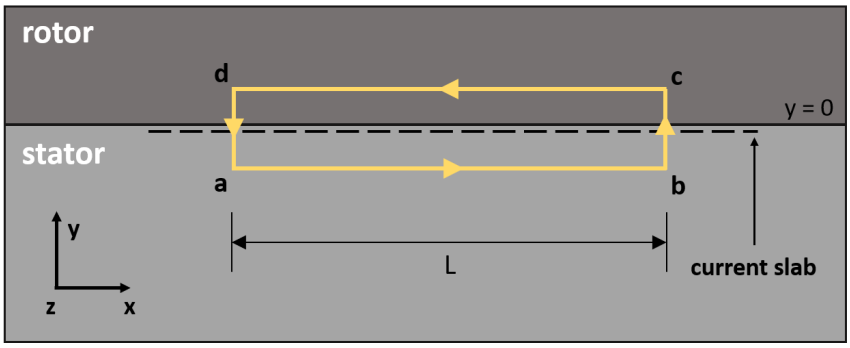

Figure 2.5: First boundary condition: y=0.

In fig. 2.5 we can see the current density slab imposed by the stator at the boundary, and the magnetic field path [abcd] involving it. The horizontal sections, [ab] and [cd] are, respectively, in the stator and rotor immediately below and above the boundary. The vertical sections [bc] and [da] are as small as needed when compared with the horizontal ones, and consequently, neglected. The length of the both horizontal sections is L. Now, applying circuital law along the [abcd] path, eq. (2.24), we have eq. (2.25)

$$\int_a^b H_{\mathsf{x}}\,\mathsf{dx} + \int_b^c H_{\mathsf{y}}\,\mathsf{dy} + \int_c^d H_{\mathsf{x}}\,\mathsf{dx} + \int_d^a H_{\mathsf{y}}\,\mathsf{dy} = \int_a^b J_{\mathsf{e}}\,\mathsf{dx} \tag{2.25}$$

Then, with the following considerations:

- the magnetic field's component associated with the vertical segments of the closed path can be neglected, due to having negligible lengths when compared with the horizontal paths
- as the magnetic permeability of the stator is much higher than the rotor's, the magnetic field's component associated with the bottom segment can be neglected
- the imposed current density only has a z component
- the path involves only the current density slab of the stator
- the horizontal paths' length L when compared with the imposed current wave length can be neglected, as it is much smaller, and consequently $\mathbf{H}_{\mathsf{z}}$ and $\mathbf{J}_{\mathsf{M}}$ can be considered constant, due to low variation

Equation (2.25) can be reduced to eqs.2.26a and 2.26b,

$$H_{\mathsf{x}}\,\mathsf{L} = J_{\mathsf{e}}\,\mathsf{L} \tag{2.26a}$$

$$B_{\mathsf{x}} = \mu J_{\mathsf{e}}. \tag{2.26b}$$

Taking into account eq. (2.13) and eq. (2.26b), we can now solve the vector potential distribution equation given by eq. (2.23) at y = 0, with C_1 and C_2 relation given by eqs.2.27a and 2.27b,

$$-\frac{\partial A_{\mathsf{z}}}{\partial \mathsf{y}}|_{(\mathsf{x},0,t)} = \mu J_m\, e^{j(\omega t - \mathsf{kx})} \tag{2.27a}$$

$$-\mathsf{C}_1 + \mathsf{C}_2 = \frac{\mu J_{\mathsf{m}}}{\alpha}. \tag{2.27b}$$

Second boundary condition: y = h

The second boundary condition for this model occurs at the rotor's top surface, where the magnetic field created by the stator, $\mathbf{H}$, is considered null. This condition is in fact a rough approximation, as there are no guaranties that this occurs as the magnetic permeability of the aluminum rotor and the air above is the same, 1, what causes the rotor to be invisible to the magnetic field, and consequently not affecting its normal decay.

However, this approximation is crucial for the modelling of the linear motor, as the only other possibility at this location, y = h, would be considering the magnetic field not decaying inside the rotor, only possible with an additional rotor ferromagnetic piece, [3]; this way, all the field would be ”pulled” by this piece and, consequently, not decaying inside the aluminum material. In our model, as we want to model a rotor without the additional ferromagnetic piece, the first approximation was the one considered, where $\mathbf{H}_y$=0 at y = h. In fig. 2.6 the second boundary condition is also solved with the Ampère's law, however now with a rectangular closed-loop way whose bottom and top sides are located immediately below the stator's generated current slab, and above the rotor's top surface, respectively.

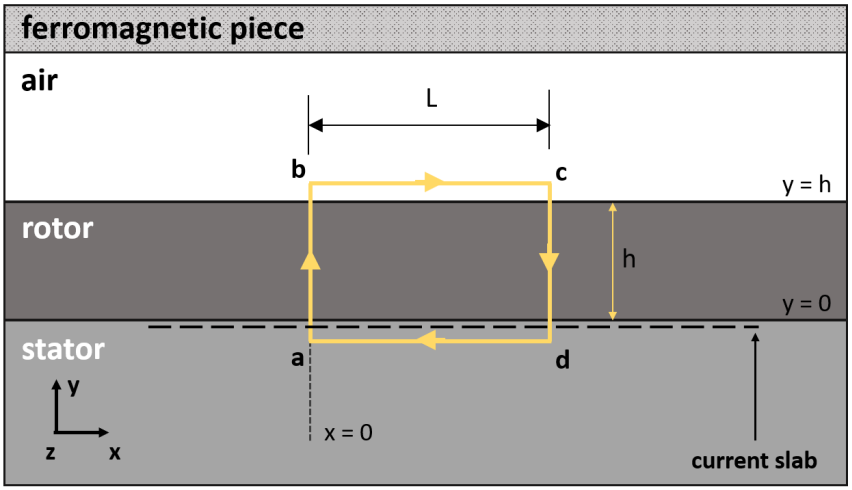

Figure 2.6: Second boundary condition: y=h.

Now, applying the Ampère's law in this path, and considering also $\mathbf{J}_z$ as the z-axis current density induced in the rotor we obtain eq. (2.28)

$$\int_a^b H_y \, dx + \int_b^c H_x \, dy + \int_c^d H_y \, dx + \int_d^a H_x \, dy = \int_a^d J_e \, dx + \int_S J_z \, dx \, dy. \tag{2.28}$$

Then, with the following considerations:

- the magnetic permeability of the stator is much higher than the rotor's, so its magnetic field can be neglected
- the magnetic field decays completely inside the rotor

Equation (2.28) can now be reduced to eq. (2.29):

$$\int_a^b H_y \, dx + \int_c^d H_y \, dx = \int_a^d J_e \, dx + \int_S J_z \, dx \, dy \tag{2.29}$$

However, as $\mathbf{H}_{y=h}$=0, $\mathbf{H}_y$ can be replaced in eq. (2.23), and consequently obtain the C_1 and C_2 relation, eqs. (2.30a) and (2.30b)

$$C_1\, e^{\alpha h} + C_2\, e^{-\alpha h} = 0 \tag{2.30a}$$

$$\frac{C_1}{C_2} = -e^{-2\,\alpha h}. \tag{2.30b}$$

With 2 relations found between the missing coefficients in eq. (2.23), C_1 and C_2 can now be obtained from eq. (2.31), presented in eq. (2.32),

$$\begin{cases} -C_1 + C_2 = \frac{\mu J_m}{\alpha} \\ \frac{C_1}{C_2} = -e^{-2\,\alpha h} \end{cases} \tag{2.31}$$

$$\begin{cases} C_1 = \frac{-J_m \cdot \mu}{\alpha + \alpha\, e^{2\alpha h}} \\ C_2 = \frac{J_m \cdot \mu\, e^{2\alpha h}}{\alpha + \alpha\, e^{2\alpha h}}. \end{cases} \tag{2.32}$$

With both coefficients now defined, the final vector potential distribution inside the rotor can be found by substituting eq. (2.32) in eq. (2.23). The final distribution is then eq. (2.33),

$$\mathbf{A} = \frac{\mu J_m}{\alpha} \left(\frac{-e^{\alpha(y-2h)} + e^{-\alpha y}}{1 + e^{-2\alpha h}} \right) e^{\jmath(\omega t - kx)}\, \mathbf{u_z}. \tag{2.33}$$

2.3.4 Electromagnetic quantities

Now with the vector potential distribution defined, the electromagnetic quantities derived by it can also be computed, by replacing the new distribution in the original equations.

Magnetic flux density

The flux density distribution,eq. (2.34), can be obtained through eq. (2.13), where $\mathbf{A_z}$ is replaced by eq. (2.33),

$$\mathbf{B} = \mu J_m \left(\frac{-e^{\alpha(y-2h)} + e^{-\alpha y}}{1 + e^{-2\alpha h}} \right) e^{\jmath(\omega t - kx)}\, \mathbf{u_x} + \frac{\jmath\, \mu J_m k}{\alpha} \left(\frac{-e^{\alpha(y-2h)} + e^{-\alpha y}}{1 + e^{-2\alpha h}} \right) e^{\jmath(\omega t - kx)}\, \mathbf{u_y}. \tag{2.34}$$

Magnetic field intensity

The magnetic field intensity, eq. (2.35) distribution can be obtained through the constitutive relation in eq. (2.5a) and the now defined $\mathbf{B}$,

$$\mathbf{H} = J_m \left(\frac{-e^{\alpha(y-2h)} + e^{-\alpha y}}{1 + e^{-2\alpha h}} \right) e^{\jmath(\omega t - kx)}\, \mathbf{u_x} + \frac{\jmath\, J_m k}{\alpha} \left(\frac{-e^{\alpha(y-2h)} + e^{-\alpha y}}{1 + e^{-2\alpha h}} \right) e^{\jmath(\omega t - kx)}\, \mathbf{u_y}. \tag{2.35}$$

Current density

The current density, eq. (2.36) distribution comes from Ampère's circuital law eq. (2.6a) and the now defined $\mathbf{J}$,

$$\mathbf{J} = \frac{J_m \mathsf{k}^2}{\alpha}\left(\frac{-\mathsf{e}^{\alpha(\mathsf{y}\text{-}2\mathsf{h})}+\mathsf{e}^{-\alpha \mathsf{y}}}{1+\mathsf{e}^{-2\alpha h}}\right)\mathsf{e}^{\jmath(\omega t-\mathsf{kx})} \; - \; \alpha\, J_m\left(\frac{-\mathsf{e}^{\alpha(\mathsf{y}\text{-}2\mathsf{h})}+\mathsf{e}^{-\alpha \mathsf{y}}}{1+\mathsf{e}^{-2\alpha h}}\right)\mathsf{e}^{\jmath(\omega t-\mathsf{kx})}\,\mathbf{u_z}. \tag{2.36}$$

Force density

The force density, responsible for the motor torque, is the product between both $\mathbf{B}$ and $\mathbf{J}$, eq. (2.3c), so its distribution comes from eqs. (2.34) and (2.36). However, to calculate the force density only the real parts of both quantities are needed, so the final equation will take the form of eq. (2.37). This is divided in two components, the *x* and *y*: the horizontal is responsible for the intended movement of the machine, the one providing work; the vertical force either pushes/pulls the rotor vertically, undesired in this case.

$$\mathbf{F} = -\mathsf{Re}(J_\mathsf{z})\mathsf{Re}(B_\mathsf{y})\,\mathbf{u_x} \; + \; \mathsf{Re}(J_\mathsf{z})\mathsf{Re}(B_\mathsf{x})\,\mathbf{u_y}. \tag{2.37}$$

Now, replacing all quantities in eq. (2.37), section 2.3.4 presents the final equation for the rotor's developed force density.

$$\begin{aligned}\mathbf{F} = -\mathsf{Re}\left[J_m(\mathsf{k}^2-\alpha^2)\left(\frac{-\mathsf{e}^{\alpha(\mathsf{y}\text{-}2\mathsf{h})}+\mathsf{e}^{-\alpha \mathsf{y}}}{1+\mathsf{e}^{-2\alpha h}}\right)\mathsf{e}^{\jmath(\omega t-\mathsf{kx})}\right]\cdot \mathsf{Re}\left[\frac{\jmath\mu J_m \mathsf{k}}{\alpha}\left(\frac{-\mathsf{e}^{\alpha(\mathsf{y}\text{-}2\mathsf{h})}+\mathsf{e}^{-\alpha \mathsf{y}}}{1+\mathsf{e}^{-2\alpha h}}\right)\mathsf{e}^{\jmath(\omega t-\mathsf{kx})}\right]\;\mathbf{u_x}\\ \mathsf{Re}\left[J_m(\mathsf{k}^2-\alpha^2)\left(\frac{-\mathsf{e}^{\alpha(\mathsf{y}\text{-}2\mathsf{h})}+\mathsf{e}^{-\alpha \mathsf{y}}}{1+\mathsf{e}^{-2\alpha h}}\right)\mathsf{e}^{\jmath(\omega t-\mathsf{kx})}\right]\cdot \mathsf{Re}\left[\mu J_m\left(\frac{-\mathsf{e}^{\alpha(\mathsf{y}\text{-}2\mathsf{h})}+\mathsf{e}^{-\alpha \mathsf{y}}}{1+\mathsf{e}^{-2\alpha h}}\right)\mathsf{e}^{\jmath(\omega t-\mathsf{kx})}\right]\;\mathbf{u_y}.\end{aligned} \tag{2.38}$$

2.3.5 Linear Model simulations

With all physical quantities defined for the linear motor model, some simulations were performed to better understand the functioning principles of the machine. These results however are purely qualitative, as they only illustrate the basic principles of the machine, due to all assumptions made.

For the simulations the used dimensions were based on the adapted linear motor: stator length of 41 cm, the mean perimeter of the circular stator; a stator height of 10 cm, identical to the circular motor; a rotor length equal to the stator's, 41 cm; a rotor thickness of 15 mm, and coil number of 60 turns. The rotor's magnetic permeability is the same as its material, aluminum. All simulations consider a current 10 A 50 Hz sinusoidal.

stator length	410 mm
stator height	100 mm
rotor length	410 mm
rotor thickness	15 mm
coil number of turns	60

Table 2.1: Linear motor dimensions.

The final step for the model simulations regards the linear current density J_m. This current density results from the machine's stator configuration,fig. 2.7. The dimensions L_d and h_h are, respectively, the horizontal distance between the center of 2 consecutive teeth, and the height of each tooth. Between each tooth are the 3 coils, represented in orange, are each represented by their current phase A, B and C, and being sinusoidal each can be written as eqs. 2.39a to 2.39c.

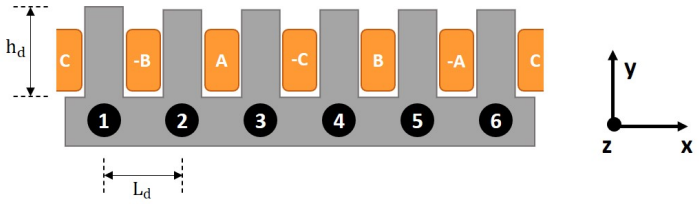

Figure 2.7: Linear stator with coil dimensions

$$i_A = I\ cos(\omega\, t) \tag{2.39a}$$

$$i_B = I\ cos(\omega\, t + \frac{2\pi}{3}) \tag{2.39b}$$

$$i_C = I\ cos(\omega\, t - \frac{2\pi}{3}). \tag{2.39c}$$

At $t = 0$, the phase A current is I, and phases B and C are -0,5I, and due to the coils' geometry, the resulting current behavior is sinusoidal, as seen in fig. 2.8.

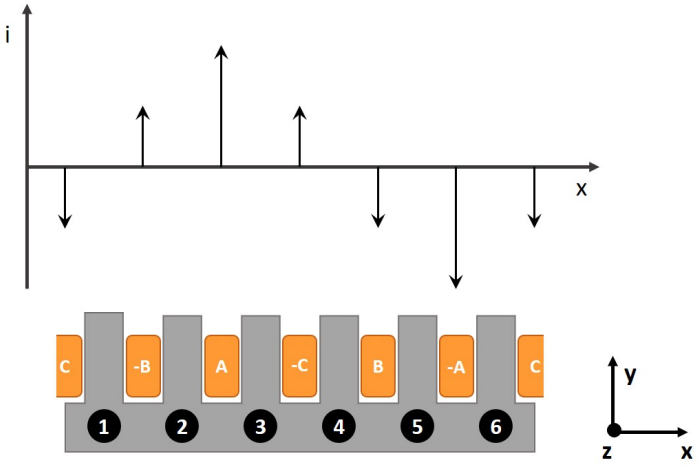

Figure 2.8: Linear stator travelling current wave.

The resulting current is then a travelling sinusoidal wave which can be written as eq. (2.40).

$$\mathsf{i} = \mathsf{I}\, e^{\jmath(\omega\, t - \mathsf{kx})} \tag{2.40}$$

Finally, since we want to calculate the current density, the stator is divided into 6 equal rectangles with dimensions $\mathsf{L_d}$ and $\mathsf{h_h}$. The current density will then be the total current divided by each rectangle area, eq. (2.41). $\mathsf{I_e}$ represents the applied RMS current in each phase, and n the number of coils per phase.

$$J = \frac{\mathsf{n}\sqrt{2}\mathsf{I_e}\, e^{\jmath(\omega\, t - \mathsf{kx})}}{\mathsf{L_d}\, \mathsf{h_d}} \tag{2.41}$$

As we consider this current density linear, the vertical component is neglected, and defining J_m as this current density amplitude, J_e can finally be defined as eq. (2.42).

$$J_e = J_m\, e^{\jmath(\omega\, t - \mathsf{kx})} \tag{2.42}$$

Magnetic flux distribution

As with any induction type of machine, the most important quantity to understand is the magnetic flux density created by the stator. It is the one responsible for inducing the currents in the rotor, and the relation between these currents and the flux is responsible for generating the torque of the machine. Consequently, its understanding is paramount.

The first simulation was the x-axis flux density, $\mathbf{B_x}$ measured mid rotor height, h/2, at 4 different moments: $t = [0; 5; 10; 20]$ ms, with a blocked rotor, i.e. velocity is 0, fig. 2.9. The purpose of this simulation was to confirm the wave form and frequency of the flux density, the same as the stator current, a 50 Hz sine. The periodicity of the signal is evident at $t = 20$ ms, at the dashed purple line overlaps the $t = 0$ line.

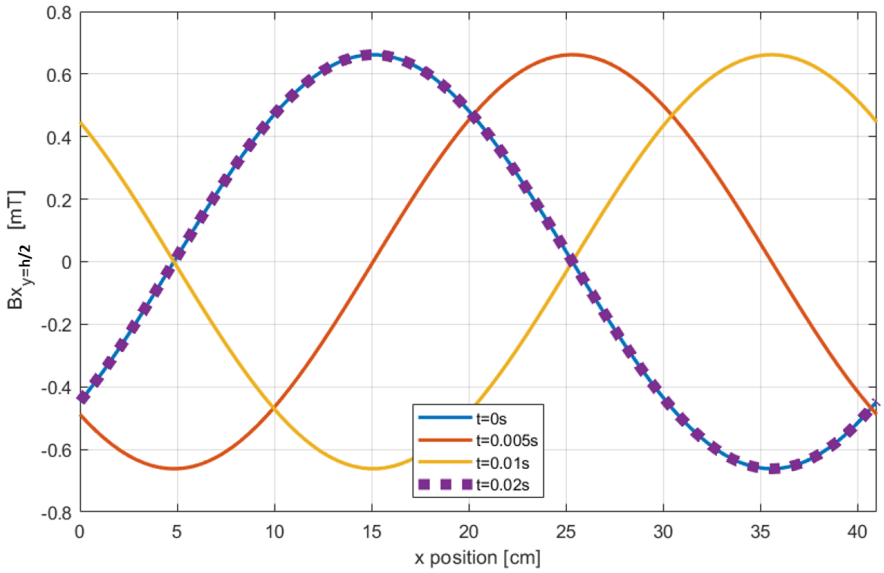

Figure 2.9: $\mathbf{B}_x$ distribution at y=h/2 along the blocked rotor length, at $t = [0; 5; 10; 20]$ ms.

Now that we know how the flux density *x*-component behaves inside the rotor, fig. 2.10 plots the same *x*-axis distribution of the flux density, however now for different rotor velocities, to understand their effect of the flux, fig. 2.10. Velocities vary between 0, blocked rotor, and 1, the synchronous speed, and the flux was again measured at the rotor's mid-height. We can see now the flux increasing with the rotor's velocity, which is a consequence of the magnetic diffusion with motion, [7]: the closest the rotor velocity is to the synchronous one, the lower the induced currents, and consequently the lowest the opposing magnetic field. In practice, the higher the velocity, the lowest is the opposing magnetic field generated by the rotor, and the higher the resulting field, the one measured. In section 2.3.5 this is will be visible in the induced current density distribution.

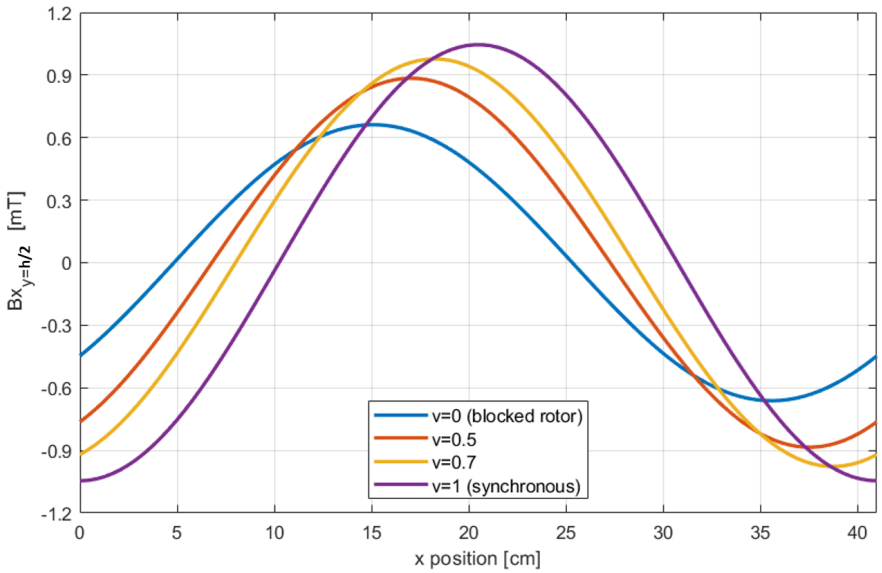

Figure 2.10: $\mathbf{B}_x$ distribution at y=h/2 along the blocked rotor length, at $v = [0; 0.5; 0.7; 1]$.

In figs. 2.9 and 2.10, the flux density was measured at h=7.5mm, half of the rotor thickness. However, it is logic the flux does not have the same value throughout the rotor height. Therefore, fig. 2.11 plots $\mathbf{B_x}$ distribution with a blocked rotor at 3 different heights: rotor's bottom, mid, and top. From this image it is visible the discrepancy in amplitudes between the 3 heights, with its maximum value at the bottom surface of the rotor, as there is no air-gap, fig. 2.5, and the minimum at the top surface, the furthest from the stator. Both mid and top values are very similar.

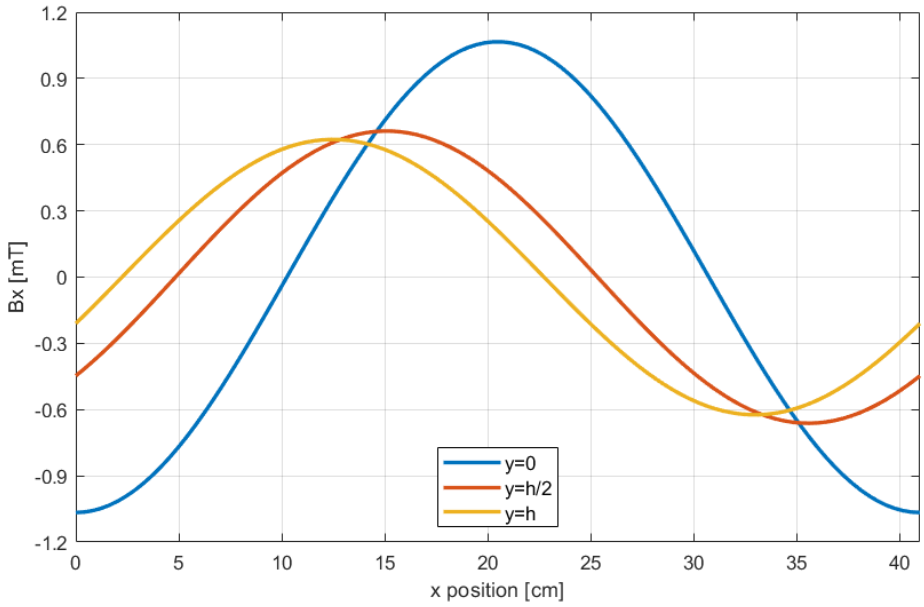

Figure 2.11: $\mathbf{B}_x$ distribution along the rotor length, at $y = [0; 7,5; 15]$mm.

However important $\mathbf{B_x}$ may be, $\mathbf{B_y}$ is also present in the rotor and its distribution is also important. Figure 2.12 plots its distribution for the same heights as fig. 2.11. We can see that all amplitudes have very different values, with the bottom flux being the highest as expected, however the top flux is null throughout the whole length of the rotor. This is a direct consequence of the second boundary condition established in section 2.3.3, as there was stapled H_y to be zero at the top surface and, as a consequence, the vertical flux density has also to be 0. This condition forces the vertical component of the magnetic field to "close" itself inside the rotor, independent of its thickness. Further in this chapter this condition is analyzed in more depth.

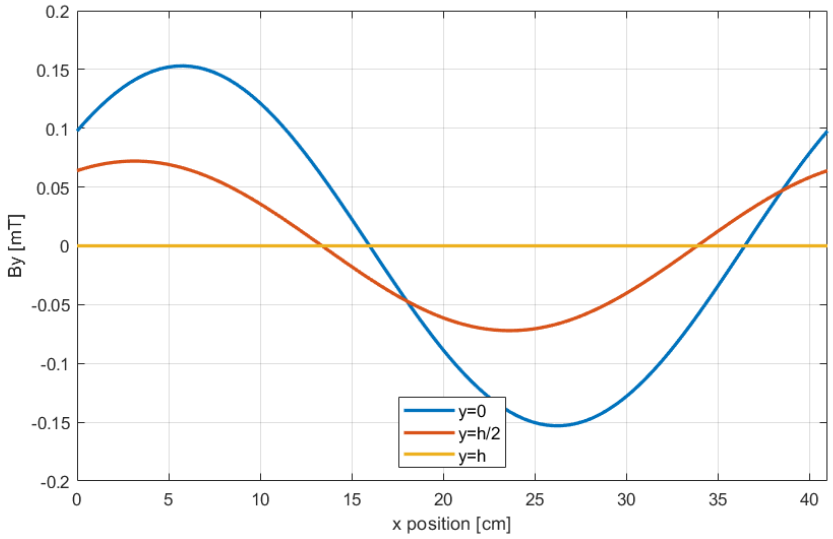

Figure 2.12: $\mathbf{B}_y$ distribution along the rotor length, at $h = [0; 7.5; 15]$mm.

With both x and y components of the flux density analyzed, fig. 2.13 plots its vector representation at the same 3 heights as before, to fully visualize the total flux density distribution.

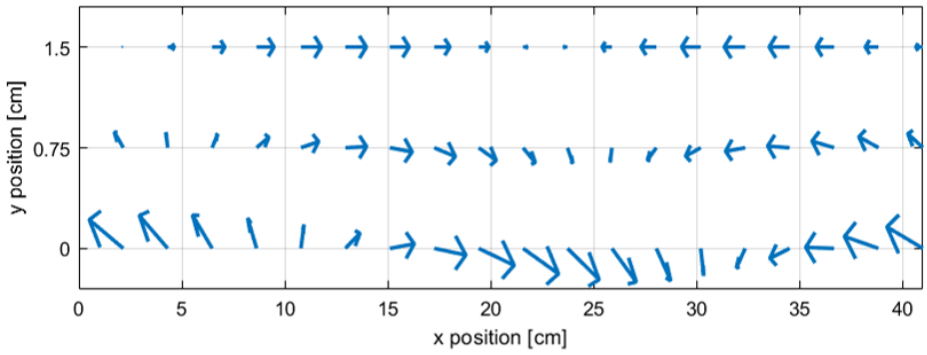

Figure 2.13: Total $\mathbf{B}$ distribution along the rotor length, at $y = [0; 7, 5; 15]$mm.

Rotor current density distribution

After the flux density distribution, the second most important quantity is the current density induced in the rotor. As assumed in section 2.2, the induced currents in the rotor have only a z component, so all following figures assume the current density to be only this component. The first current density plot is similar to fig. 2.10, as rotor velocity greatly affects the induced currents, as seen in fig. 2.14. As predicted before, the increase in velocity decreases the induced currents in the rotor, until the synchronous velocity is achieved and J becomes 0. As this happens, the opposing magnetic field created by the induced currents decreases alongside them, and consequently the resulting flux is maximum at the synchronous speed.

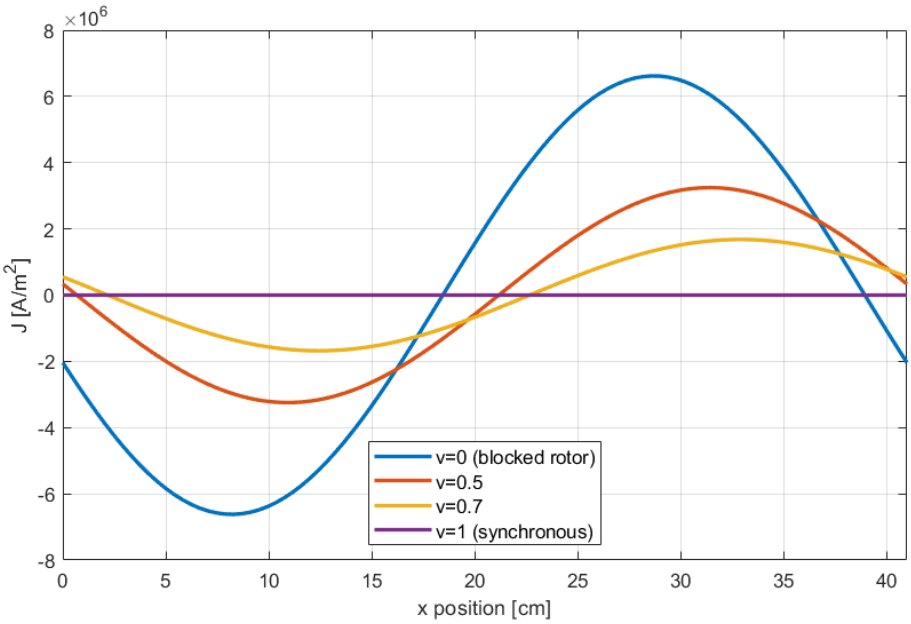

Figure 2.14: $\mathbf{J}$ distribution at *y*=h/2 along the rotor length, at $v = [0; 0.5; 0.7; 1]$.

The current density distribution inside the rotor itself is also important, so fig. 2.15 plots the current density horizontal distribution at the same 3 heights as before: bottom, middle and top. Once again, the highest amplitude occurs at the bottom of the rotor, and the lowest at the top. At the top the current density is null, as J is resultant of both $\mathbf{B}_x$ and $\mathbf{B}_y$, and the last being null as well. Since $\mathbf{J}$ is null at the top surface, the developed force must be null as well.

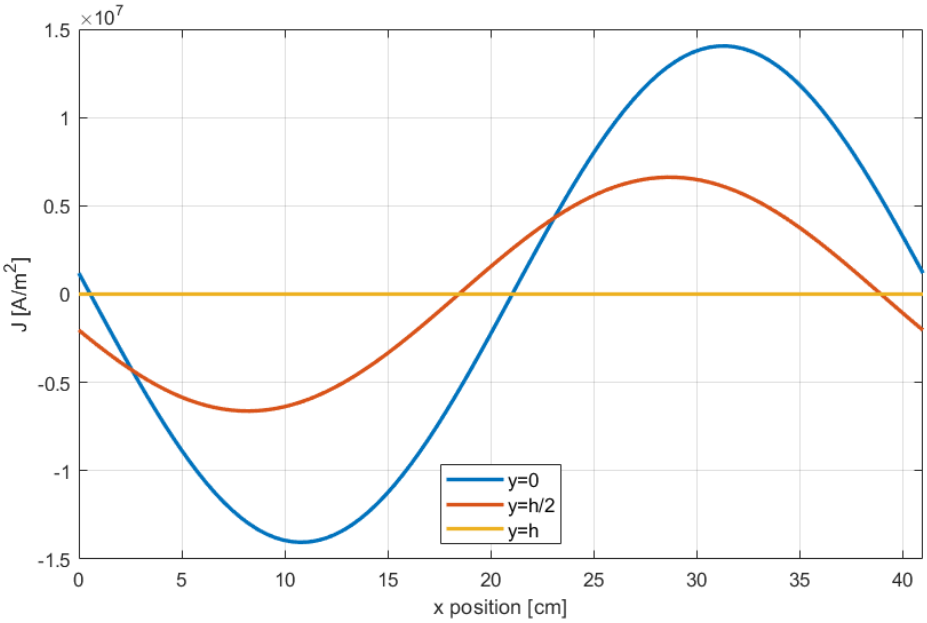

Figure 2.15: $\mathbf{J}$ distribution along the rotor length, at $h = [0; 7.5; 15]$mm.

Force density distribution

The last quantity to analyze is the rotor developed force, responsible for producing the motor's output power. With both $\mathbf{B}$ and $\mathbf{J}$ distributions known, the resulting force density should have a similar behavior: highest at the bottom and null at the top. However, its variation with the velocity changes is uncertain, as the flux increases with the velocity, the current decreases. Figure 2.16 plots the *x*-component force density evolution with a blocked rotor at the same 3 different heights. As this force density is sinusoidal, its average value is the one responsible for generating the useful force, present in the figures with a dotted line. In this case, at $y = 0$ the average force density, is the highest, around 800 N/m^3; mid-height, at $y = h/2$, the average force density is much smaller, below 200 N/m^3; at the top, as mentioned before in zero.

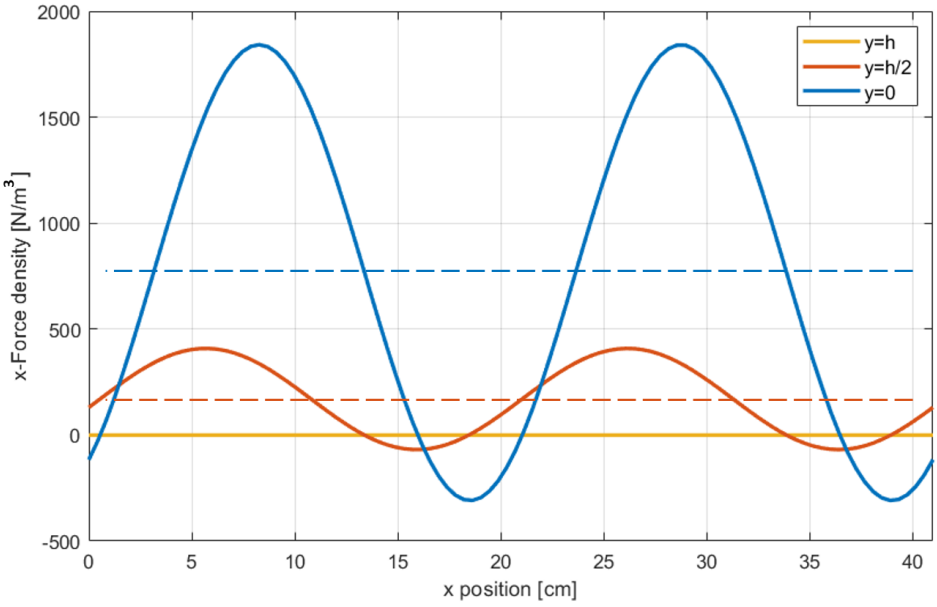

Figure 2.16: $\mathbf{F}_\mathrm{x}$ distribution along the rotor length, at $h = [0; 7.5; 15]$mm.

Now we can understand how different the force density distribution is, mainly due to having the double of the frequency of both $\mathbf{B}$ and $\mathbf{J}$. This is due to the force density being the product between the previous, and despite having the same 50 Hz frequency, these quantities are out of phase with each other, i.e. they become zero at different moments, and therefore have twice the zeros, maximums and minimums.

As a consequence, the force density beside having a frequency of 100 Hz, it has a mean value different than 0. So, at the bottom of the rotor, the force density is the highest and has a maximum amplitude of 1842 N/m^3 and a mean value of 715 N/m^3; the middle height force has a lower maximum and mean values, 408 and 171 N/m^3, respectively. The force density at the top surface, as expected, is null. However, despite the force density not being constant along the *y*-axis, the rotor is solid, and therefore produces a single force: the integral of its components.

Since this model is only qualitative, due to all considerations made, an exact value for the total average force density is unnecessary. Its distribution is more important, so figs. 2.17 and 2.18 plots both $\mathbf{F}_x$ and $\mathbf{F}_y$, respectively, measured mid-rotor height for the same velocities' range as before: blocked rotor, 50%, 70% and 100% of the synchronous speed.

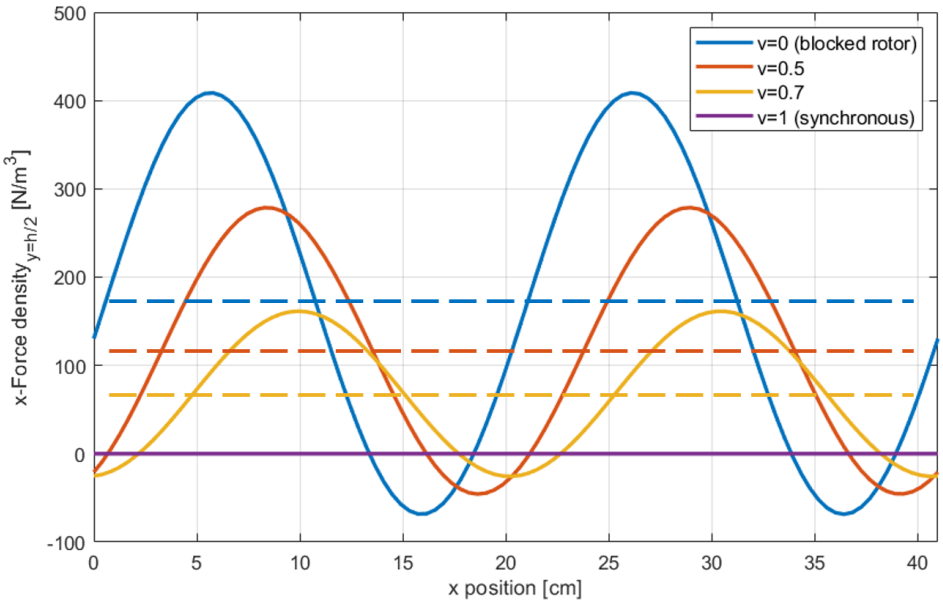

Figure 2.17: $\mathbf{F}_x$ distribution at *y*=h/2 along the rotor length, at $v = [0; 0.5; 0.7; 1]$.

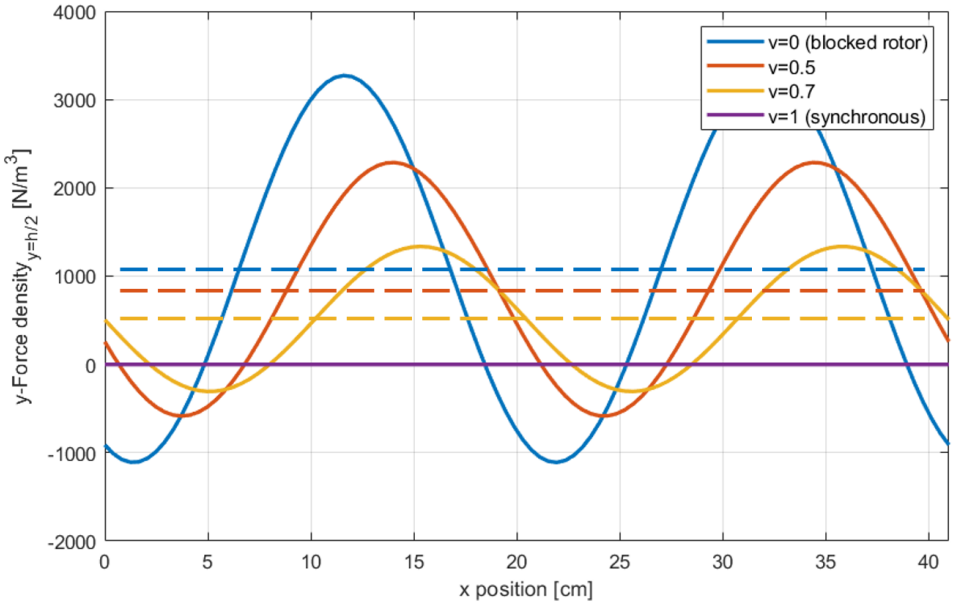

Figure 2.18: $\mathbf{F}_y$ distribution at *y*=h/2 along the rotor length, at $v = [0; 0.5; 0.7; 1]$.

In both plots there is a similar waveform as fig. 2.16 as expected, and in fig. 2.17 $\mathbf{F}_x$ mean values decrease until zero as the rotor velocity becomes closer to the synchronous one, also expected. In fig. 2.18 the mean values are positive in practice, which means the vertical force developed by the rotor is repulsive, i.e. the rotor levitates. In this machine the levitating force is neglected, however in other applications this force is used as a levitating bearing, which can be used to maintain the air-gap of the machine.

The final plot, fig. 2.19 shows the force density vectors at the 3 different heights with the blocked rotor, as to further understand the relationship between both force axis.

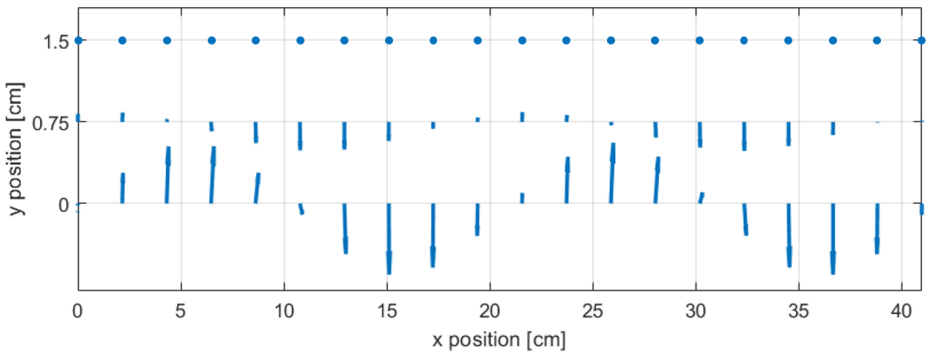

Figure 2.19: Total $\mathbf{F}$ vector distribution along the rotor length, at $h = [0; 7.5; 15]$mm.

In vector form of the force density is quite visible how different the x and y components of the force are, with all vectors being practically only vertical. This figure further illustrates how inefficient this linear machine is.

2.3.6 Analytical Model conclusions

With the linear model developed and simulated, we can understand and start to predict some behaviors of the machine. However due to all simplifications made, its simplicity cannot accommodate and predict every behavior of the machine. Furthermore, the complexity of the real machine, with an axial symmetry on the stator, and non-symmetric coils, any analytical model would be too complex or insufficient, as this linear model was, an alternative is necessary.

Due to Covid-19 restrictions in the year 2020 the laboratory access was impossible for long periods of time, so the lab work for this thesis was shortened, and the only alternative left is a 3D model of the machine. This type of model can accommodate all geometries of the machine and all possible alterations needed. So chapter 4 to chapter 7 show the building, testing and simulations of this model.

2.4 Magnetization curve

Ferromagnetic materials, like the ones used in electrical machines due to their electrical and magnetic properties, have a magnetization curve to represent its magnetic properties.

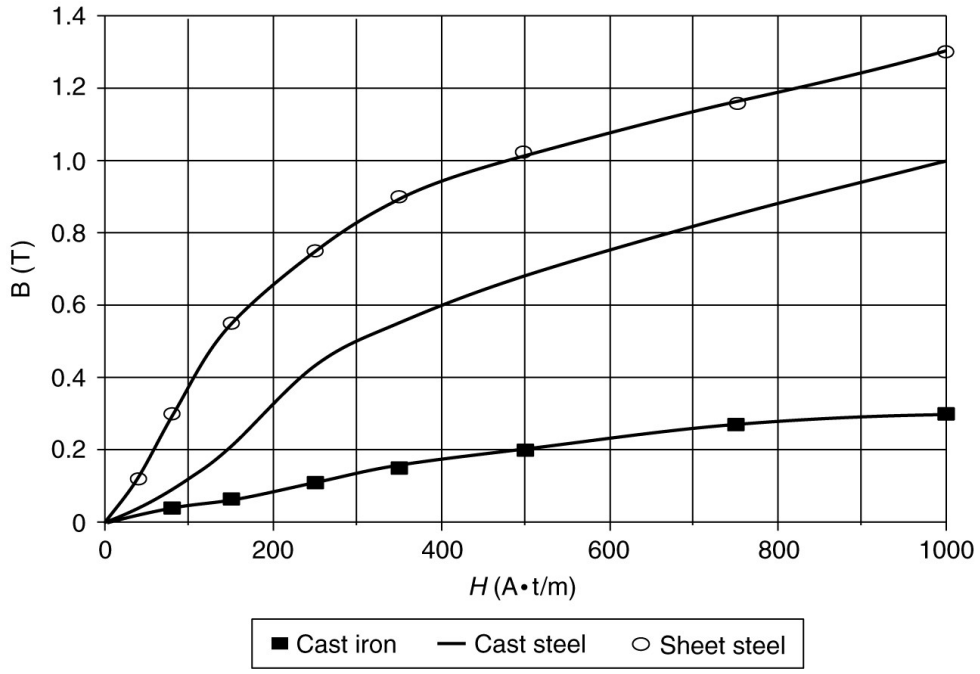

Figure 2.20: BH curve for three different materials [8].

This relation is a result of the material's physical properties and can be interpreted as the imposing of a magnetic field and the resulting flux density the material can generate, eq. (2.43)

$$B = \mu H. \tag{2.43}$$

The material's magnetic history is as well an important factor, as most materials show hysteresis, i.e. the number of magnetization cycles occurred influence the amount of hysteresis present [6]. The fig. 2.20 shows a DC an-hysteretic curve, which means the material's excitation was done with a non-alternating signal, usually a rising positive excitation, and therefore does not present hysteresis; however, every AC machine works with time-dependent alternating quantities and therefore will show some level hysteresis.

The magnetic hysteresis occurs whenever a material is excited with an alternating field, fig. 2.21. Firstly, when the material is magnetized, from the origin to **b**, a field $H(b)$ is needed to impose a flux density $B(b)$; however, when the material is demagnetized, from point **b** to **c**, the same field is applied, however it is not sufficient to decrease B to zero, and a remnant flux density persists, $B(c)$; some additional field is therefore needed to finally decrease B to zero, **d**, with $H(d)$ being the coercive field. As the cycle continues with the alternating field intensity, a symmetry occurs, with symmetric values: maximum imposed fields, $H(b)$ and $H(e)$, maximum flux densities, $B(b)$ and $B(e)$, remnant flux densities, $B(c)$ and $B(f)$, and coercive magnetic fields, $H(a)$ and $H(d)$.

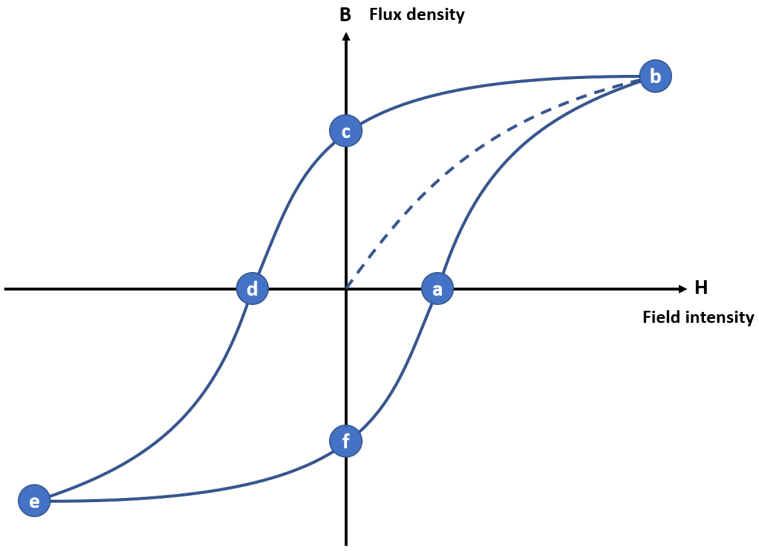

Figure 2.21: Generic BH curve with hysteresis.

This behavior is a result of the magnetic domains that compose a ferromagnetic material, as the imposing of a magnetic field in a direction causes the alignment of said domains until they are completely aligned with the field; when the imposed field changes direction, the domains will in turn re-align themselves into the opposing direction, however the amount of energy need to fully re-align them domains is higher, as there is a need to fully invert the direction of every domain; whereas originally, when no external field is applied, the domains have no specific orientation and therefore do not need to completely invert its rotation [4].

Most material's BH curve is easily obtained, whether through the manufacturer's or for more common materials the relation is already known and easily available. However, this relation will almost always be the DC curve with no hysteresis, as hysteresis as already discussed will depend on the application, so usually it has to be measured under the application conditions.

Chapter 3

Stator Characterization

3.1 Magnetization curve measurement motives

The motor's stator that is already constructed is made of a soft iron alloy, Somaloy ®, whose physical properties ended not matching the manufacturer's, as the previous works showed [1, 3]: the theoretical model developed in the first part was simulated with the product's specifications from the manufacturer, and the physical motor was built with the real material. However, as mentioned in section 1.1, when the motor was tested in the laboratory, the experimental data did not match the simulated. Consequently, a more comprehensive electromagnetic characterization of the machine is needed.

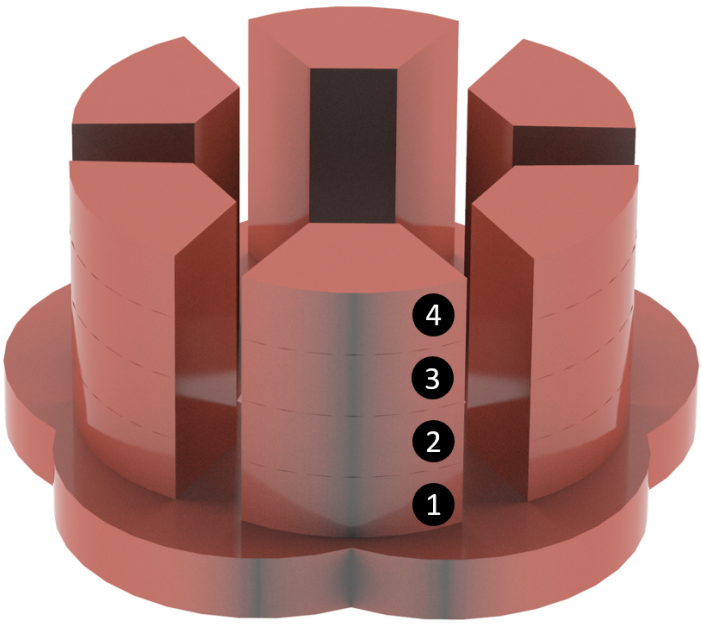

Figure 3.1: Stator assembly with marked layers, 3D render.

In fig. 3.1, a close-up view of the stator shows its full assembly, with the stacks of pieces that comprise each tooth, four 20 mm pieces, and the stator base, with 5 pieces fig. 3.2. This type of geometry, comprised of several glued pieces, makes the stator a ”composite” material, as the iron alloy, glue and air in the air-gaps between each piece, all have very different magnetic permeabilities. Due to this, the stator's ferromagnetic properties cannot be reduced to the same as the iron alloy comprising itself. So, the first step to create a more accurate finite elements' model is to characterize the real stator as it was built instead of relying on manufacturer's soft composite data. This is done by experimentally measuring the magnetization curve of the stator body.

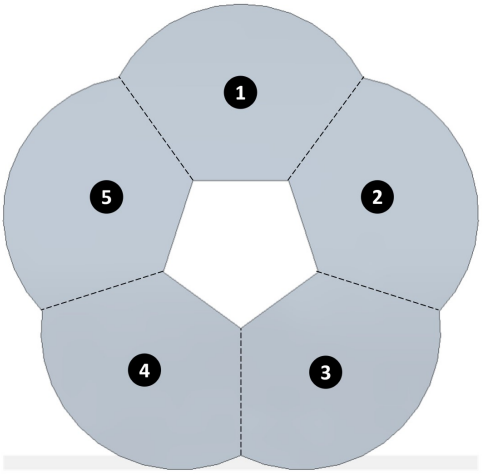

Figure 3.2: Stator core base assembly.

3.2 Experiment process outline

To induce a magnetic flux in a material, the easiest way is through the winding of a coil around the material, where a sinusoidal voltage is applied at its terminals, u . However, due to the coil's resistance, there is a voltage drop at its terminals, making the available voltage the difference between both, eq. (3.1)

$$u = Ri + \frac{d\Psi}{dt}. \tag{3.1}$$

This available voltage is in turn equal to the variation of the magnetic flux linkage in the coil, Ψ. This magnetic quantity is in turn equal to the total magnetic flux imposed by the coil,

$$\Psi = N_t \cdot \phi \tag{3.2}$$

$$\phi = B \cdot S \tag{3.3}$$

where N_t denotes the number of turns comprising the coil, and ϕ the flux per turn. This flux can be approximated by the magnetic flux density B through the coil area, S.

This flux density relates with the quantity H , magnetic field, through the material's magnetization curve. This quantity is in turn related to the current circulating in the coil,

$$H \cdot l = N_t \cdot I. \tag{3.4}$$

3.3 Experiment

The first experiment done is the characterization of the magnetization curve of the stator with the use of a new 200 turn coil and an auxiliary iron alloy disk, used to close the magnetic circuit between two consecutive stator teeth, fig. 3.3. This new coil has 200 turns as the higher the number of turns, the lower the current, and consequently the less dangerous the experiment.

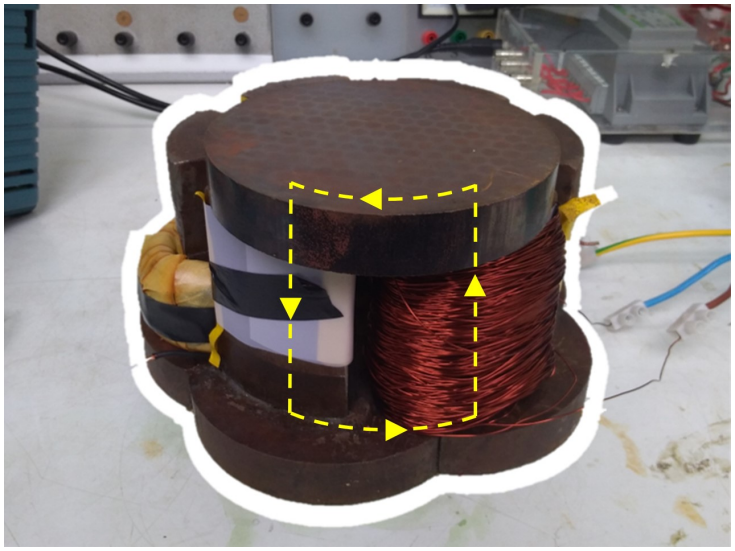

Figure 3.3: Stator assembly with auxiliary and magnetic path.

By closing the air gap of the circuit at the top of the teeth with the same material as the stator, we reduce the magnetic dispersion in the air, making it easier to achieve magnetic saturation, a crucial part of a BH curve. Now, we have a magnetic circuit, comprised of a single type of "material", the alloy-glue material, with a certain equivalent magnetic permeability and a possible saturation level.

The experiment, whose setup is shown in fig. 3.4, is done in the laboratory by applying a 50 Hz voltage in the auxiliary coil, 1, and measuring both the current and the voltage waveforms with an oscilloscope, 4. The current is acquired with a current probe, 2, and the voltage with a 20/1 isolation transformer, 3. This transformer is useful as it not only isolates both signals, the original and the oscilloscope one, but also reduces the voltage amplitude by a 20:1 ratio, and finally both signals are monitored with an additional and current meter and volt meter, 6 and 7. As the saturation of the material is desired, temperatures higher than nominal are expected, so the temperature at coil is monitored with a thermal probe connected to a multimeter, 5.

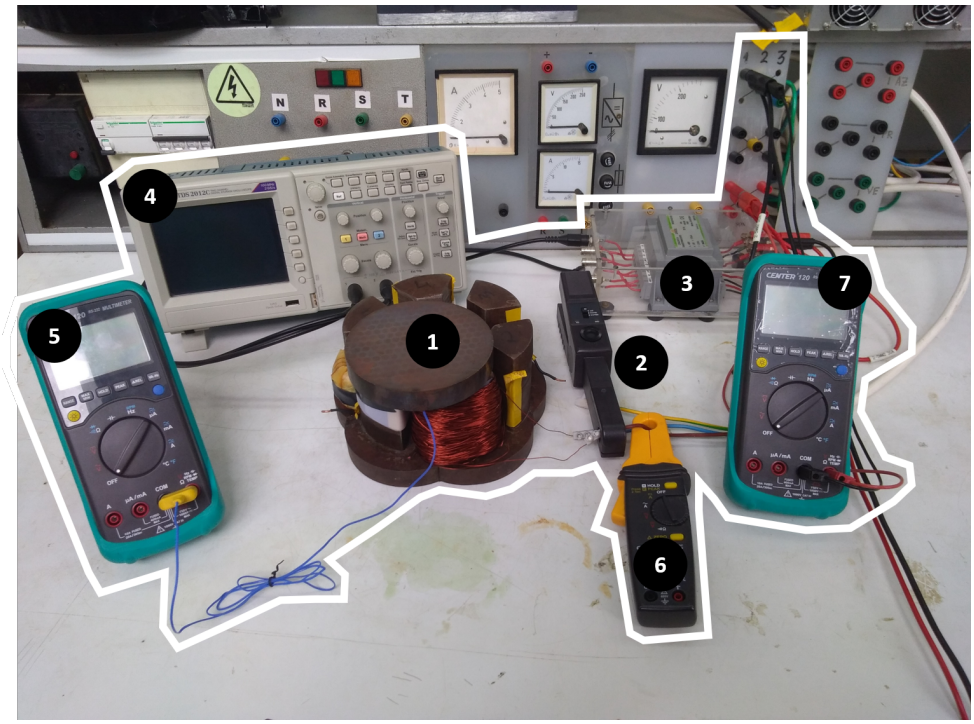

Figure 3.4: Laboratory setup for the stator BH curve measurement.

The experiment was done for different voltages, between 1 V and 196 V amplitudes, due to temperature limitations, as the temperature inside the coil reached 110°C with the highest voltage. Figs. 3.5 and 3.6 show two of the applied voltage and respective currents, at 50 V and 196 V, respectively.

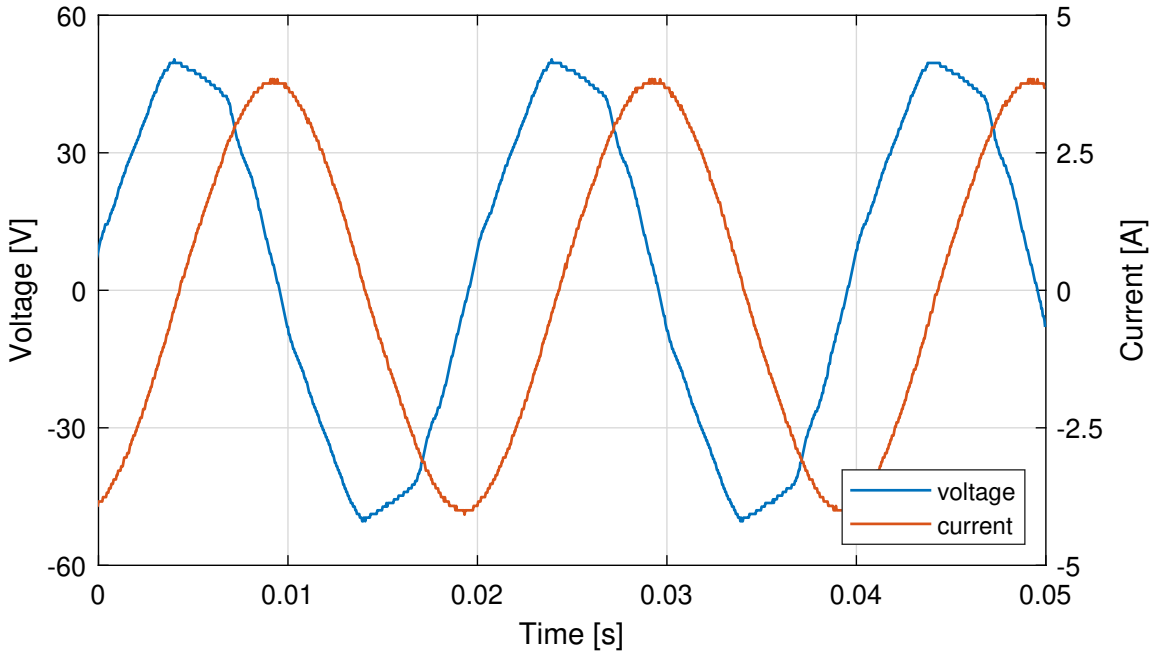

Figure 3.5: 200 turn coil excitation - 50V.

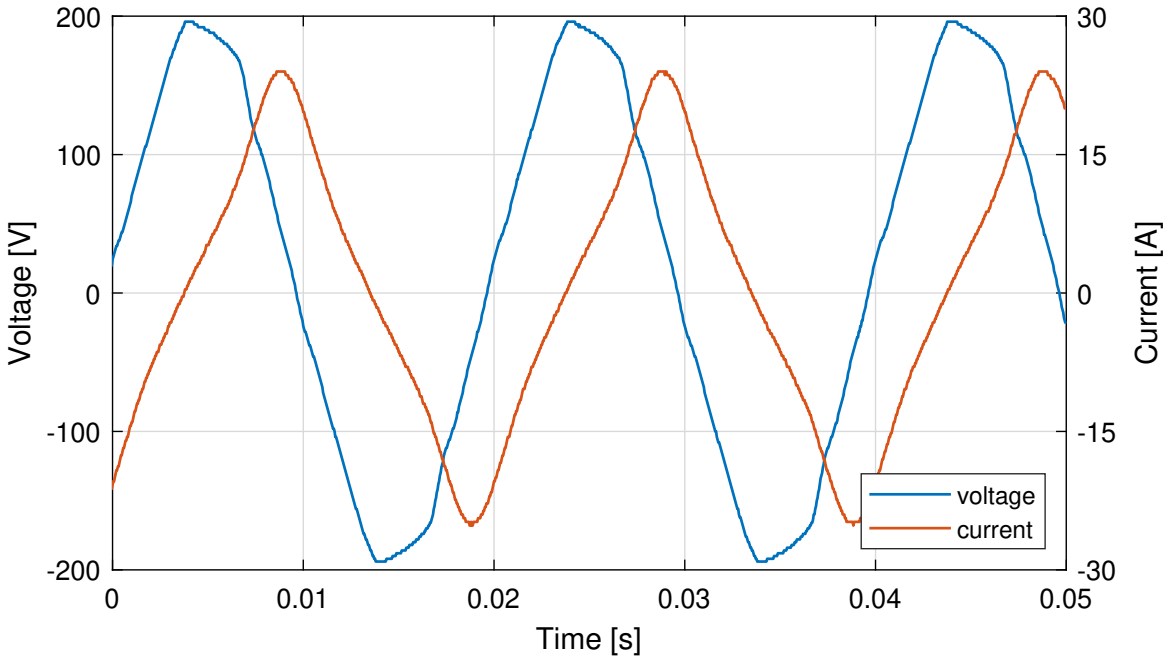

Figure 3.6: 200 turn coil excitation - 196 V.

By observation of the waveforms alone it is possible to see the magnetic saturation effect of the material, as the current in fig. 3.6, from the highest voltage applied, is no longer sinusoidal, whereas the current in 3.5 remains sinusoidal.

Now, with the voltage and current signals acquired, the magnetic flux density and magnetic field intensity need to be calculated. According to the induction law, the flux linkage Ψ can be expressed as

$$\Psi = \int (u - Ri) \cdot dt \tag{3.5}$$

and sometimes, when the voltage drop at the coil's terminals is much smaller than the applied voltage, this voltage drop is neglected and

$$\Psi \approx \int u dt. \tag{3.6}$$

By definition, the flux linkage is the total flux in the coil with N_t turns

$$\phi = \frac{\Psi}{N_t}. \tag{3.7}$$

The flux density B can be approximated by dividing the flux on each turn by its normal surface area, S

$$B = \frac{\phi}{S}. \tag{3.8}$$

The magnetic field H is obtained through the relation in eq. (3.9), and as explained before, is a result of the current circulation in a coil, with N_t turns. The product between the current and the number of coils is called the magnetomotive force, F_{mm}, equal to the magnetic field intensity H along the magnetic circuit where it circulates, with the length l,

$$H = \frac{N_t \cdot I}{l}. \tag{3.9}$$

Now, with for each voltage-current pair of signals the BH curve for the magnetic circuit is calculated. Fig. 3.7 shows the BH curve for 50 V and 196 V excitations.

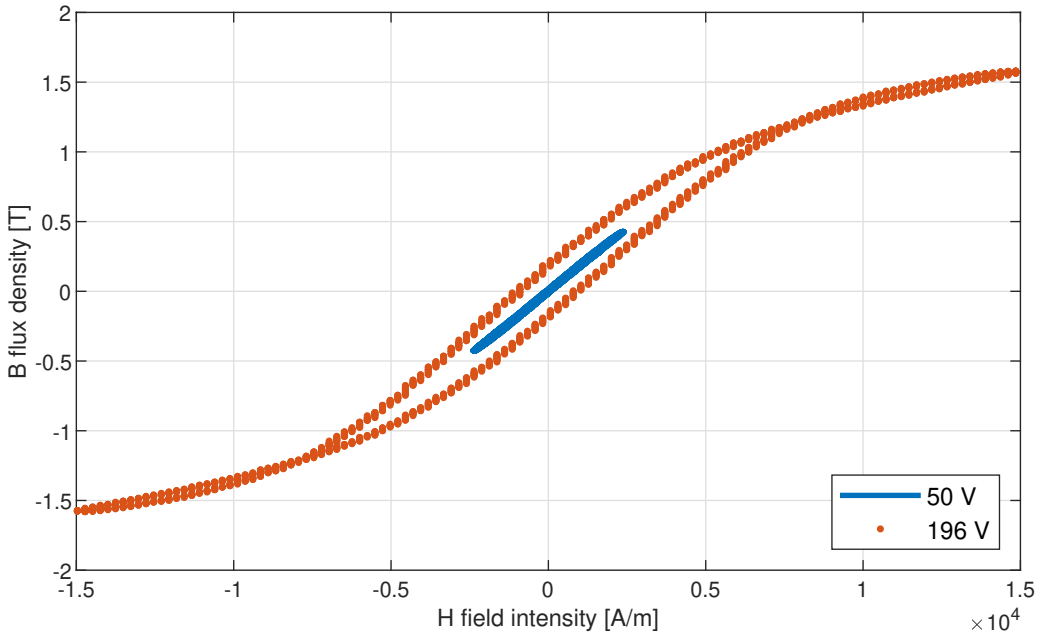

Figure 3.7: Stator core BH curve for 50 and 196 V.

The blue line is the BH curve for the 50 V excitation, where the relation between both quantities is practically linear, as the material is still far from saturation. When the BH relation is this linear, the magnetic permeability can be obtained, as

$$B = (\mu_r \mu_0) \cdot H \tag{3.10}$$

$$\mu_0 = 4\pi \cdot 10^{-7} [\text{H/m}] \tag{3.11}$$

$$\mu_r \approx 141 \tag{3.12}$$

with μ_r the relative permeability and μ_0 the vacuum magnetic permeability.

In the 196 V signal, where the maximum B is reached, the curve's slope decreases almost to zero at both ends of the graphic, where H is the highest. This happens because the material can no longer support a higher magnetic density, despite the increase in magnetic field intensity. Because the slope of the curve does not actually become μ_0, the material does not reach full saturation, however it almost saturates, being the saturation density not much higher than B_{max}, 1.6 T.

It is also important to mention the hysteresis of the material, observable on the plot by the widening of the curve on the middle. This widening happens because the material consists of atomic domains, such that when a magnetic field, H is applied to them, they align with said field. However, when the external field changes direction, the domains take time and energy to re-align themselves in the new direction, being this extra energy and delay are what causes hysteresis. In this case, as the applied voltage increases, the external field H also increases and the cycle widens: for the same B inside the material, there's a need for a higher H to achieve it.

As mentioned before, in some cases, the voltage drop at the coil's terminals can be neglected, and fig. 3.8 plots the BH curves for the stator, neglecting and considering this voltage drop, with 2 different excitations, 50 and 196 V.

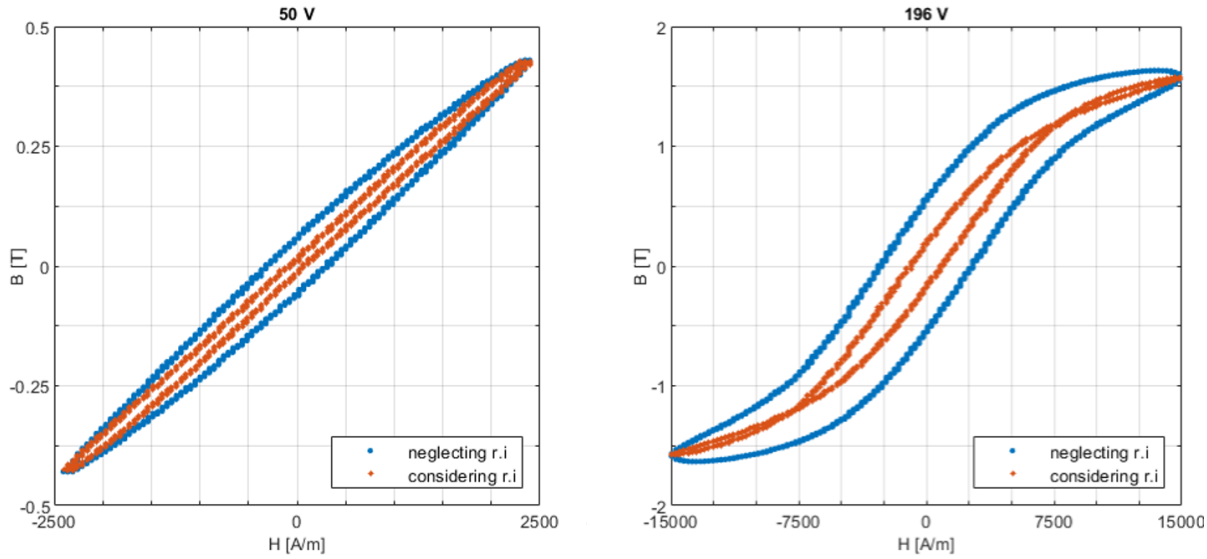

Figure 3.8: BH curves for (a) 50V and (b) 196V, considering and neglecting voltage drop.

From the figures we can now understand the importance of the voltage drop, as the curves in blue are calculated without considering the losses in the coil, and the orange ones, considering. Although the peak values don't vary, maximum and minimum values for both quantities, the area of the curves is completely different. For the lowest voltage, 50 V, the relation is practically linear when considering the drop; The highest, 196 V, the area inside the hysteresis curve, the magnetic energy, is much higher than the real one, considering the drop voltage.

Having now several BH curves for the magnetic characterization of the stator core, it is necessary to do a curve fitting and define a function that represents it. For the simulations. It is also relevant to mention that although the curve shown before is represented in all 4 quadrants, it is only necessary to define it in the first one, as the other quadrants representation is done by inverting the first quadrant one. Obviously, this is only valid by neglecting hysteresis, as it is a function of the material history.

The experimental hysteresis data is post-processed through the average of all the points with the same field intensity in the positive H axis, followed by a curve fitting, fig. 3.9. As the fitted signal, a 2nd degree polynomial function, started drifting from the experimental data around a 9,000 A/m field, the final curve, in orange, uses the experimental points in the end of the curve, as there is almost no scattering, while remaining monotonically increasing, a crucial property of a BH curve.

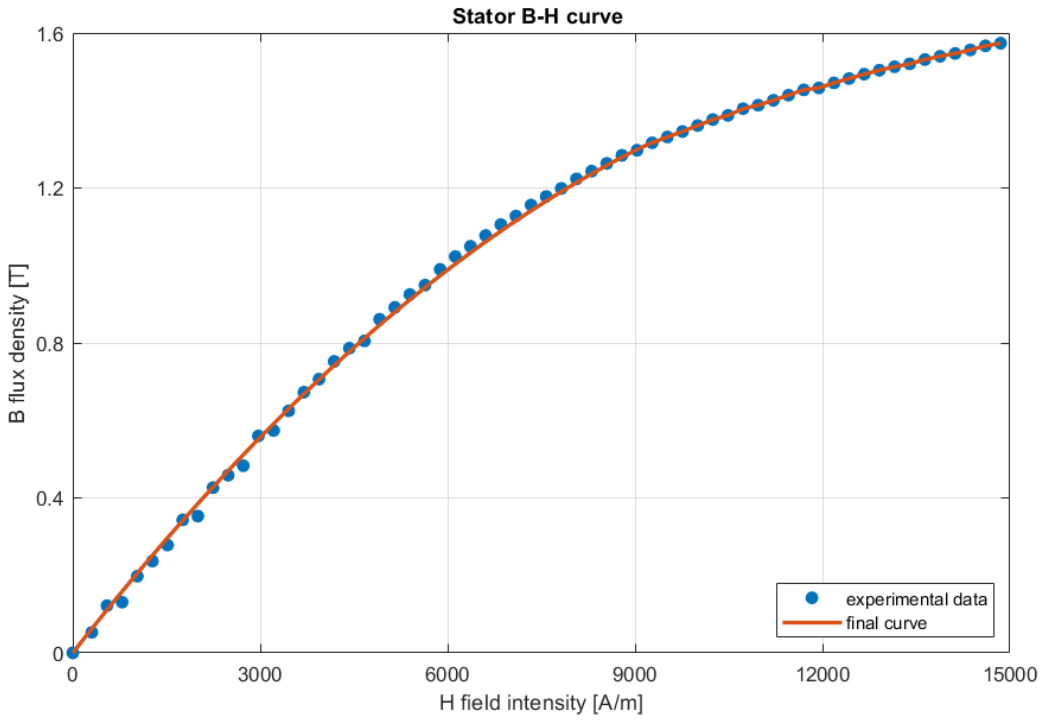

Figure 3.9: Experimental and fitted BH curves.

3.4 Manufacturer's and Experimental BH curves comparison

Having now the stator's core material BH curve, it is finally possible to compare it with the manufacturer one and start to understand the differences between the assembled stator and the initially one designed. Figure 3.10 shows both curves, in blue, the experimental data, and in orange, the manufacturer's data.

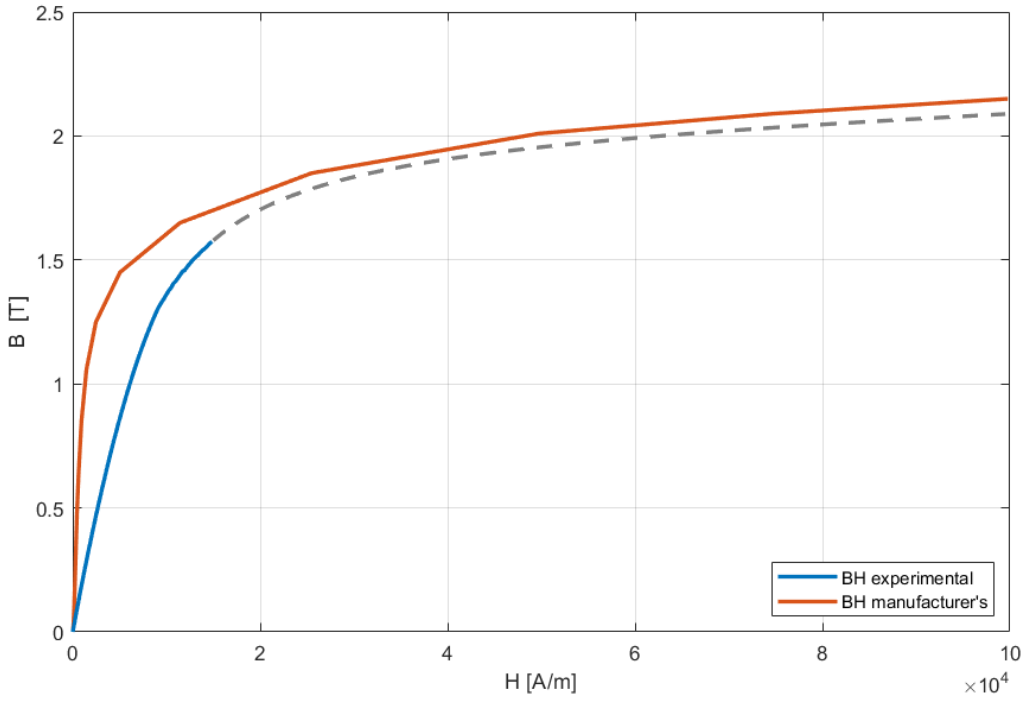

Figure 3.10: Experimental and manufacturer stator core BH curves comparison.

It is easy now to understand the magnetic performance differences between the theoretical and practical. The permeability, measured in the linear part of both curves, is much higher in the datasheet than the experimental. The knee of the theoretical curve occurs around 3000 A/m, as the practical occurs at about 10000 A/m. In practice, this means that to achieve the same flux density, it is needed a much higher field intensity to do it so, which implicates a higher number of turns on the coils or a higher current.

Due to current limitation in the laboratory, a significant saturation level was not achieved at any experiment. The maximum measured was 1.6 T. This constraint is a result of the thermal energy loss inside the coils, as the reached temperature became so high, higher currents were impossible. To circumvent this phenomenon, 2 other equal sets of coils were wound around the original one, creating a coil with 3 configurations: 200, 400 or 600 turns. However, despite higher field intensities were achievable, the increase in resistance of the coil set meant a much higher voltage was needed to generate the same magnetic flux density value. In conclusion, this increase in coil turns was cancelled by the maximum voltage available, 400 V_{rms}; and the increase in resistance also caused coil temperatures even higher than before, ending in a short circuit of the coil.

So, with the impossibility to induce a higher magnetic field in the stator circuit, fig. 3.10 is now plotted at a more appropriate scale, fig. 3.11, as the motor operating limit point is around 1000 A/m (for a 3-phase 10 A rms current).

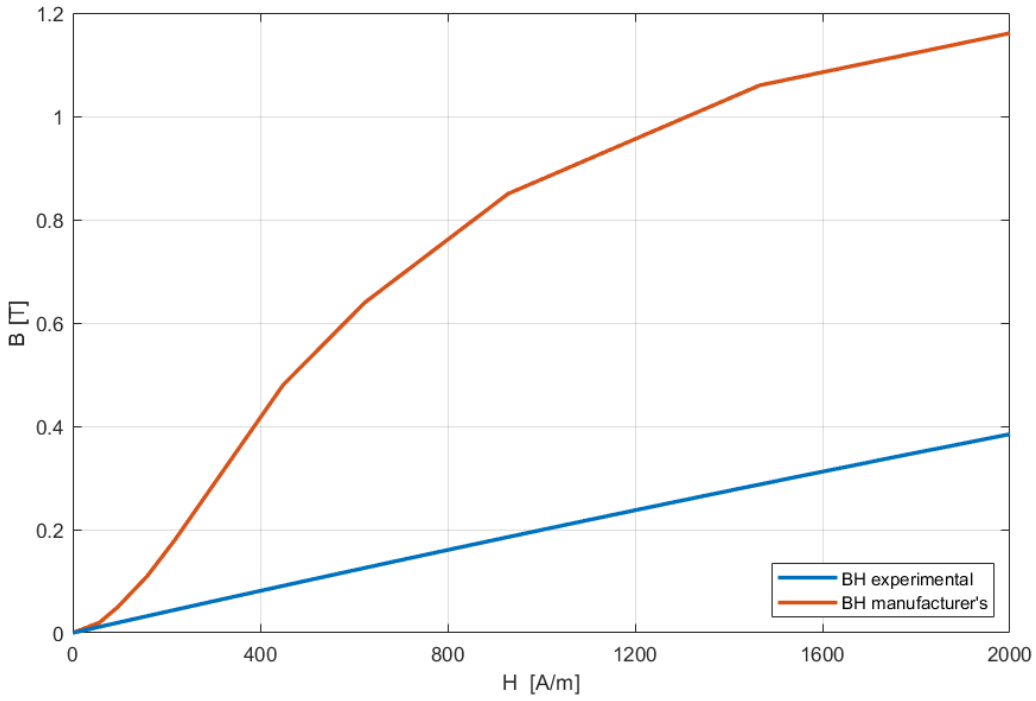

Figure 3.11: Experimental and manufacturer BH curves comparison, close-up.

Now we can observe in more detail both curves, and evidence that with such magnetic fields, the permeability difference is even higher, as for a 1000 A/m field the flux is approximately 0,2 T in the experimental curve and 1 T according to the manufacturer. This difference in the magnetization curves is mainly due to the used stator structure, where the glued surfaces used to join the alloy pieces create tiny air-gaps responsible for an increase in the magnetic reluctance of the circuit, with measured relative permeability of 141 and a manufacturer's relative permeability of 660 in the same operating region.

Chapter 4

Finite Element Method Model

4.1 Geometry

To perform a more detailed and complete analysis of the machine, an equivalent 3D electromagnetic simulation model had to be developed, similar to the one developed in the [1]. The Finite Element Method (FEM) was the used to solve the problem, with the use of a FEM simulation software. This model was designed with the actual dimensions of the real motor, and an additional sphere of air involving the main geometry fig. 4.1. The model also considers the real materials and their properties due to their significance.

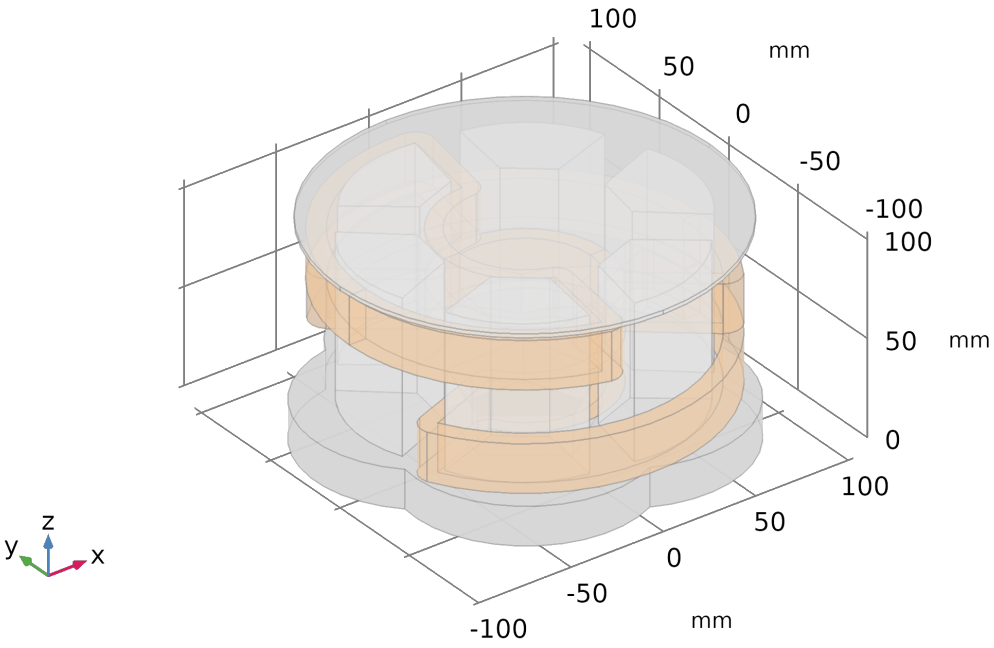

Figure 4.1: 3D render of the finite elements motor.

Despite this model being the most important, as it models the electromagnetic physics of the motor, other physical models were also developed, such as the thermal model, different coils and rotating machinery model.

4.2 Materials

The second step when designing a FEM model is the selection of the materials for the model, as they will define the physical properties of each material. In this case, for a magnetic field simulation the most important characteristics are the electrical conductivity and magnetic permeability, the latter coming from a magnetization curve or the relative value in case of a linear characteristic.

In the FEM model, several materials were used for the different parts of the machine, being most of them part of the software library. However, as already demonstrated, to create a more accurate electromagnetic model of the motor, the stator's iron core material is going to be characterized by the magnetization curves built from the experimental data. In total, there were used 4 different materials, table 4.1. Figure 4.2 shows the model's main geometries: stator, coils, rotor and enveloping air volume.

Material	electrical conductivity	BH relation
Stator iron alloy	5000 [S/m]	measured BH curve
Aluminum	3.774 $\cdot 10^7$ [S/m]	$\mu_r = 1$
Copper	5.998 $\cdot 10^7$ [S/m]	$\mu_r = 1$
Air	10 [S/m]	$\mu_r = 1$

Table 4.1: FEM model materials' electromagnetic properties

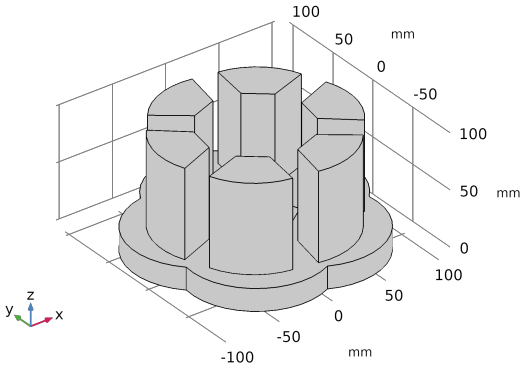

(a) FEM model stator

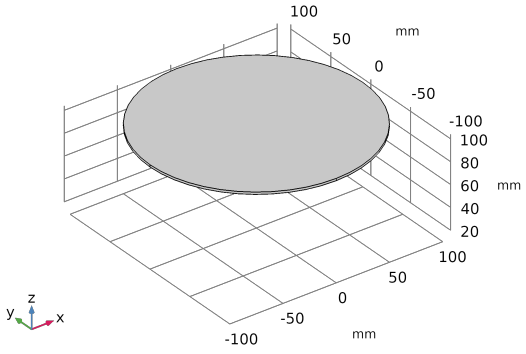

(b) FEM model rotor

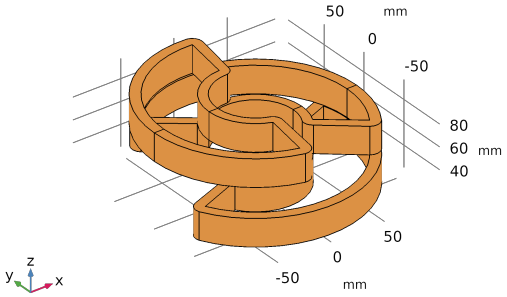

(c) FEM model stator winding coils

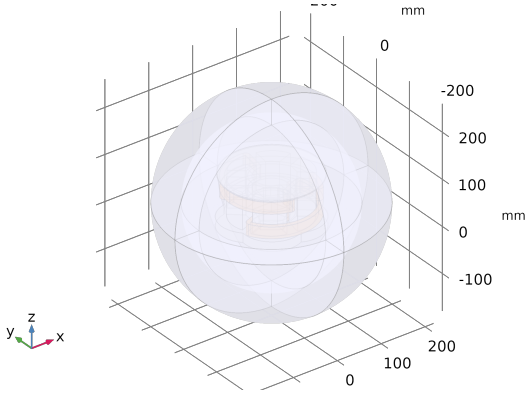

(d) FEM model air volume

Figure 4.2: FEM model main geometries.

4.3 Meshing

In a FEM analysis, the model meshing, i.e. the division of the geometries in a grid, is a necessary and important part of the simulation, as it defines the portion of the model where the physics calculations will be performed. The meshing of the model is in itself a challenge as it is the outcome of a balance between precision for the solution and computing resource usage: the finer the mesh, the more precise the model is and more detailed the solution will be. However, the number of mesh elements increases and the computational resources to solve it increase as well. The solution. fig. 4.3 for this problem is then divided in 2 different approaches:

- For the more relevant domains, the finer the mesh is, to increase accuracy and optimize the quality of the model. This approach is then used in the stator, coils, and rotor of the machine model;

- For the less important domains (the air surrounding the main geometry), the mesh is coarser, making the number of elements also smaller and the resolution worse. This air mesh consists of a sphere surrounding the model, with a coarse mesh inside and an infinite mesh on the outside. Here the field decays exponentially until the outer surface, where it is set to zero, marked by the red dashed line in fig. 4.3.

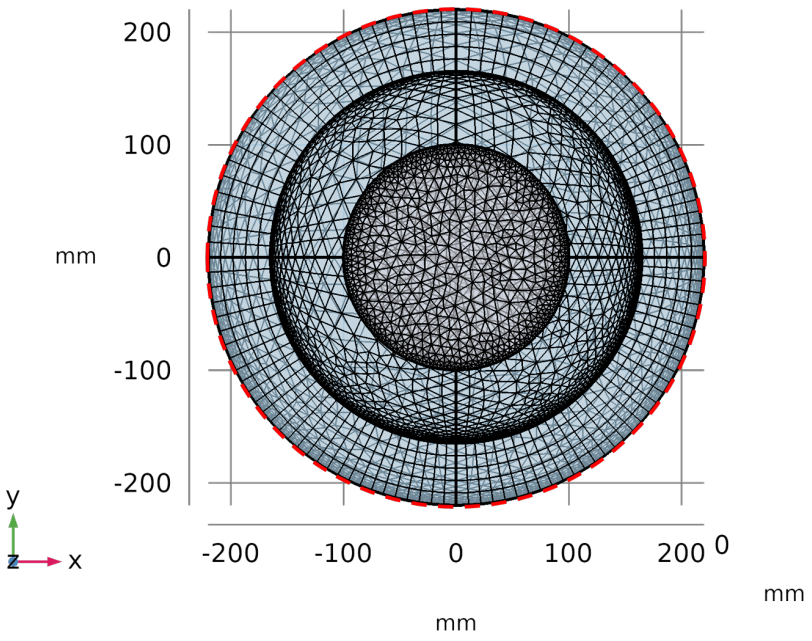

Figure 4.3: Mesh top-view of the finite elements motor.

4.4 FEM electromagnetic Physics

The Physics step of any FEM is the most important, as here are defined the electromagnetic physics conditions for the solver. Here the user defines the relations between physical domains, the boundary conditions separating them, and in some cases specific types of domains.
The first set conditions are intrinsically connected to the type of study, in this case, a Magnetic Fields' study. The Ampère's Law for all domains,eqs. (4.1) to (4.4), the Magnetic Insulation, eq. (4.5), and finally the initial values, eq. (4.6).

Firstly, the Ampère's Law condition is set for all domains, eqs. (4.1) and (4.2). The BH relation used for each material is their relative permeability, table 4.1, except for the stator, where the used BH relation comes from the curve built.

$$\nabla \times \mathbf{H} = \mathbf{J} \tag{4.1}$$

$$\mathbf{B} = \nabla \times \mathbf{A} \tag{4.2}$$

$$\mathbf{E} = \frac{-\partial \mathbf{A}}{\partial t} \tag{4.3}$$

$$\mathbf{J} = \sigma \mathbf{E}. \tag{4.4}$$

The next condition is a boundary one, the Magnetic Insulation on the outside surface of the air volume surrounding the volume, eq. (4.5), where the infinite elements domain surface is characterized by

$$n \times \mathbf{A} = 0 \tag{4.5}$$

forcing the value of the potential vector to be zero at the outermost boundary.

The Initial Values condition in eq. (4.6) sets the vector potential to be zero at the beginning of the study

$$\mathbf{A}_{x,y,z} = 0. \tag{4.6}$$

The final condition is a specific domain condition for the coils, as their geometrical representation is only the volume they occupy. Equation (4.7) defines the external current circulating in the coil to be related to the coil parameters: coil resistance, from the real wire thickness and material, the input voltage at its terminals, the number of turns and the length of each turn. Besides these values, the last domain parameter is e_{coil}, the direction unity vector following the mean path for the coil, defining the current density direction.

$$\mathbf{J}_e = \frac{N_t(V_{coil} + V_{ind})}{S * R_{coil}} \mathbf{e}_{coil}. \tag{4.7}$$

4.5 FEM Simulation Studies

The last step of the model setup is the study that will solve it, according to the user specifications. The most common study is a time dependent study, where the software solves the model in time steps, for a total time, also user defined. This kind of study not only provides a more detailed solution, with a time step as small as one needs, but also allows non-sinusoidal excitations, making it the most complete study. However, this type of study is very resource intensive, so alternatives were explored.

4.5.1 Frequency Domain study

The Frequency Domain study was the most used, albeit only valid for sinusoidal quantities. However, at normal operating conditions the motor is to run without significant magnetic saturation, and therefore most quantities will remain sinusoidal. This study, instead of considering time dependent quantities, considers frequency dependent ones, and equations eqs. (4.3) and (4.4) are replaced by eqs. (4.8) and (4.9)

$$\mathbf{E} = -\jmath\omega\mathbf{A} \tag{4.8}$$

$$\mathbf{J} = \sigma\mathbf{E} + \jmath\omega\mathbf{D}. \tag{4.9}$$

However, at low frequencies, such as the normal operating frequency of 50 Hz frequency, a quasi-magnetostatic regime can be assumed, and displacements currents can be neglected, eq. (4.10). When this happens, the frequency domain equation for the Maxwell-Ampère's Law can be reduced to eq. (4.11)

$$\frac{-\partial\mathbf{D}}{\partial t} = 0 \tag{4.10}$$

$$\mathbf{J} = \sigma\mathbf{E}. \tag{4.11}$$

Another important factor about a Frequency Domain study is use of the effective BH curve of a material as a substitute of its actual BH curve, section 4.5.1.

As some simulations require voltage or current values outside the normal operating zone of the stator's core BH curve, for example in the iron core validation experiments, this type of study is avoided and a more resource-consuming time-dependent study had to be performed. This difference in performance is relevant, as the computing time difference between studies can be as high as 15 times longer.

Effective BH curve

As measured in chapter 3, the stator of the machine shows a non-linear magnetic behavior, and although it could be simulated through its relative permeability, a better approach would be through the use of its magnetization curve. Whoever, this curve is highly non-linear and therefore increases the problem complexity, so a linearization of the BH relation would be ideal. This linearized curve is called Effective BH curve.

The used Frequency Domain studies, where all quantities are sinusoidal, use this effective BH curve instead of the original one, so a transformation is in place. From the several methods available, the Average Energy Method was the one used [9, 10]. This method relies on the conservation of the average magnetic energy between a real material, with a non-linear BH curve, and an equivalent material, with an equivalent linear B-H_{eq} relation.

As the magnetization voltage is imposed on the coils, with B the sinusoidal imposed flux density eq. (4.12), and H_{eq} the also sinusoidal resulting field intensity eq. (4.13)

$$B(t) = B_{eff}\sqrt{2}sin(2\pi ft) \tag{4.12}$$

$$H_{eq}(t) = H_{eff}\sqrt{2}sin(2\pi ft). \tag{4.13}$$

From the original BH curve, the average energy is calculated for a sinusoidal B with period T, while taking advantage of the quarter period present in this signal,

$$\left\langle \hat{W}_m \right\rangle = \frac{4}{T}(\int_0^{T/4} H(B)\cdot dB)\cdot dt. \tag{4.14}$$

Now, for an equivalent linear material where both flux and field quantities are sinusoidal, the average magnetic energy, i.e. the total magnetic energy stored in the will be

$$\left\langle \hat{W}_m \right\rangle = \frac{1}{2}\left\langle H_{eq}(t)\cdot B(t)\right\rangle = \frac{1}{4}\cdot\frac{B_{eff}^2}{\mu_{eq}}. \tag{4.15}$$

Finally, if we consider there is conservation between both energies, eqs. (4.14) and (4.15), μ_{eq} and H_{eq} become

$$\mu_{eq} = \frac{B_{eff}^2}{\frac{16}{T}\int_0^{T/4}(\int_{B(0)}^{B(t)} H(B)dB)dt)} \tag{4.16}$$

$$H_{eq} = \frac{1}{B}\cdot\frac{16}{T}\int_0^{T/4}(\int_{B(0)}^{B(t)} H(B)\cdot dB)\cdot dt. \tag{4.17}$$

For every imposed B the eq. (4.17) is used to calculate the respective H_{eq} and the final equivalent curve is created for the material in question, with B_{eff} the RMS amplitude of the applied flux on the vertical axis, and H_{eff} the RMS amplitude of the equivalent field intensity on the horizontal one. Figure 4.4 plots both normal and effective BH curves of the material.

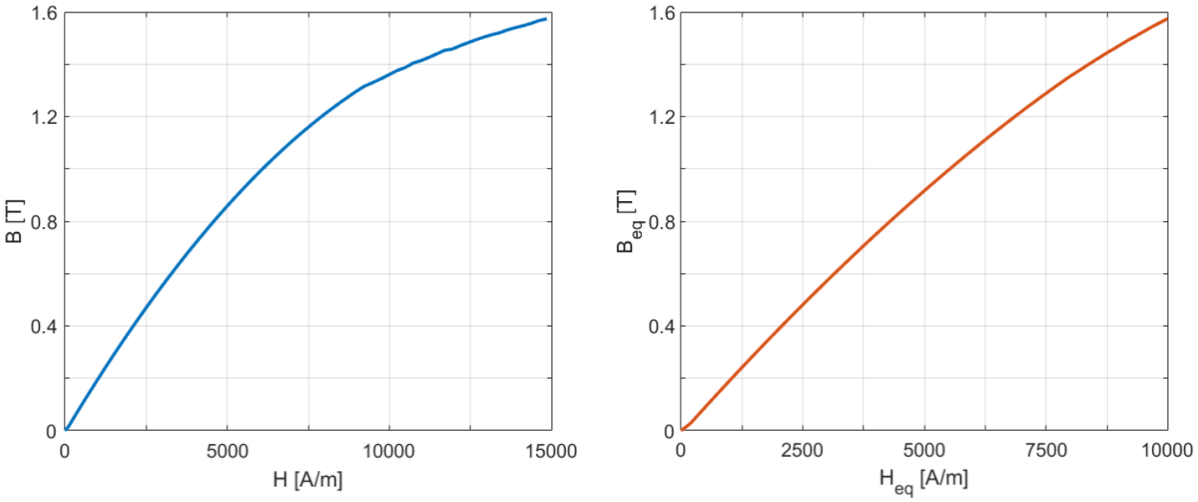

(a) stator core real BH curve

(b) stator core computed effective BH curve

Figure 4.4: BH and effective BH curves.

However accurate this method is when there is no significant saturation, outside the linear zone of the magnetization this method should not be used as the quantities stop being sinusoidal, as this method relies on the assumption that both B and H are sinusoidal. When saturation is reached, either the voltage or the current or both, stop being sinusoidal, and eq. (4.15) is no longer valid. However, as frequency domain studies are only valid when all quantities are sinusoidal, and the effective BH curve is only used by it, all simulations where saturation is achieved are performed with a time dependent simulation study.

4.6 Rotating Machinery study

The final type of simulations, Rotating Machinery Model (RMM), is the most complex of all, as this type of simulation uses a different type of physics interface, the rotating machinery 3D, where the rotor rotates at a fixed velocity. This velocity will in turn be used to calculate the Lorentz force density developed in the rotor. This study as a time-dependent type takes the highest computing time, so it is only used for a few simulations, where the mechanical behavior of the machine is also modelled.

4.6.1 Mixed formulation

This type of study was the last performed as its complexity far exceeds the previous ones, as a time dependent study with a moving mesh contains much more degrees of freedom than stationary or frequency domain studies. Adding to the increase of DoF, the Rotating Machinery study uses a mixed formulation to solve the Maxwell equations that make the model, where 2 different approaches are considered: the *vector potential formulation* (MVP) and the *scalar potential formulation* (MSP).

The *vector potential formulation* approach, defines the electrical field and the magnetic flux density as eqs. (4.18) and (4.19)

$$\mathbf{E} = -\frac{\partial \mathbf{A}}{\partial t} \tag{4.18}$$

$$\mathbf{B} = \nabla \times \mathbf{A}, \tag{4.19}$$

and the Maxwell's equations are solved in

$$\nabla \times \mathbf{E} = -\frac{\partial \mathbf{B}}{\partial t} \tag{4.20}$$

$$\nabla \cdot \mathbf{B} = 0 \tag{4.21}$$

$$\nabla \times \mathbf{H} = \mathbf{J}. \tag{4.22}$$

The *scalar potential formulation*, however, is only valid in regions where there is no current density, $\mathbf{J} = 0$. In these regions the magnetic scalar potential, V_{m} , is introduced and the magnetic field is defined as the gradient of this potential,

$$\mathbf{B} = \mu_0 \mu_r \cdot \mathbf{H} \tag{4.23}$$

$$\mathbf{H} = -\nabla \cdot \mathbf{V_m}. \tag{4.24}$$

This approach allows a much simpler solution, less computationally heavy, thus reducing the complexity of the model and a consequently faster solving time. However, the MSP formulation has the downside of only being applicable to very specific situations (no electrical current), meaning it will only be used in some air regions.

4.6.2 Rotating Mesh

The RMM simulation uses an imposed rotation to some parts of the model to calculate quantities related to movement of those parts and their velocity. In this case, the rotor is set to rotate at a fixed speed and the axial torque is computed, this way simulating the real behavior of the machine. This rotating movement of the rotor makes the mesh of the model to be different at every time step, as the

model needs to update the mesh at the new angular position.

The need for a rotating part of the model creates the need of a separation between fixed and rotating domain, and therefore two air volumes surrounding the model fig. 4.5: one stationary, in pink, involving the stator and the coils, and one moving, in orange, around the rotor. The increased complexity of the model caused further simplifications of the geometry, as the air regions had to be replaced by cylinders, instead of a sphere, and the infinite domain surrounding the air was discarded.

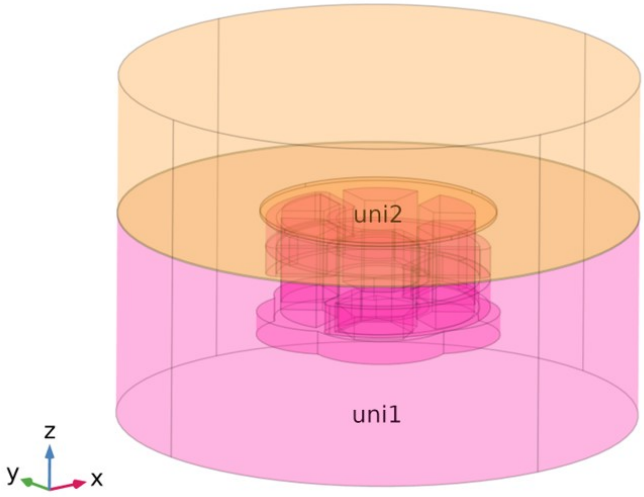

Figure 4.5: Rotating Machinery geometric model.

4.6.3 Materials and model setup

Despite the materials for this simulation being the same as the previous simulations, the iron alloy magnetic behavior (BH curve) was substituted for its relative permeability. As previously observed, the magnetic fields created by the stator are well within the linear part of the magnetization curve, and therefore the stator permeability can be approximated by its relative permeability. The air regions' electrical conductivity was also altered to 10 S/m to simplify the model, as a 0 S/m conductivity meant a more difficult solution for the Ampère's Law,

The model setup, although very similar to the frequency domain simulations, has some differences, mainly regarding the mixed formulation of the model, as each air region uses a different formulation: the magnetic flux conservation (MSP) for the top air, and the Ampère's Law (MVP) for the bottom air.

Ideally both regions would use the simpler scalar potential as it would simplify the solution, however the current flow inside the coils creates a current path and is therefore incompatible with this formulation. The boundary separating both regions is defined as a *mixed formulation boundary*, and the boundary between stationary and rotating parts is defined as a *continuity boundary*.

Chapter 5

Model Validation

As previously tested in [3], there are big discrepancies between the projected motor in [1] and the real constructed machine. So, after the modelling of the machine there is a need to validate the model and this way create a parallelism between both real and FEM models. Several experiments were performed, and the FEM model adjusted accordingly.

5.1 Experiment outline

The simulation performed was time-dependent with the BH curve calculated in the previous chapter. The reason for a time-dependent study is the need to recreate the laboratorial experiment with the most extreme conditions, the 196 V excitation experiment with stator and closed air-gap Somaloy®lead, section 3.3 , where the material saturates. This saturation, as previously stated, is not compatible with a Frequency Domain study as quantities become non-sinusoidal.

Following the geometry of the laboratory experiment, a simulation of this assembly was designed, fig. 5.1, with an alteration of the main motor geometry, as the experiment uses an auxiliary coil wound on one tooth of the stator and an alloy bulk between two teeth. This geometry was also modelled with the aid of a 3D CAD software.

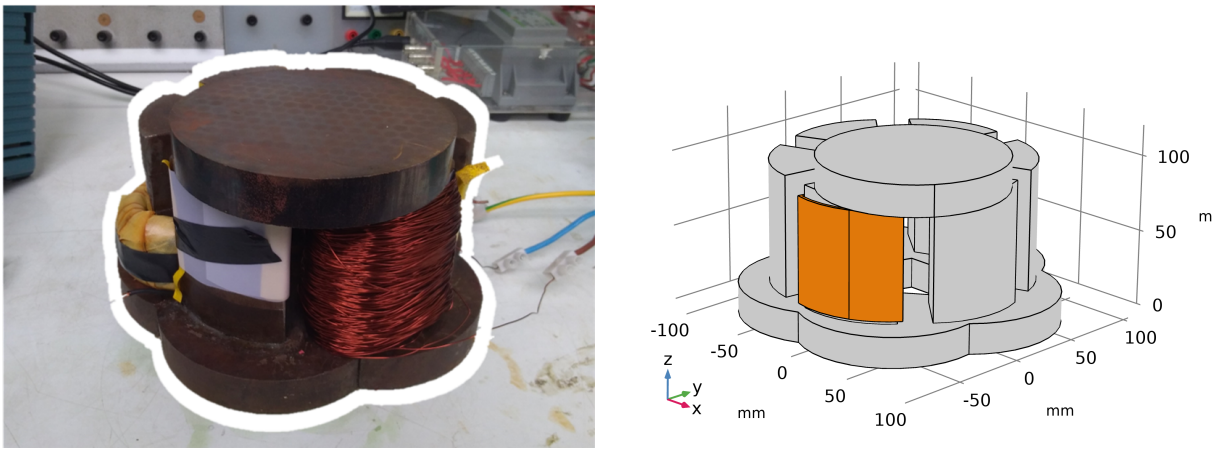

(a) laboratory assembly

(b) FEM model assembly

Figure 5.1: Real (a) and simulated (b) BH curve measurement assemblies.

The simulation was designed equivalent to the laboratory, with 200 turns copper coil and the iron alloy stator and cylinder lead. The iron alloy BH curve was the same calculated from the lab data, and the coil's excitation with the voltage from the laboratory, same waveform and amplitude, 196 V. This is important as the grid supplied voltage at the laboratory, fig. 5.2, is not completely sinusoidal due to harmonic distortion caused by nearby connected devices. The objective of this simulation is to model the real behavior of the machine at the laboratory by comparing both experimental and simulated signals, voltage and current.

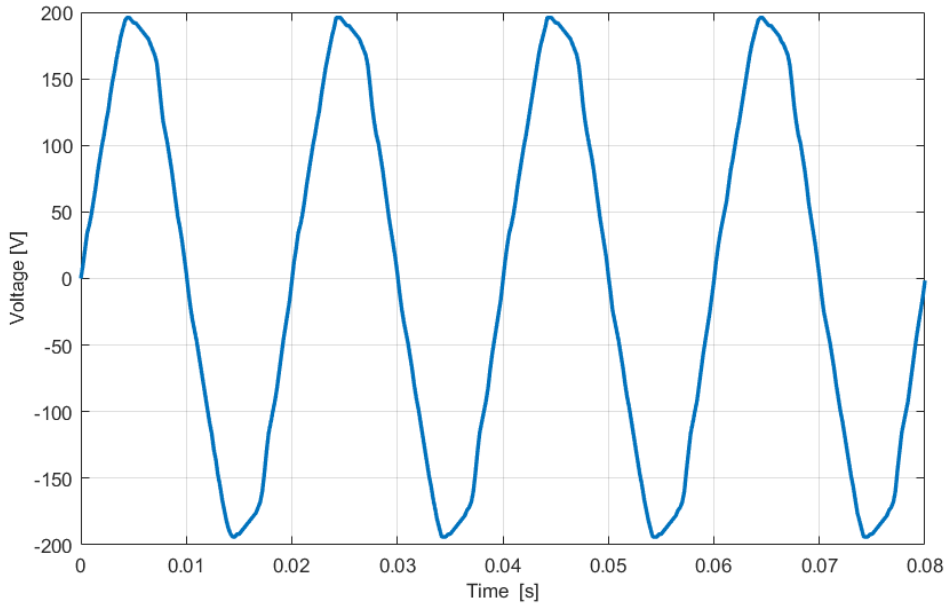

Figure 5.2: Laboratory grid voltage, 196 V.

5.2 Experimental and simulation comparison

5.2.1 No modifications

After simulating 4 cycles at 50 Hz, both laboratory and simulated voltage and current were plotted, respectively, in figs. 5.3 and 5.4.

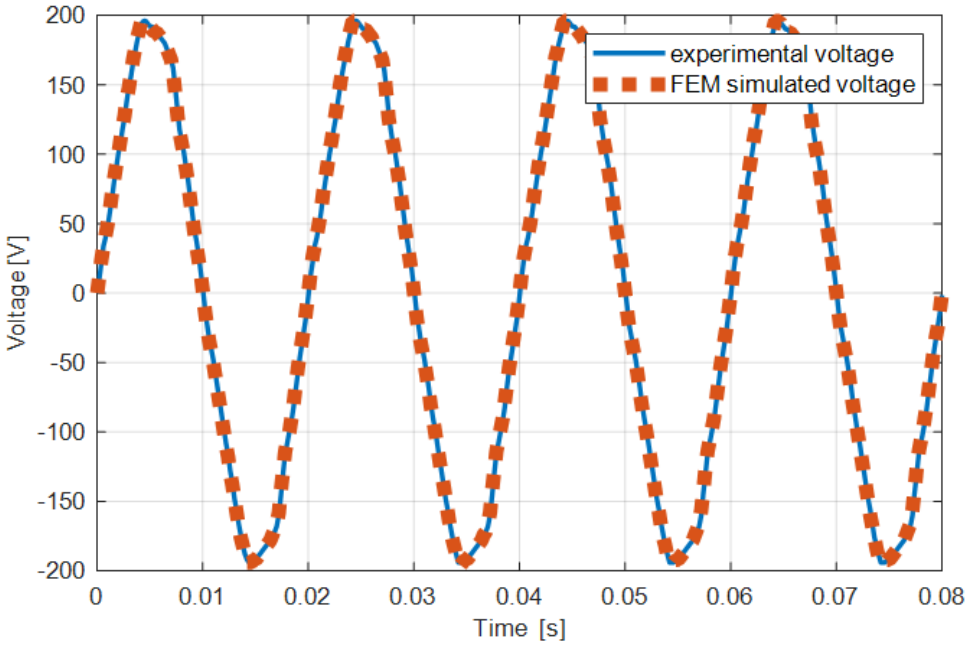

Figure 5.3: Laboratory and FEM simulation - voltage comparison.

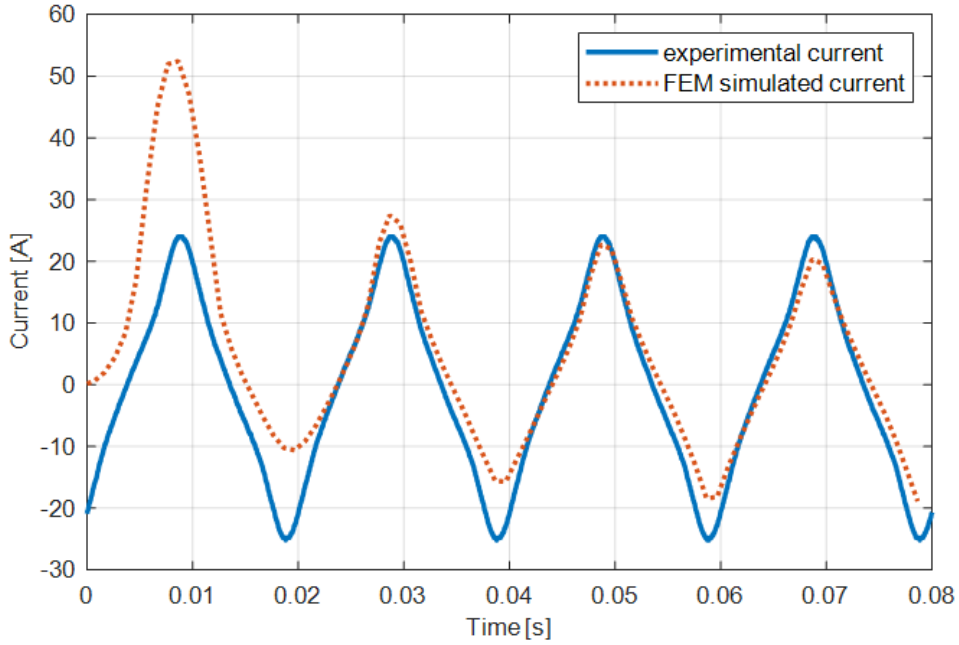

Figure 5.4: Laboratory and FEM simulation - current comparison.

In fig. 5.3 there is no visible difference between both voltages, as the coil excitation in the simulation uses the same exact voltage waveform as the experimental. In the current plot, however, fig. 5.4, the difference is quite visible. In the first 3 periods, the simulation is in the transitory regime, clearly visible by the 3 different amplitudes; in the fourth period, however, when stationary behavior is achieved, and not only the amplitude is inferior to the experimental, but also a difference in phase and form between signals. As a consequence, the FEM model isn't validated yet.

5.2.2 BH curve modifications

To solve the issues between current signals, an understanding of the causes for these differences is of great importance. However, as the geometry is identical to the real motor, and the coil's dimensions, number of turns and excitation are the same, the only variable left is in the magnetization relation of the stator core.

Since the air and copper in the model use standard relative permeabilities for each material, 1 for both materials, the only variable left is the stator's BH curve, which is in accordance with the previous findings. So, modifications in the software input curve is necessary. Besides, the BH curve relates both voltage and current (voltage with B and current with H), where the difference stays.

The current differences, phase, amplitude, and waveform need to be correct through the transformation of the original curve. These 3 factors are related to different zones of the curve: the phase difference between voltage and current is related to the derivative of the linear zone of the BH curve; the amplitude of the current, because there is no difference between voltage, it relates to the point of the curve where the imposed B is higher, $H(B_{\text{max}})$; and finally the waveform, that is related to the BH curve zone: linear, knee or saturation.

Firstly, the maximum imposed B by the voltage is calculated from the linked flux measured in the FEM software, and H'_{max} from the input curve

$$B_{max} = \frac{\phi_{max}}{S \cdot N_t} = \frac{0.624}{1.845 \cdot 10^{-3} \cdot 200} = 1.62\,T \tag{5.1}$$

$$H'(B_{max}) = 20,000\,A/m \tag{5.2}$$

$$H'_{max} \cdot l_{FEM} = N_t \cdot I_{max,FEM} \tag{5.3}$$

$$l_{FEM} = \frac{200 \cdot 24.04}{20,000} = 0.24\,m. \tag{5.4}$$

Now, with the equivalent length of the FEM magnetic circuit and the desired current amplitude, the new maximum field is calculated,

$$H(B_{max}) = \frac{N \cdot I_{max,exp}}{l_{FEM}} = 20,416\,\text{A/m}. \tag{5.5}$$

So, we know the new BH, regardless of its aspect, has a fixed coordinate: (20416,1.62).

Now, the phase difference is considered, as its relationship with the curve comes from the curve's linear slope, it will affect the final waveform. Both phase differences between each voltage-current pair is then $\varphi_{\text{exp}} = 74°$ and $\varphi_{\text{FEM}} = 79°$, a 5°difference. As the curve's slope is proportional to the inductance, there is a need to lower the inductance of the electric circuit. However, as tests were conducted, there was no possibility to achieve that lower inductance. The alternative found was an increase in the circuit's electrical resistance of the copper coil in the FEM model, lowering this way the overall phase difference,

$$\sigma_{Cu,FEM} = 0.7 \cdot \sigma_{Cu}. \tag{5.6}$$

As the current waveform relates to the curve's zone: more sinusoidal if closer to the linear zone, and less sinusoidal if close to the saturation. As the experimental current waveform is not sinusoidal, we know the fixed coordinated dictating the amplitude must be closer to the saturation than the linear zone. Finally, after several iterations and error measurements, the most fitting curve was found. Figure 5.5 plots both BH curves, fig. 5.6 plots the experimental and the simulated currents, and fig. 5.7 plots the error evolution between both currents in relation to the peak-to-peak amplitude.

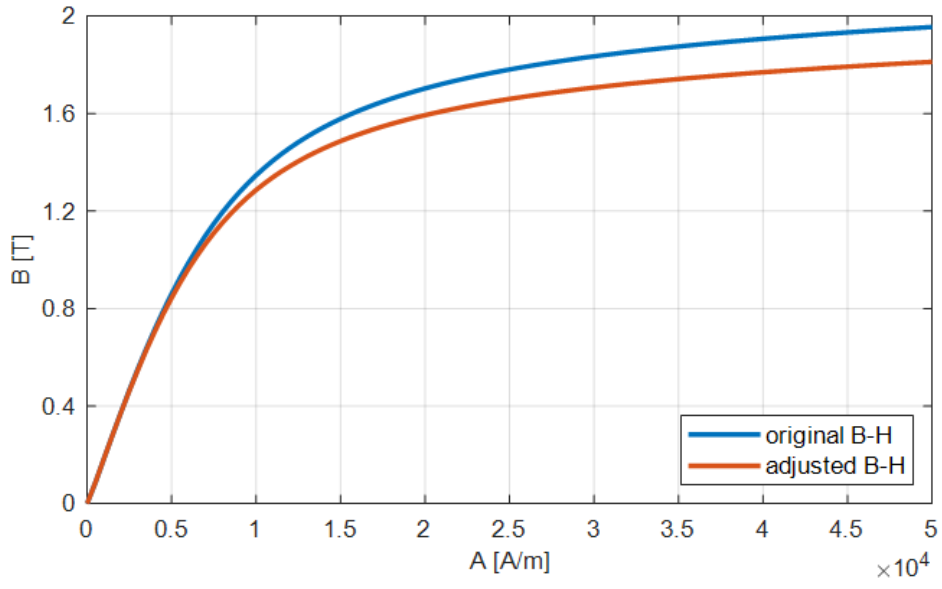

Figure 5.5: "Original" and adjusted BH curves.

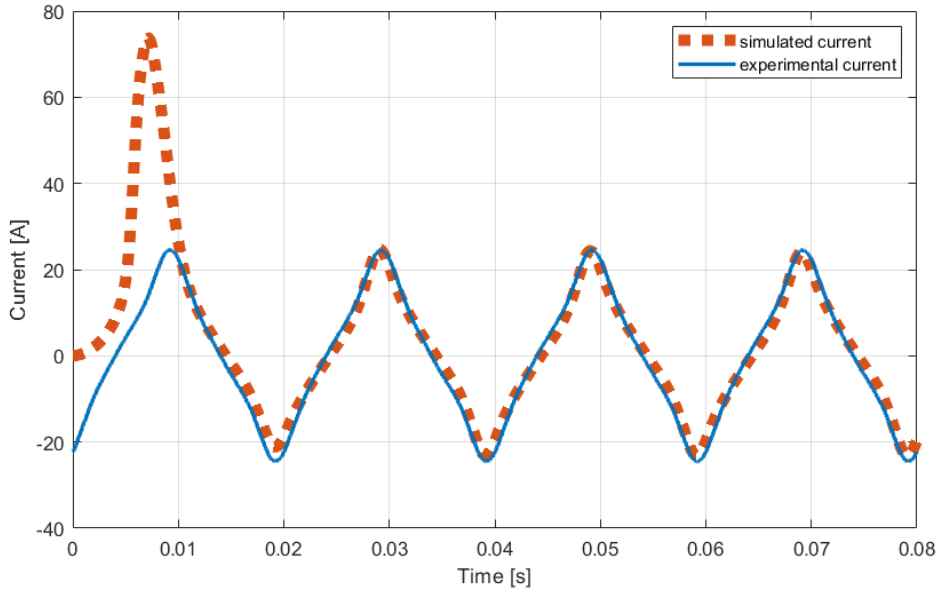

Figure 5.6: Laboratory and adjusted FEM simulation - current comparison.

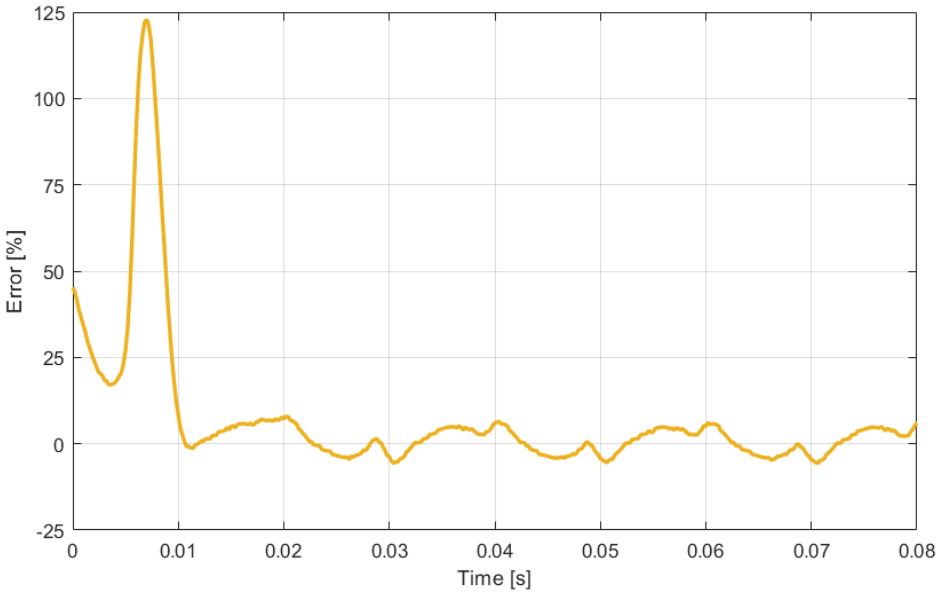

Figure 5.7: Laboratory and adjusted FEM simulation - relative current error.

From fig. 5.6 is clear the improvement in the current signal in all aspects: waveform, amplitude, and phase difference. fig. 5.7 plots the relative error evolution (in relation to the experimental amplitude). In the transitory, the relative error is maximum, as it is being compared with the experimental data that was measured in the stationary conditions, however in the stationary region the maximum error is 12% and the average error is 6%.

With no error in the voltage and a relatively small difference in current, the finite elements model is validated, and it is now safe to assume a parallelism between both models, real and simulated, has been created. The adjusted BH curves, time-dependent and effective, are plotted in fig. 5.8.

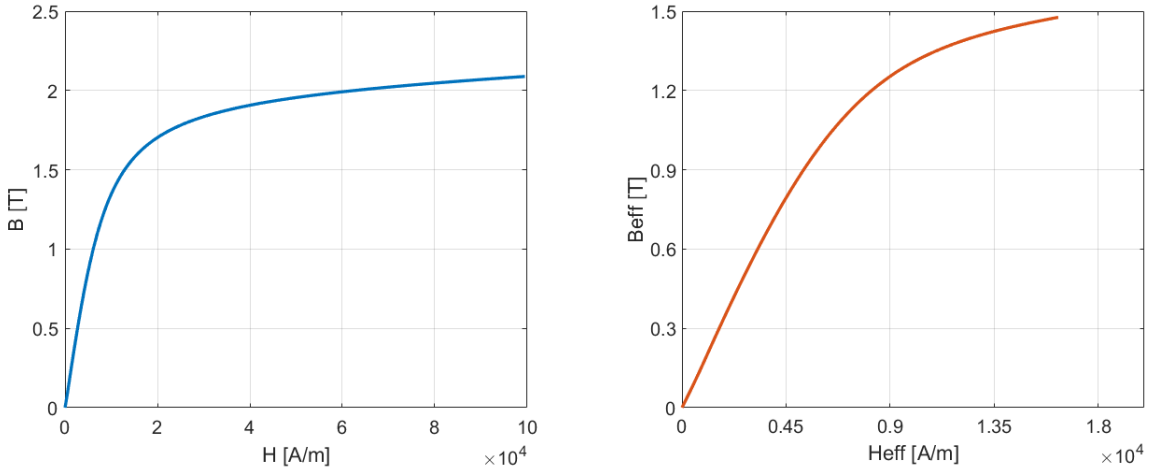

(a) adjusted BH curve

(b) adjusted effective BH curve

Figure 5.8: Adjusted BH and effective BH curves.

Chapter 6

Simulation Results

Having the FEM model validated, there is an equivalence between the simulation and the real motor. This parallelism is very important, as physical experiments are more expensive than simulated ones when it comes to experimenting new materials and different coil geometries, and also the existing limitations in the laboratory, like the available maximum voltage and temperature damage to materials, which in turn are easily overcome with the numerical model.

Several simulations were then run, most of them with a blocked rotor, for the electromagnetic study of the machine, with an emphasis on the stator study, as the behavior of the magnetic field there created will dictate the functioning of the machine. As explained in section 4.5.1, most simulations were performed with a frequency domain study, as the motor is designed to function within its materials' normal operating conditions, i.e. within the linear zone of their BH curves and therefore all quantities will remain sinusoidal.

After the first set of frequency domain studies, some experiments were performed with the rotating machinery physics and solved time dependent studies. However, due to some inconsistencies in the stator's magnetic penetration, these results can only be appreciated as qualitative, not quantitative. At last, the final simulations were again frequency domain studies, however now with several modifications to the machine's coils and rotor. The rotor modifications regard its thickness, and the coils modifications regard its geometry, pair of poles and number of turns.

6.1 Frequency Domain – Blocked Rotor 3 mm 50 Hz

The first experiment performed was a blocked 3 mm rotor with a 50 Hz, 20 V, 3-phase excitation. This study simulates the laboratory conditions for the machine, with the objective of studying the stator, coils and rotor.

6.1.1 Stator and Coil Analysis

In fig. 6.1, the total current density inside the coils is plotted, with its color scale on the right; these values represent the amplitude of the sinusoidal quantity. From the figure it is quite visible a discrepancy in values between each coil, which is a result of the height difference between them, as the higher positioned coils have a smaller inductance, as there is less leakage. Table 6.1 shows each coils' parameters given by the numerical model: voltage, current, resistance and equivalent inductance.

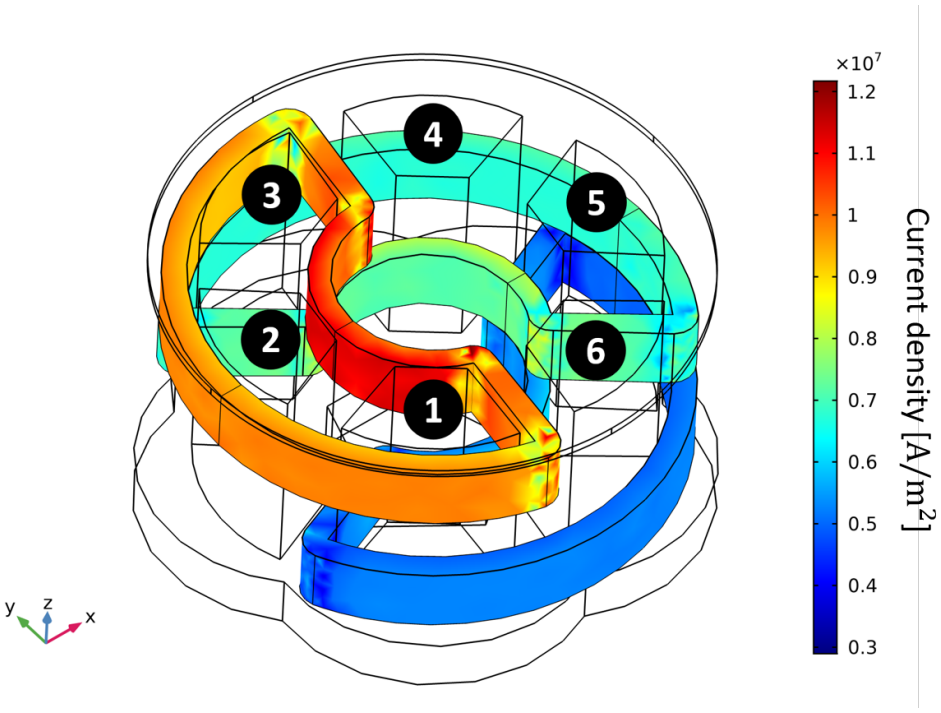

Figure 6.1: Coils current density distribution for 3-phase 20V excitation.

	Voltage [V]	Current [A]	Resistance [Ω]	Inductance [mH]
Top coil	20	$35.8e^{-49^\circ}$	0.37	1.33
Middle coil	$20e^{-120^\circ}$	$26.1e^{+174^\circ}$	0.32	2.21
Bottom coil	$20e^{+120^\circ}$	$19.2e^{+47^\circ}$	0.31	3.17

Table 6.1: Coils' parameters.

From table 6.1 inductance values, it is now very visible this difference. The top coil has less than half the inductance of the bottom coil, which is undesirable in any symmetrical machine. As these coils are responsible for generating the magnetic flux in the stator, the more different the coils are, the more different these fluxes will be, which in turn will cause a non-radial symmetry in the air gap of the machine. Already from the first simulation it is visible a possible origin for the poor behavior of the machine, as the magnetomotive forces generated by each coil are so different, section 6.1.1, the resulting magnetic field by them generated will suffer from this,

$$F_{mmTOP} = 35.8 \cdot 60 = 2148\ A/t \tag{6.1}$$

$$F_{mmMID} = 26.1 \cdot 60 = 1566\ A/t \tag{6.2}$$

$$F_{mmBOT} = 19.2 \cdot 60 = 1152\ A/t. \tag{6.3}$$

Next in fig. 6.2, maintaining the same 3D orientation, the magnetic flux density norm of the stator is evaluated volume-wise. This flux as previously mentioned comes from the coils, and therefore is expected not be equal between all teeth.

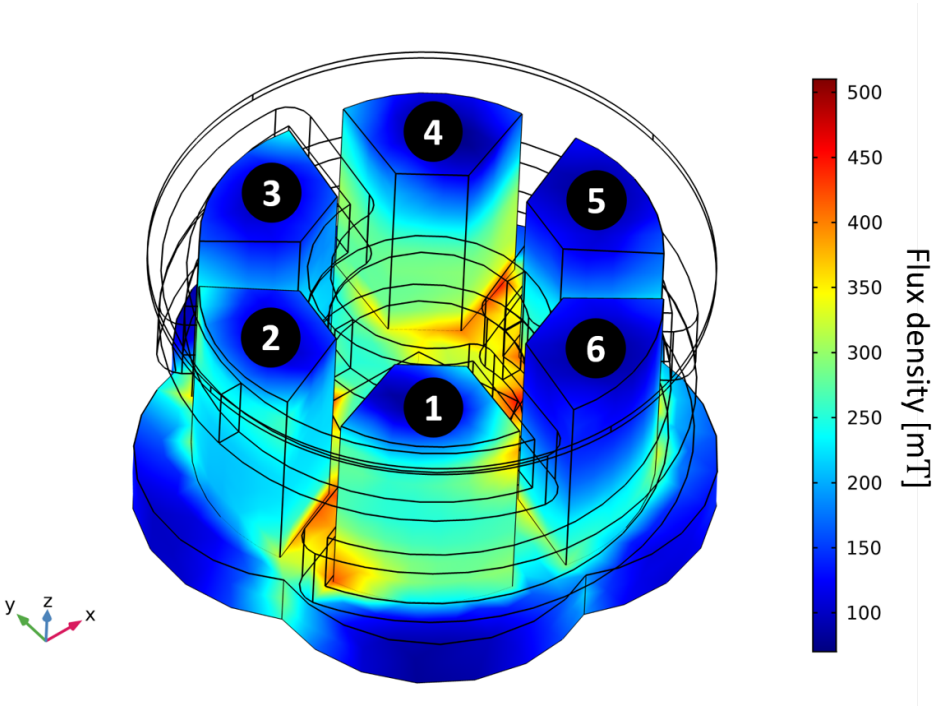

Figure 6.2: Stator surface magnetic flux density norm.

Now, even though only teeth 1, 2, 4 and 6 are visible, several aspects of the magnetic behavior of the stator can be inferred. The first one is the difference in flux in each tooth depending on the coil's position. In tooth 1 we can observe at the bottom left side there is a big flux concentration, with values more than double than its opposite side, only few centimeters apart. Whereas in tooth 2, there is no visible flux concentration, although most of its surface shares a similar color hue with the first. In tooth 6 however, not only there is no area with a flux concentration like in the first, but also its main color is much darker and very close to the minimum values of 100 mT.

These differences in flux distribution are a direct result of the coils wrapping the teeth, for example as tooth 6's flux is generated by the bottom coil, with lower inductance, and consequently current density, whereas tooth 1's flux is generated by both the bottom and top coil. In addition, tooth 1 is surrounded by each coil in three of its faces, all four sides combined; furthermore, both coils inner corners wrap the tooth, creating the high flux concentration areas of the tooth. Tooth 6 however, besides being only "touched" by the bottom coil, it is only wrapped by it in two of the faces, and has no corner of the coil to create the flux concentration. As a consequence, by just comparing these 3 teeth flux densities, the effects of the coil's disposition are already visible and relevant.

Despite the importance of the total flux distribution on the stator, the air-gap flux is the one responsible for generating the rotor's current density and ultimately, the torque developed. Figure 6.3 plots the absolute value of the vertical component of the flux density at the top surface of the stator, B_z.

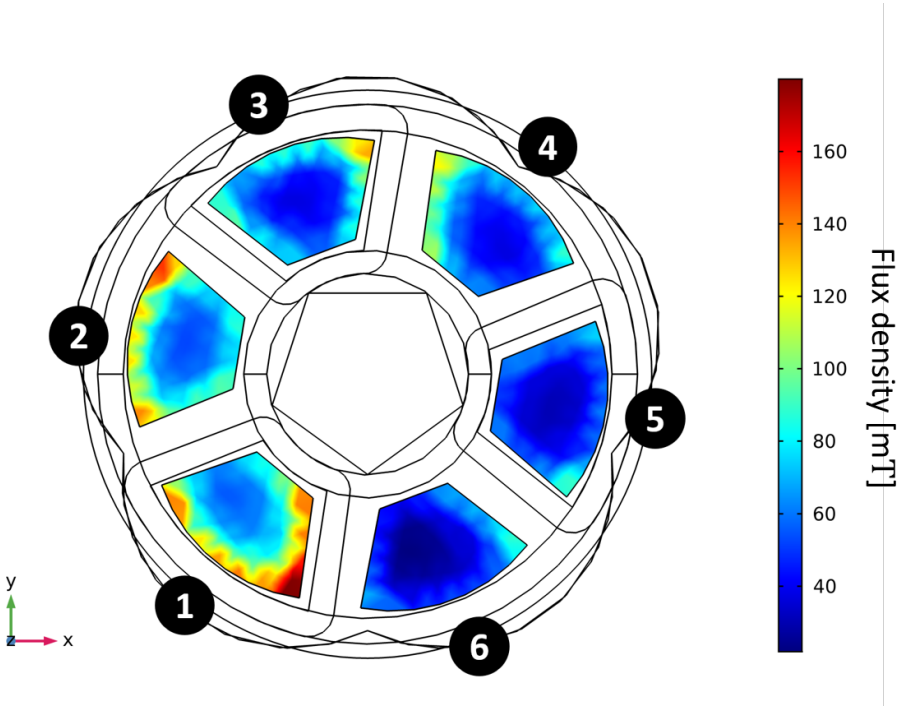

Figure 6.3: Stator top surface magnetic flux density z-component.

In fig. 6.3 we can see with more precision the exact flux z-component distribution at the stator's surface, whose values are much smaller than the total flux. These surface values are less than 25% the

maximum values of the total. However, the most relevant fact rests on the flux distribution which, as a consequence of what mentioned before, makes the difference in flux distribution in each tooth is very big. In tooth 1, B_z values range from 60 to more than 170 mT, whereas in tooth 6 they don't surpass 90 mT. Not only the range of value in one tooth is very big, not desirable when designing a balanced machine with a supposed radial symmetry, but most important the absolute values of B_z are very small, with average values ranging 43 mT (tooth 6) to 94 mT (tooth 1).

Now, only from the stator and coil analysis it is already possible to make some assumptions about the poor magnetic performance of the machine:

- The few number of coil turns and the low current causes the available magnetomotive force to be very small.

- Secondly, the low relative permeability of the stator, measured 141 instead of the manufacturer's 850, causes the flux to be 6 times smaller than originally designed.

- Finally, the electrical conductivity of the stator core of 5,000 S/m, despite a low value, causes induced Eddy currents in the teeth that cancel the desired vertical flux, forcing the available flux at the top even lower than it could be.

After the stator and coil analysis, most of the machine's flaws are already identified: firstly, the air-gap flux generated at the stator, responsible for generating the rotor's induced currents and the magnetic flux density, was proven to be very small. Usually, the flux density is between 1 and 2 T for a similar size machine (10/20 times higher the measured values), so the rotor induced currents will in turn be small as well. In section 6.1.2 these currents are analyzed.

6.1.2 Rotor Analysis

Figure 6.4 represents the norm of the induced current density in the x and y-axis. The z-axis component is neglected as the rotor's developed torque is a result of the cross product between the vertical flux, B_z, and the rotor's induced current density plane normal to it, J_x and J_y.

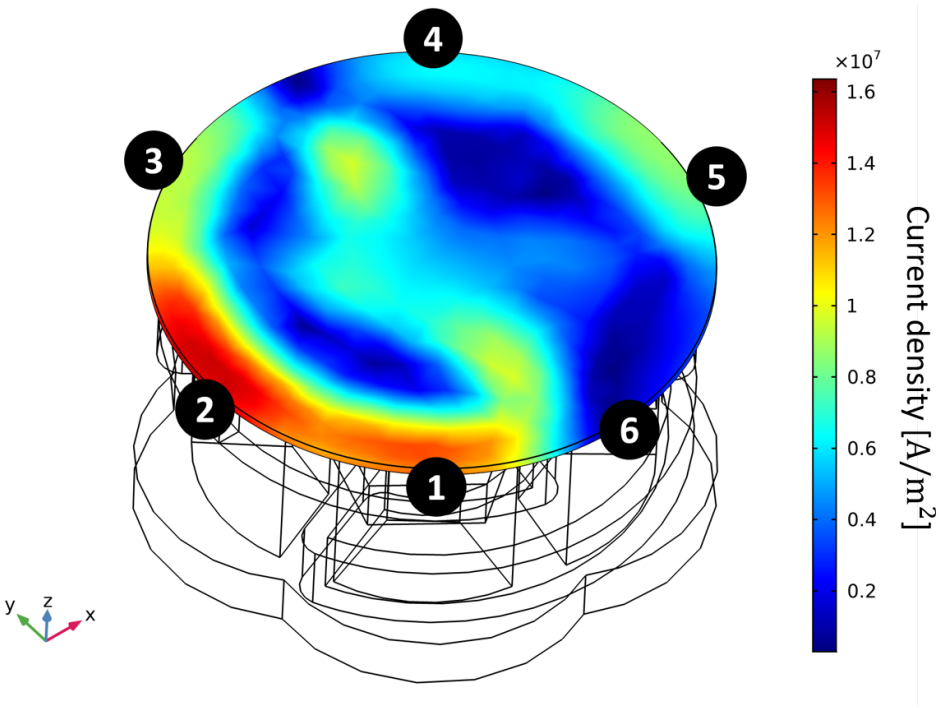

Figure 6.4: Rotor induced current density norm for the x and y-components.

The current density in the rotor is induced by the vertical flux density in the air gap above the teeth top surface and, as we can observe infig. 6.4, it is highly concentrated around the edges of the rotor, right above the teeth. This is a direct result of the flux density being much higher in the teeth edges, as shown in fig. 6.3. As expected, there is a big disparity in the values in the figure, an 8 times difference above teeth 2 and 6, as a result of the coils' positioning. Due to this uneven J distribution, the machine is very unbalanced, which will create forces in the rotor that are not axial, and consequently create vibrations on the rotor, which have already been observed in the laboratory, even more with the additional iron plate rotor, as an additional force pulls the rotor, due to the magnetic attraction between the iron ferromagnetic, and the flux.

After the stator and rotor analysis, the axial torque and the 3 axial components of the force in the rotor were calculated by the software, visible in table 6.2 and fig. 6.5. These forces are the axial torque and the x, y and z components of the Lorentz force.

axial Torque	Force x-component	Force y-component	Force z-component
0.16 Nm	2.01 N	1.33 N	15.78 N

Table 6.2: Rotor developed forces: axial, and Lorentz x, y and z-components.

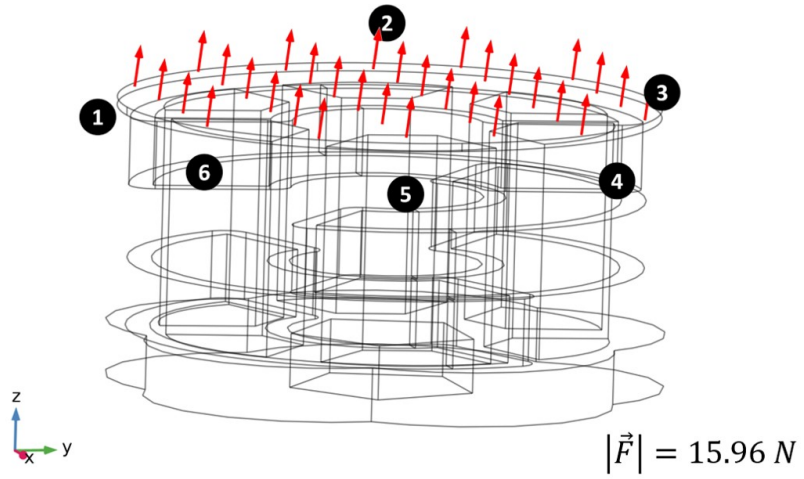

Figure 6.5: Rotor developed force vector.

The axial torque, responsible for the rotation of the machine, is a combination of both x and y-axis components of the force, and the z-component is responsible for the vertical movement of the motor, in this case positive. This translates to a force pushing the rotor away from the stator, in this case a force practically 10 times higher in the vertical direction, quite visible in fig. 6.5, unwanted, than in the horizontal plan, wanted. This upward is a result of the induced currents that create an opposing magnetic field, which creates a repulsion between them.

This, is a consequence of the type of machine designed, as non-axial flux machines have its rotor surrounded by magnetic field, instead of being above it. This repulsive force is therefore canceled as the field rotates. Consequently, this force can be neglected in non-axial flux machines.

Another important aspect is the axial torque value being very small, with a total developed force at the edge of the rotor of 1,6 N. This number is rather small when considering the machine's dimension and weight, as, however, this was already expected, as the machine's magnetomotive force generated by the coils and the stator core's permeability are very low. Due to being a blocked rotor simulation, these studies cannot predict the torque behavior of the machine at a real speed, their purpose is just the analysis of the electromagnetic behavior of the machine.

6.2 Frequency Domain – Blocked Rotor 3 mm 5-60 Hz

The second test was done for the same rotor thickness; however, the electrical frequency was varied between 5 and 60 Hz. This was done in order to vary the flux, while maintaining the same input voltage.

This works with the same principle as the Scalar Command of an induction motor, where the air-gap flux of the machine,eqs. (6.4) and (6.5), is maintained by preserving the relation between the input voltage and frequency, as it is proportional to this, eq. (6.6),

$$\mathbf{U} = j\omega L \cdot \mathbf{I} \tag{6.4}$$

$$L \cdot \vec{I} = \mathbf{\Psi} \tag{6.5}$$

$$|\mathbf{\Psi}| \propto \frac{|\mathbf{U}|}{\omega}. \tag{6.6}$$

So, as the flux created by a coil is inversely proportional to the its frequency, the lowering of the frequency will increase the flux, and theoretically increase the motor's torque output. Figure 6.6 plots B_z, for 3 frequencies: 5, 30, and 60 Hz.

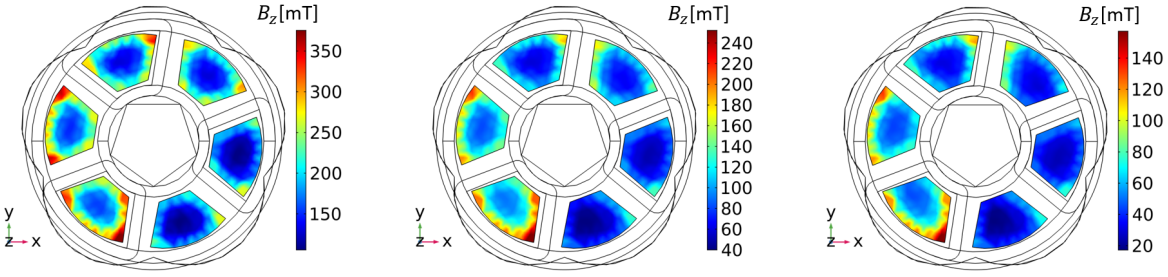

(a) B_z top view - 5 Hz (b) B_z top view - 30 Hz (c) B_z top view - 60 Hz

Figure 6.6: Stator top surface $\mathbf{B}_z$ for 5 (a), 30 (b) and 60 Hz (c).

It is possible now to observe in the 3 scales the difference in ranges: for 5 Hz, flux can be as high as 4 times the 60 Hz one, while maintaining a very similar distribution. This is a direct result of flux relation with the frequency, eq. (6.6), as we lower the frequency and maintain the voltage, the flux increases. Figure 6.7 plots the total flux density at the surface of the stator for the frequencies set. With a higher flux, a higher torque is also developed. Figure 6.8 plots the developed starting torque of the machine for frequencies between 5 and 60 Hz. Once again, as these results regard the torque with a blocked rotor, they cannot be extrapolated into a normal operating torque, they are only valid for the initial startup of the machine.

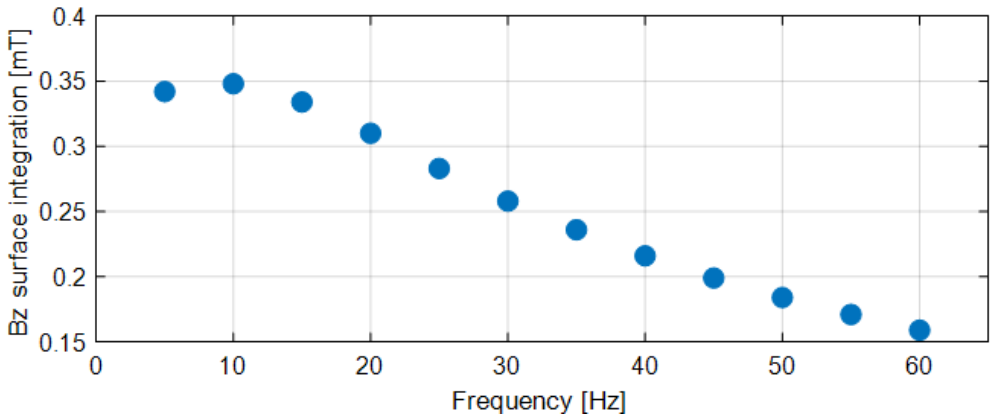

Figure 6.7: Stator top surface total $\mathbf{B}_z$ for [5;60] Hz.

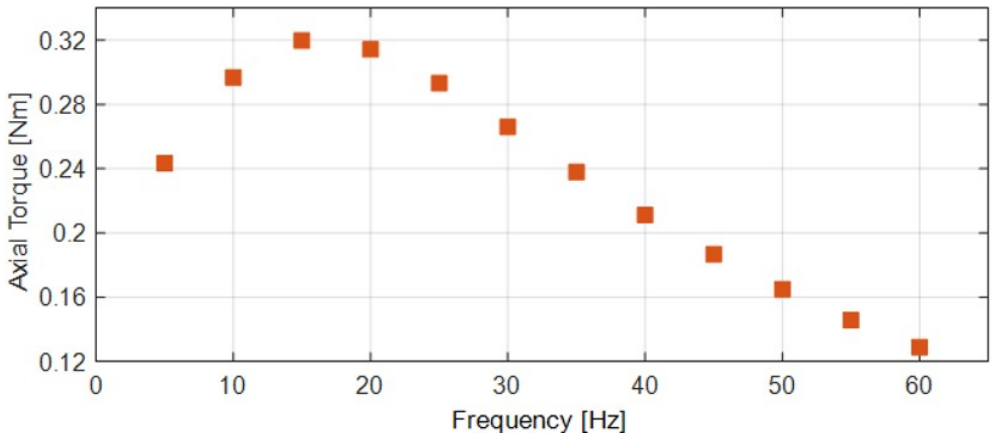

Figure 6.8: Rotor starting torque for [5;60] Hz.

Analyzing both figures, one verifies the almost perfect correlation between the stator's top surface flux and the rotor's developed torque. However, as these cannot be considered as the nominal torque of the machine, or even be considered proportional to it, the mechanical output of the machine P_{mech} cannot be computed. This output, as it is dependent on the mechanical velocity of the rotor, eq. (6.7), for both simulations is 0 W.

$$P_{mech} = \tau \cdot \omega_{mech}. \tag{6.7}$$

6.3 Rotating Machinery vs Frequency Domain blocked rotor

From the previous simulations using the frequency domain physics, some limitations were found, as this model not only works exclusively with sinusoidal quantities, but also is incompatible with any movement. As movement can only be applied on a 2D model, not a 3D like the real motor, the rotating machinery physics with a time-dependent study was chosen. It solves both limitations of the previous simulations: quantities can be non-sinusoidal, and rotational movement can be simulated. The first RMM simulation is then a 50 Hz 3-phase 20 A excitation with a blocked rotor.

Now both simulations, frequency domain (FD) and rotating machinery (RMM) time-dependent simulations can be compared.Figure 6.9 plots B_z for both cases: on the left, the RMM time-dependent at 18.8 ms, and on the right, the frequency domain at 338°, the equivalent phase as in eq. (6.8)

$$\varphi = \frac{18.8}{20} \cdot 360^\circ = 338.4^\circ \tag{6.8}$$

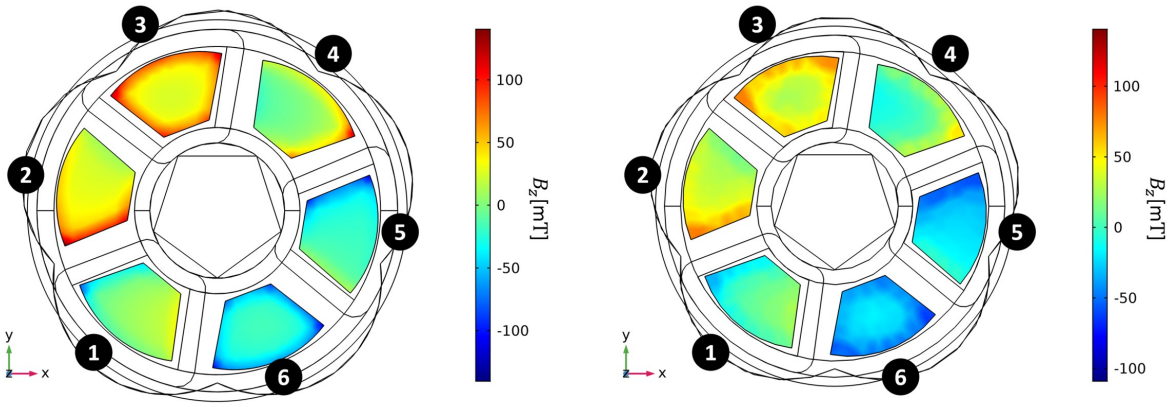

(a) RMM B_z (b) FD B_z

Figure 6.9: Rotating machinery (a) and frequency domain (b) top surface flux density z-axis.

Looking at fig. 6.9 it is visible the difference between both simulations, as the amplitude and magnetic penetration between both figures are quite different. In the RMM simulation, (a), the magnetic field generated by the coils penetrates the stator teeth much less than in the frequency domain simulation, (b). This is a result of the model setup itself, section 4.6.1, where the Ampère's Law, MVP, is used to solve the stator domain. This formulation, despite being used in both physics, stationary frequency domain, and rmm time-dependent, uses an additional domain condition as to improve the convergence of the solution, the gauge fixing for A-field. This condition, despite improving numerical stability, alters the magnetic behavior of the material. However, without it the available computing power is not capable of solving the model. With higher computing power, the software should be able to solve the model without this condition.

Due to this, all rotating machinery simulations have to seen only as qualitative, as there is no equivalence between the values in both types of simulations. In fig. 6.9 we can see an almost identical behavior on the outer edges of each tooth, with a variation only on the values itself, visible in the colors. However, in the center of each tooth, the values itself are very different, as the teeth on the left, RMM, have almost all the same values of flux density, with a similar green color in all of them.

Consequently, this type of study will only be used to analyze the magnetic behavior of the machine with the moving rotor, regardless of the error in values. The rotating machinery FEM model is then used as an approximate qualitative model of the moving motor, as the magnetic behavior is similar to the stationary frequency domain model, different on the values only. This will be useful to analyze how the magnetic fields change with the rotor speed, and how the flux in the air-gap travels in time, not only in frequency.

6.4 RMM clock/anticlockwise 2900 RPM

As an electric machine can work both as a motor or a generator, depending on the rotational direction or velocity, the first simulations were performed in opposing directions at the same imposed speed. These simulations are also important as the RMM FEM works by imposing a fixed speed on the rotor. These 2 simulations were run at 2900 rpm, 3-phase 20 A 50Hz, in both rotating directions, for 1 cycle, fig. 6.10. The use of 20 A excitation instead of the 20 V rests on the fact that current excited simulations are less compute-intensive than voltage excited, and despite a same current excitation on the 3 coils implies 3 different voltage values, the magnetomotive force on the coils is more uniform.

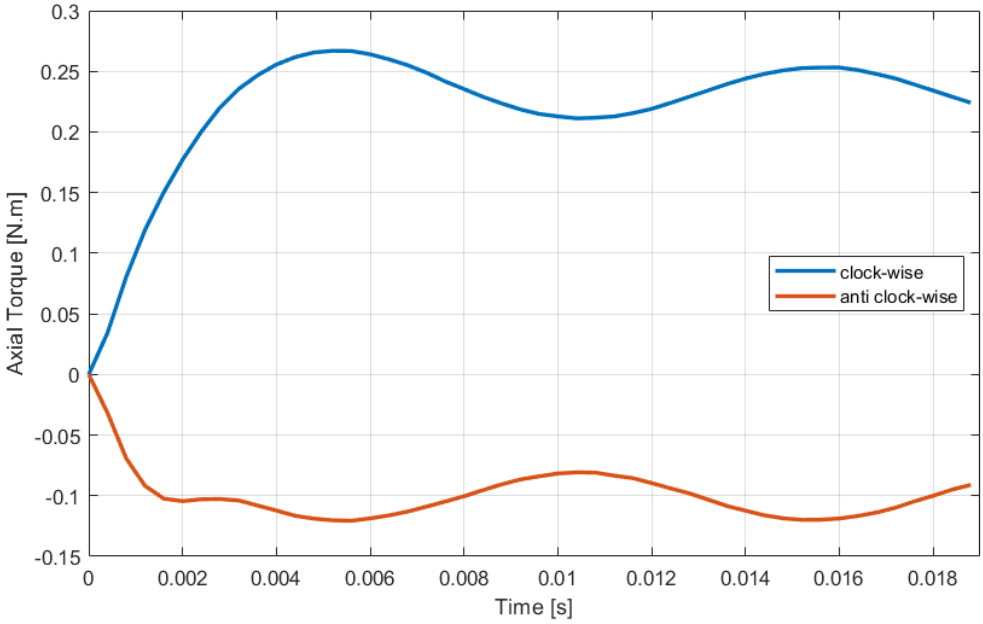

Figure 6.10: Motor axial torque @2900 RPM for clock/anticlockwise directions.

Now, with the rotor developed axial torque for both directions, the rotating direction's behavior can be analyzed and from the sign of the quantities, positive for blue and negative for orange, the motor and generator directions can be identified. As the machine either develops torque in the imposed motion's rotation (the torque output is positive), or it develops torque in the opposing direction, and acts as a break for the rotor (the torque output is negative). With a known motor direction, the next simulations were all computed in the same direction.

6.5 RMM 2 cycle 2900 RPM

6.5.1 Torque analysis

After defining the direction of the rotation, a 2 cycle simulation was performed at 2900 rpm, a speed close to a nominal operation of a typical 50 Hz 1 pair of poles machine. The coil current excitation is the same as in section 6.4, 3-phase, 20 A, 50Hz. The torque evolution of the machine is plotted in fig. 6.11.

In the figure we observe that a stationary behavior is achieved after 10 ms, half-period, which means the model does not depict the full study of the machine, only the steady state operation. This happens as the coils are excited with current, instead of a normal voltage excitation, as voltage excited coils would show a current transitory. However, voltage excitation simulations are more complex, so the alternative current excitation was used. Although the start-up of the machine cannot be studied with this model, the normal operation of a machine is in a stationary regime, and therefore the model is fit for this type of study.

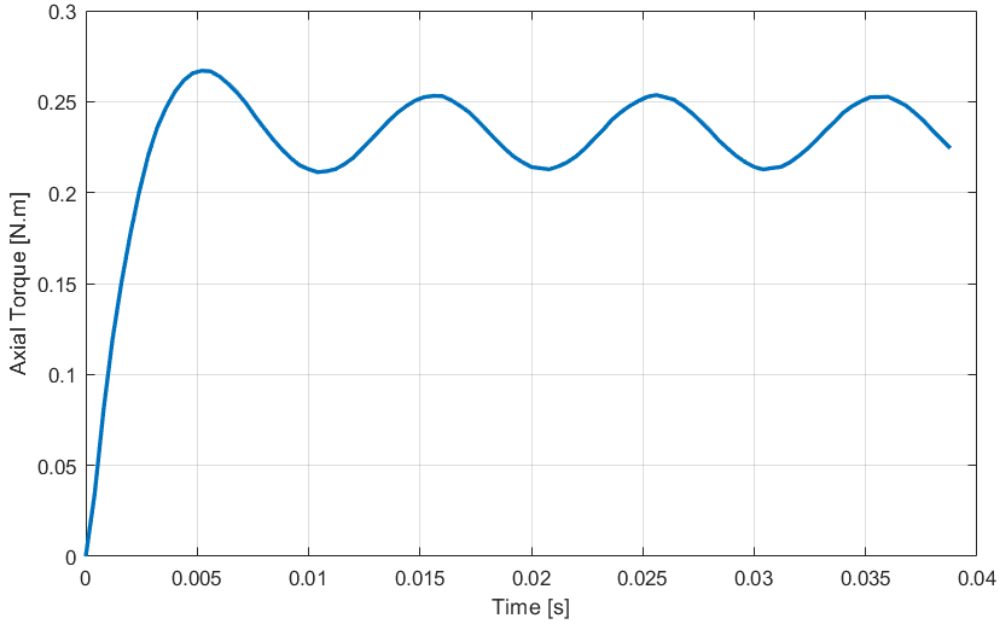

Figure 6.11: Motor axial torque @2900 RPM for 2 cycles.

max torque 1	min torque 1	max torque 2	min torque 2	max torque 3	min torque 3
0.27 Nm	**0.21 Nm**	**0.25 Nm**	**0.21 Nm**	**0.25 Nm**	**0.21 Nm**

Table 6.3: Axial torque local maximums and minimuns.

Table 6.3 depicts the sequential local maximums and minimums of the axial torque for the 2 periods study; from there, the conclusion that the average torque of the machine will remain constant over time, and it can be calculated accurately with only 1 period simulations. This conclusion is important as each 20 ms of simulation, one 50 Hz period, takes approximately 24 hours of computing power.

The torque behavior of the machine alone is not sufficient to accurately model the real motor. In fact it is a consequence of the two most important quantities in an electrical machine. The travelling magnetic field in the air-gap of the motor, responsible for not only bridging the stator and the rotor, but also for inducing the current density in the rotor. So, a further analysis of these quantities is due.

6.5.2 Magnetic field analysis

As the most important quantity to be analyzed is the magnetic field at the top of each stator tooth, the magnetic field density in the vertical direction, B_z , is calculated and plotted for 6 equally time-spaced instants, fig. 6.12, starting at t_0=17 ms, the time where the flux density is higher, in the middle tooth of the top coil. The ideal behavior of the machine is an even B_z distribution at each top surface, and similar values for each instant. However, this was not verified.

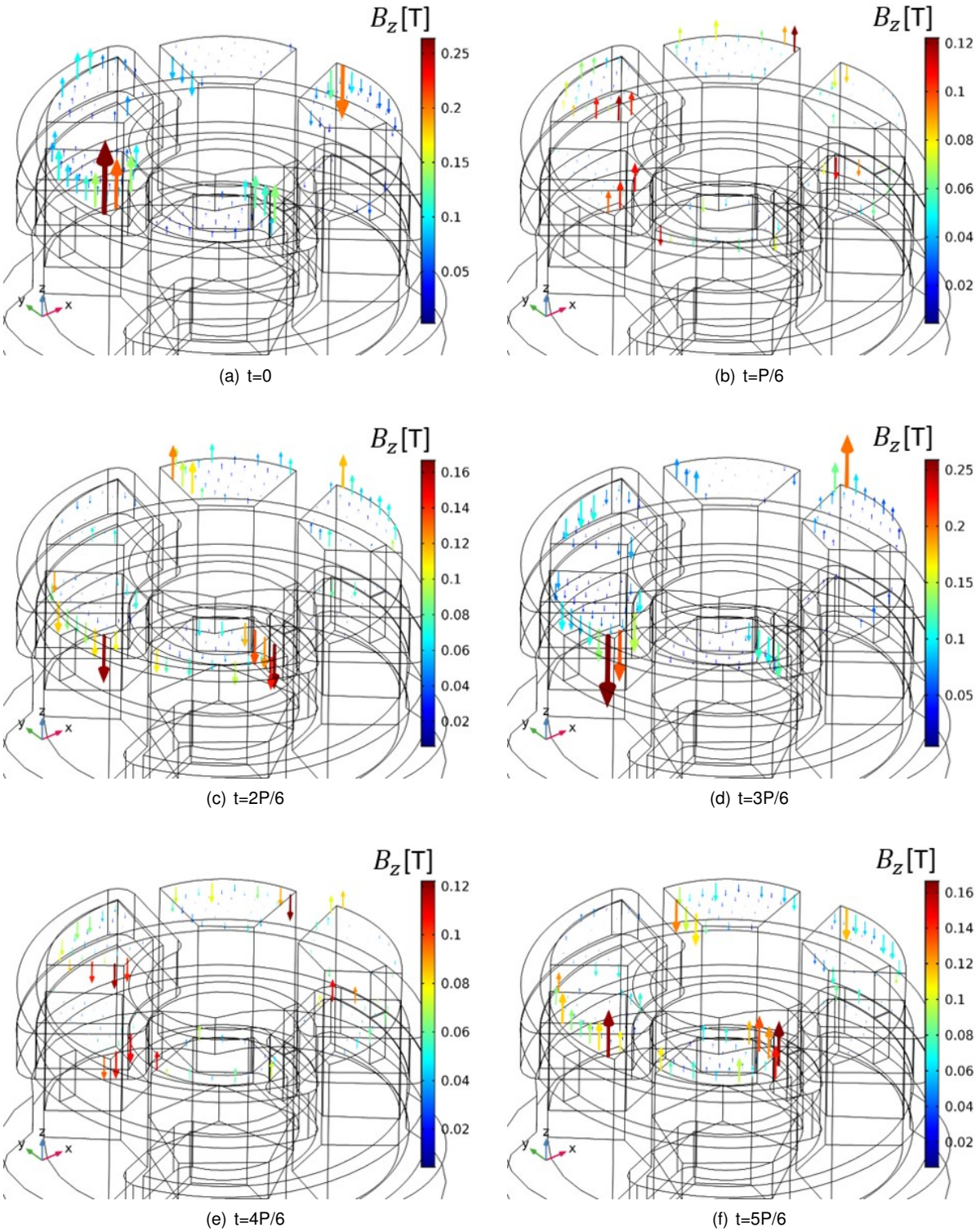

(a) t=0 (b) t=P/6

(c) t=2P/6 (d) t=3P/6

(e) t=4P/6 (f) t=5P/6

Figure 6.12: $\mathbf{B}_z$ top surface @2900 RPM 6 times.

From these images it is evident the unevenness of the surface in each tooth, quite visible in the first image where the flux density varies between 50-250 mT in the same tooth, and in the opposing between 0-200 mT in the negative direction. From this sequence it is also clear the magnetic field distribution is not equally spaced. So, a new plot was created, fig. 6.13, that depicts the average surface value of the flux density for each tooth in the same period, t=[17;37] ms.

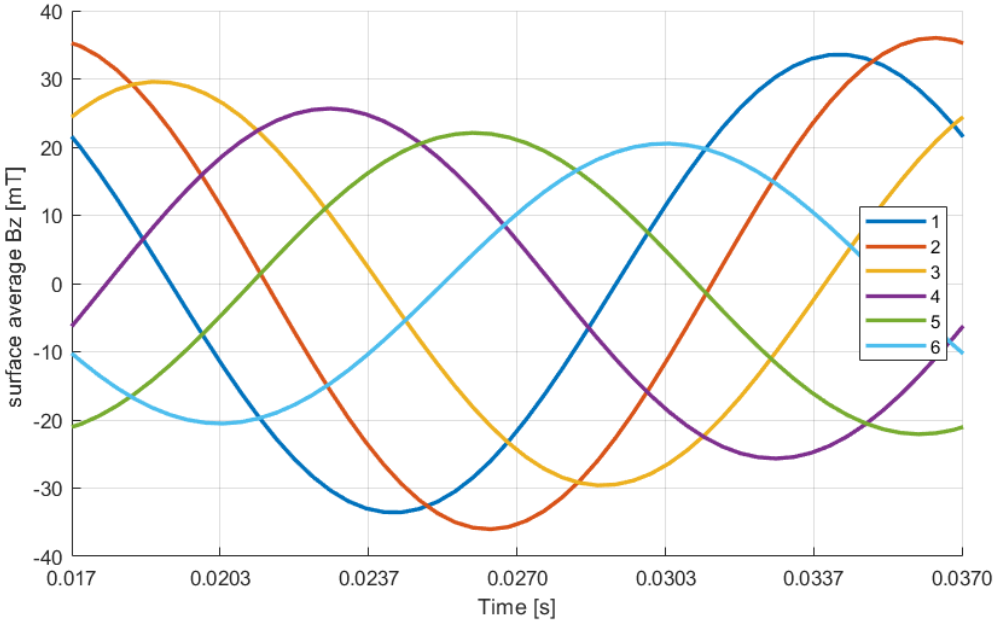

Figure 6.13: Average $\mathbf{B}_z$ per tooth for one 50Hz cycle.

From this figure, we observe the variation of each surface in time. Despite each tooth displaying an almost sinusoidal flux density normal to its top surface, the maximum value for each is quite different; and in turn the resulting field is not sinusoidal. This is a direct result of the height difference of the coils, as the top-most coil generates a flux density of 36 mT at its peak in the 2nd tooth, and the bottom coil highest value only 22 mT; a significant difference of 63%. Furthermore, the mean value per-cycle of each tooth is not 0, as shown in table 6.4 and fig. 6.14.

tooth	1_{st}	2_{nd}	3_{rd}	4_{th}	5_{th}	6_{th}
mean B_z	1.8 mT	5.1 mT	3.3 mT	-0.8 mT	-3.9 mT	-2.4 mT

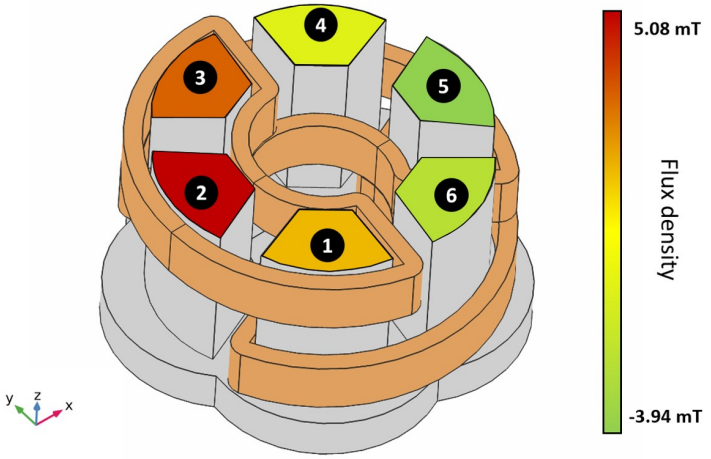

Figure 6.14: Mean $\mathbf{B}_z$ for one 50Hz cycle.

From these values we know that is impossible to have a resulting travelling field that is sinusoidal, as the mean value in each tooth is different from 0, and therefore their combination cannot have a mean value of 0 also. So, another way of evaluating the aspect of the travelling magnetic field at the surface is the radial distribution at the same instant. This distribution should be sinusoid-like and for this machine, 1 pair of poles, and a frequency of 50 Hz.

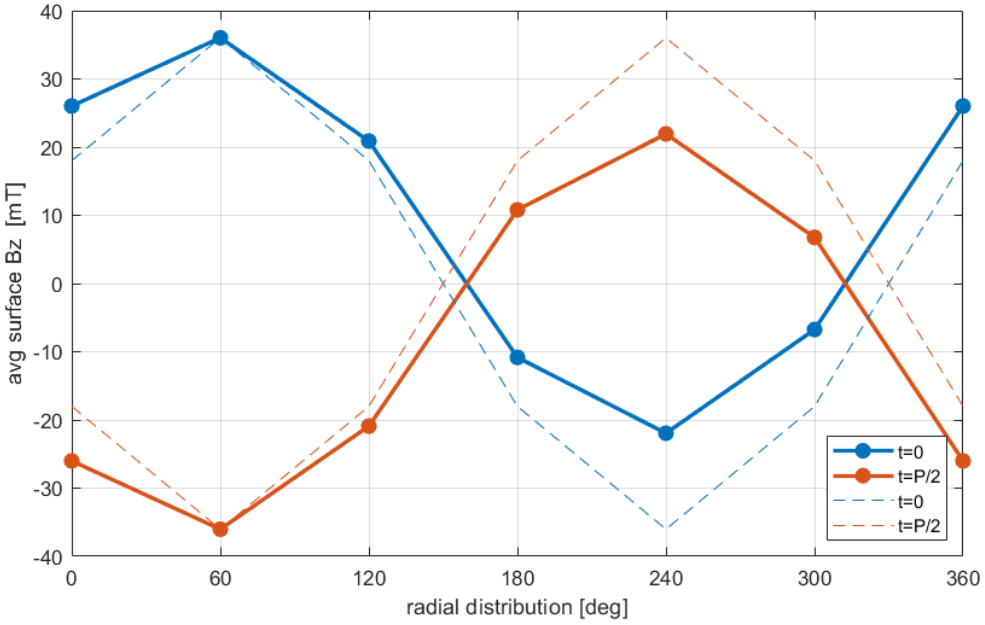

Figure 6.15: Resulting travelling magnetic field radial distribution, for t=0 and t=P/2.

The radial distribution of the field is plotted in fig. 6.15 for 2 instants, t=0 and t=P/2. The solid lines are the measured values from the simulations, and the dashed lines the expected sinusoidal signal. We easily observe the non-sinusoidal field distribution, with a higher absolute value in one side, and a lower in the opposite. This oscillation makes the field almost pulsating, instead of sinusoidal.

The normal circular distribution for an induction machine with 1 pair of poles should be equal to the dashed lines, where each tooth is 60 degrees apart. In this case, each tooth is surrounded by 1 or 2 coils, and their respective contribution to the teeth. In the graph the top coil middle tooth is represented at 60 degrees, when the current is the highest, 20 A; normally, the current in the other coils being 120 electrical degrees apart, should make the total field in each tooth a combination of the 3 currents, and therefore create a travelling wave at the top surface (air gap), equal to the dashed line. Instead, the behavior is quite different, as the absolute value at the maximum, 60 deg, does not repeat at the opposing side, it is much smaller, creating a field with and mean value different of zero.

One half-period later, the travelling wave should suffer a shift of 180 deg, with the same values equally spaced, in this case, mirrored in the vertical direction. Despite the waveform being mirrored vertically, it did not shift 180 deg, as each new value does not correspond to its original at t0. Now the mean value still remains different from 0, as its absolute value is equal to the previous, but with an opposing sign.

As the mean value is not 0, and the highest and lowest values are constantly changing in value, the resulting travelling magnetic wave in the air-gap is far from ideal; as it is non-sinusoidal and with an always changing mean value, it cannot be considered to be travelling at the expected velocity of 50 Hz like the electrical one. This results in a wave whose travelling velocity is unknown, and consequently a machine that does not have a synchronous speed of 3000 rpm, or 314 rad/s, which in turn will heavily impact the torque behavior of the machine at this speed, whose value should be 0.

6.6 RMM 1 cycle 0-3300 RPM

Having now the certainty of a cyclic behavior after half a period, several 1 cycle simulations were performed at different mechanical speeds, from 0 to 3300 rpm, and their respective mean torque values were calculated. Figure 6.16 plots the torque evolution in time for 0, 1000, 2000 and 2900 RPM.

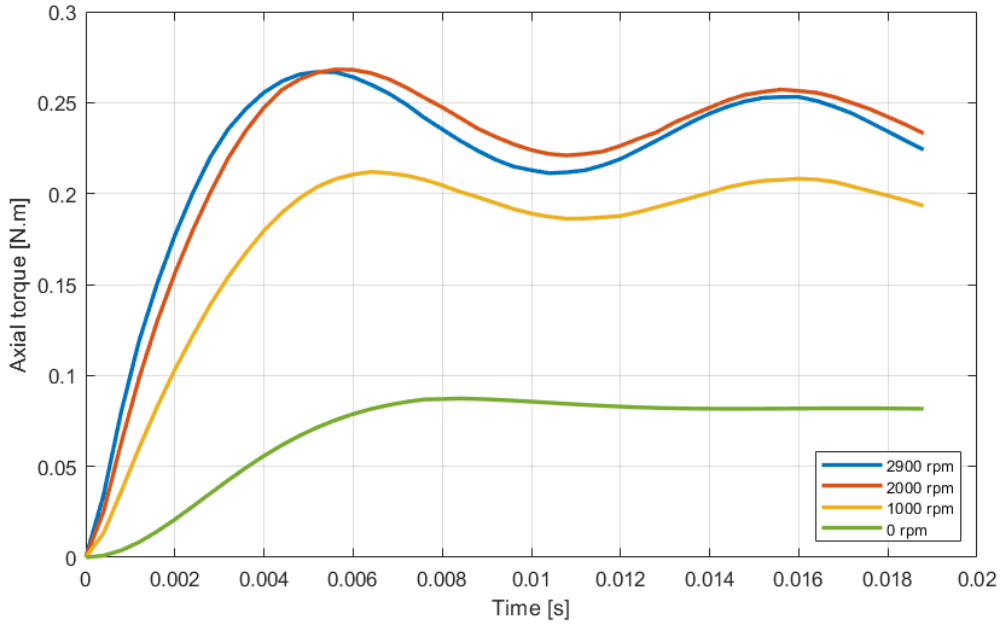

Figure 6.16: Torque evolution in time for 4 different speeds.

From the figure one can observe 4 different axial torque displayed in time, and the similarities in mean values for the 3 highest speeds. This a result of the machine poor magnetic capabilities as the magnetic field in the air-gap is so small the induced currents will in turn be small, and as a result the developed average mechanical torque does not surpass the 0.25 Nm at any speed. Finally, the torque/speed curve of the machine is plotted in fig. 6.17.

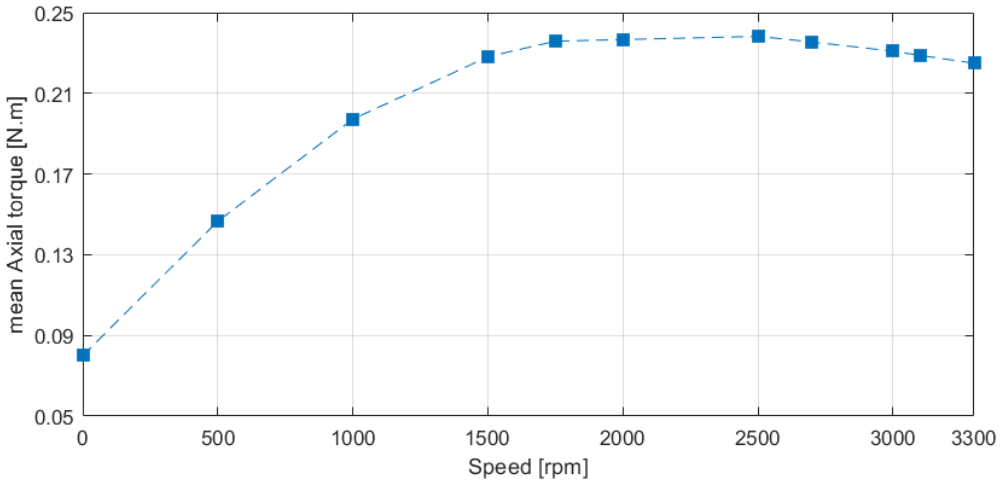

Figure 6.17: Torque/speed curve for 0-3300 rpm.

This figure now plots the torque/speed behavior of the machine, a very important measurement of functioning of any electrical machine. However, as these values were obtained with the RMM model, they cannot accurately depict the real behavior of the machine. So, they can only give us an idea of the order of magnitude of the torque, about 830 times smaller than the originally designed in [1], 208.35 Nm.

6.7 Current compensation

These inconsistencies in the magnetic field generated by the stator are a result of the coils' vertical displacement as their inductance vary so much, the field they generate when injected equal currents, 3-phase 20 A, cannot generate the same field at different heights. To overcome this difference without any physical modification, the 3 injected currents must be different in amplitude. Two different approaches were then made to calculate the new currents, one considering the inductance differences, and the other considering the differences in the measured flux at the teeth's surface. Both methods maintain the top coil current.

	Top coil	Middle coil	Bottom coil
coil inductance	1.33 mH	2.21 mH	3.17 mH
old current	20 A	20 A	20 A
new current	20 A	33.2 A	47.7 A

Table 6.4: Current compensation method 1 - inductance.

	Top coil	Middle coil	Bottom coil
max B_z (mean)	36 mT	25 mT	20 mT
old current	20 A	20 A	20 A
new current	20 A	28.5 A	36 A

Table 6.5: Current compensation method 2 - $\mathbf{B}_z$.

Now, 2 simulations were performed at the same velocity, 2900 rpm, each with one set of the currents, plotted in figs. 6.18 and 6.19. And from the figures it is evident now the B_z compensation method, 2nd, is superior to the 1st, where only the inductance differences were considered. In fig. 6.19 the amplitudes of the fluxes are much more similar between each other, with an amplitude average of 37.5 mT, a 34% increase of the original value, 28mT; and a max deviation of 10% from the average, instead of 18%. This results in a much more uniform resulting field, which will in turn generate fewer vibrations, and consequently a more efficient machine.

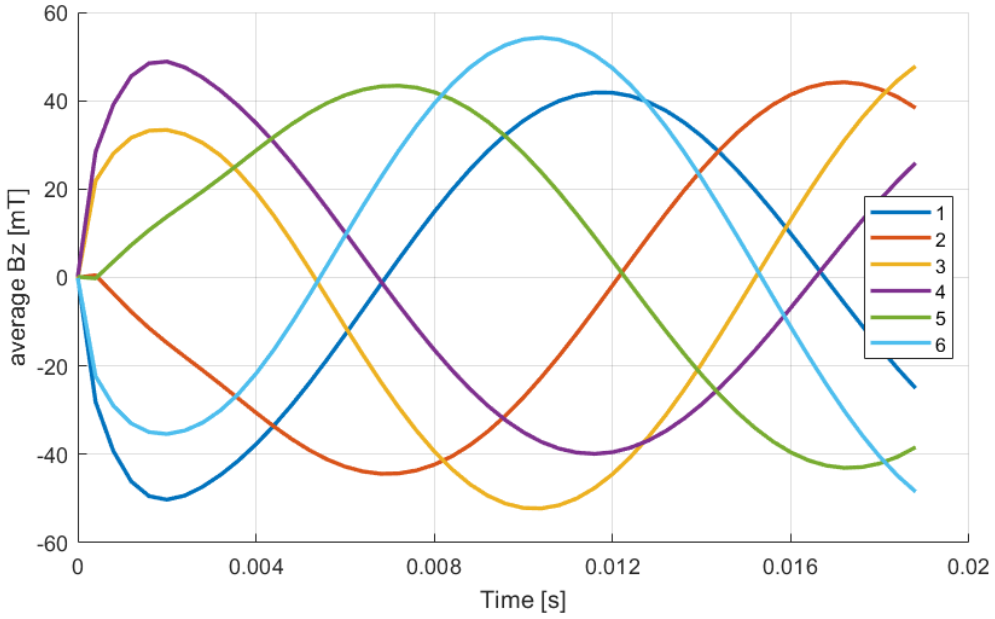

Figure 6.18: Current compensation 1st method - average $\mathbf{B}_z$ per tooth for one 50Hz cycle.

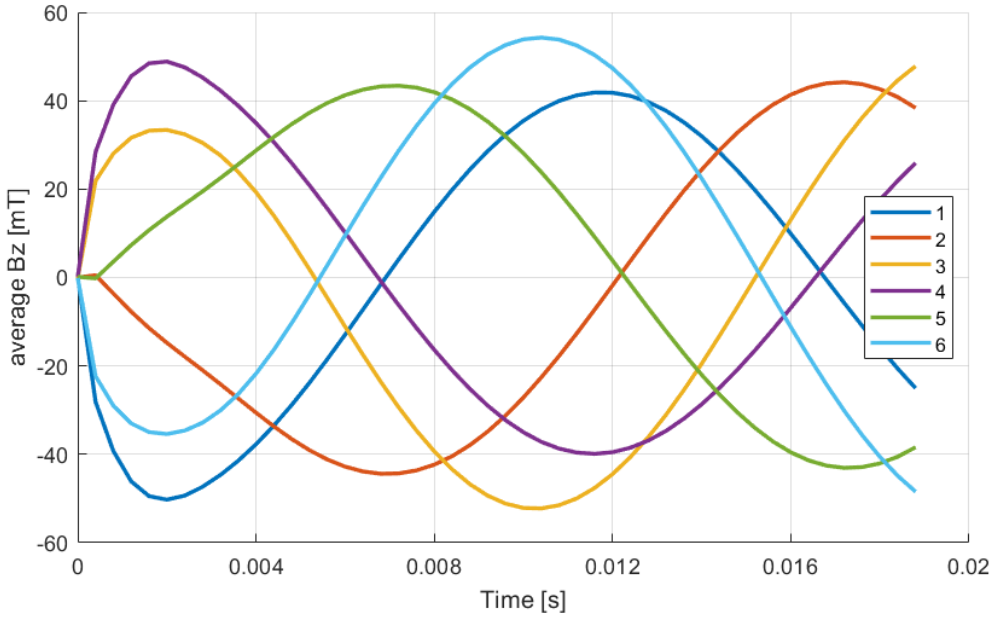

Figure 6.19: Current compensation 2nd method - average $\mathbf{B}_z$ per tooth for one 50Hz cycle.

6.8 Motor improvements

After all analysis performed on the motor, we know its weak components, from the stator material to the coils itself, there is a lot of room for improvements. Therefore, more tests were performed to simulate all possible alterations on the motor, all using the frequency domain model, with running times of a few minutes. The motor's components, stator, coils and rotor, were modified and then compared to the original.

6.8.1 Stator modifications

From the previous tests a poor magnetic performance from the stator is visible, with a relative permeability of 141, the developed fields by the stator will always be very low. This problem can also be related to the stator geometry itself, as magnetic leakage could also be the responsible for such low B values in the air-gap. To test this possible leakage the motor was simulated with the 50 Hz 3-phase 20 A currents, and the flux density as measured at 3 different heights, with slices in the middle of each coil, fig. 6.20.

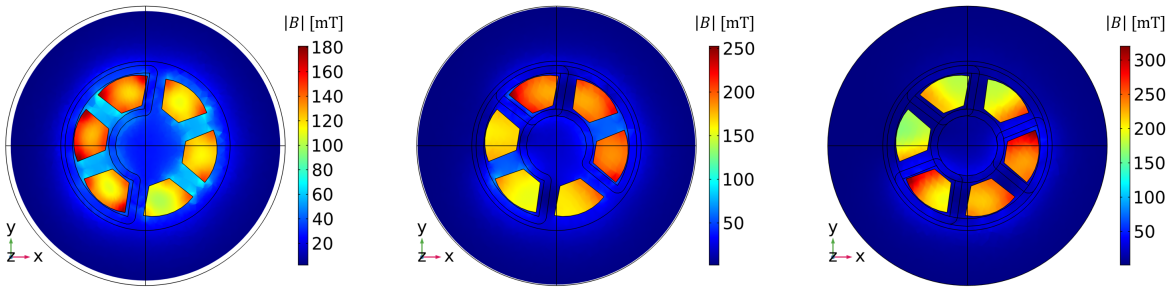

(a) h=top coil (b) h=middle coil (c) h=bottom coil

Figure 6.20: $|\mathbf{B}|$ cut view of each coil, (a) top, (b) middle, (c) bottom, middle height.

In figures 6.20 we observe much higher flux values inside the stator teeth, than in the air surrounding, where the values are very low in comparison. In the top coil slice, where the flux leakage is the highest in comparison with the maximum values, the flux in the air has a cyan color, $B_{\text{air}} < 70$ mT, whereas the flux inside the stator is the dark red, $B_{\text{stator}} < 180$ mT. In the other coils the flux in the air has similar values, however the flux in the teeth is much higher, with values surpassing 300 mT in the bottom coil, more than 4 times the leaked flux. From this we can conclude that despite a far from optimal coil design, the stator design itself does not cause much leakage, so there is no need to change the geometry of the stator in this case.

Now, with the current stator design validated, we know there is no major flux leakage lowering the available air-gap flux, so the poor magnetic capabilities must come from the material itself, more specifically the material's magnetic properties: the magnetic permeability, μ, and electrical conductivity, σ, with $\mu_{\text{r}} = 141$, and $\sigma_{\text{somaloy}} = 5000$ S/m. Although the conductivity is extremely low when compared with typical iron, whose conductivity is approx. $1.12 \cdot 10^7$ S/m, cannot overcome the stator's low permeability.

To overcome this low magnetic performance, 2 different materials were simulated for the stator: electrical steel and laminated electrical steel. These materials are typically used in electrical machines, both with identical magnetic permeabilities and differing only in electrical conductivity. The laminated steel is especially used in power transformers, where sheets of steel are stacked with insulating material in-between; This creates an easy path for the magnetic flux while creating a very difficult path for the electrical currents, as they are perpendicular to each other. This type of material is simulated through the use of a directional conductivity instead of an isotropic conductivity. 2 new FD simulations identical to section 6.1 were then performed and the blocked-rotor torque and vertical forces were compared to the original stator, table 6.6.

stator material	relative permeability	electrical conductivity	z-Force	axial Torque
Somaloy	141	isotropic 5000 S/m	5.6 N	0.099 Nm
electrical steel	5000	isotropic $1.12 \cdot 10^7$ S/m	3.23	0.022 Nm
laminated electrical steel	5000	x,z=$1.12 \cdot 10^7$ & y=0.1 S/m	5.34	0.073 Nm

Table 6.6: Stator core materials' properties.

Now we can compare the 3 materials with the axial torque, most relevant, and the vertical force on the rotor, less relevant, and from the 3 materials, the Somaloy stator is the best. From all materials it has the highest torque, 35% higher than the laminated iron stator, and with a vertical force only 5% higher. This is a result of the combination of both magnetic permeability and electrical conductivity, although the relative permeability is 35 times smaller, i.e. for the same magnetomotive force in the coils the generated flux is 35 times smaller for the Somaloy than the iron's, the conductivity in the iron is so much higher, 2000+ times, that even for a laminated stator the induced currents are so high the total flux is smaller; and consequently, the developed torque is smaller as well. This makes the Somaloy stator the best option between the 3 materials.

It is also relevant comparing both electrical steel materials and the importance of the lamination process, as in fact the raw material comprising both is the same, differing only in this process. In table 6.6 we compare both developed torques, and we easily conclude the impact of the lamination process, with the Torque from the laminated stator is 3 times higher than the non-laminated. This is a result of the reduction in induced currents in the stator teeth, normal to the vertical flux, z-axis, and therefore horizontal, x and y-axis. The conductivity in the laminated iron changes from an isotropic $1.12 \cdot 10^7$ S/m, to being $1.12 \cdot 10^7$ S/m in the x-axis and 0.1 S/m in the y-axis. This reduces the induced currents and therefore increases the total available vertical flux in the air-gap.

6.8.2 Stator coils modifications

After the stator possible modifications, which proved to be unnecessary, the next and probably the most relevant modification possible is in the coils. As seen in section 6.1.1, the magnetic field generated by the coils is not only very low, as a result of the low small number of turns, but also very uneven, due to different height positioning. So, new coils must be designed with both characteristics in mind: maximize magnetomotive force, coil number and current, and homogenize coil geometry.

The new coils, visible in fig. 6.21, are now 6 identical concentrated around each tooth, instead of 3, and for the same wire diameter can have as much as 150 turns, instead of 60. Each phase is now comprised of two opposing coils connected in series. These new coils, being wound tightly around each tooth have practically no leakage, and by being identical will in theory generate a perfectly distributed magnetic field and therefore a more balanced machine with a higher efficiency.

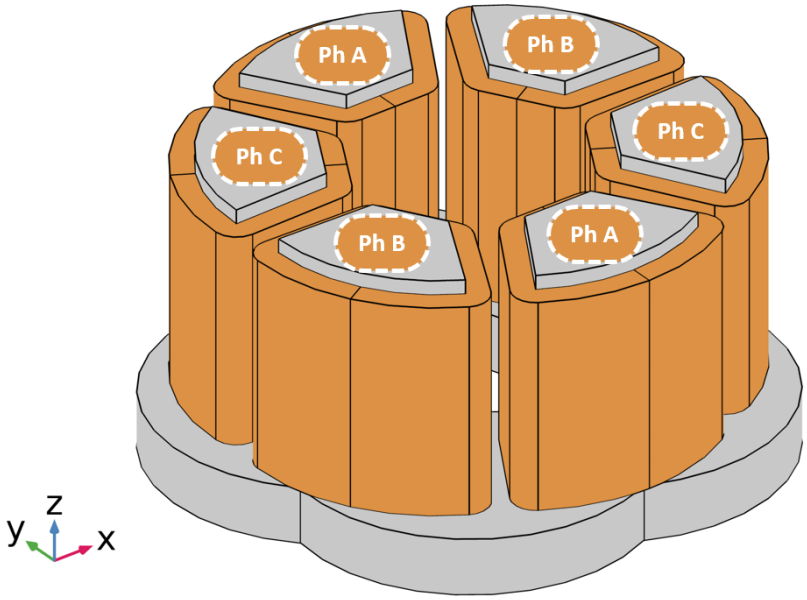

Figure 6.21: Stator with new concentrated coils.

Now with the new coils new simulations were performed, for 60 and 150 turns. The first simulation uses the same 50 Hz 3-phase 20 A currents for both coil designs, and the top view of the vertical flux is plotted in fig. 6.22.

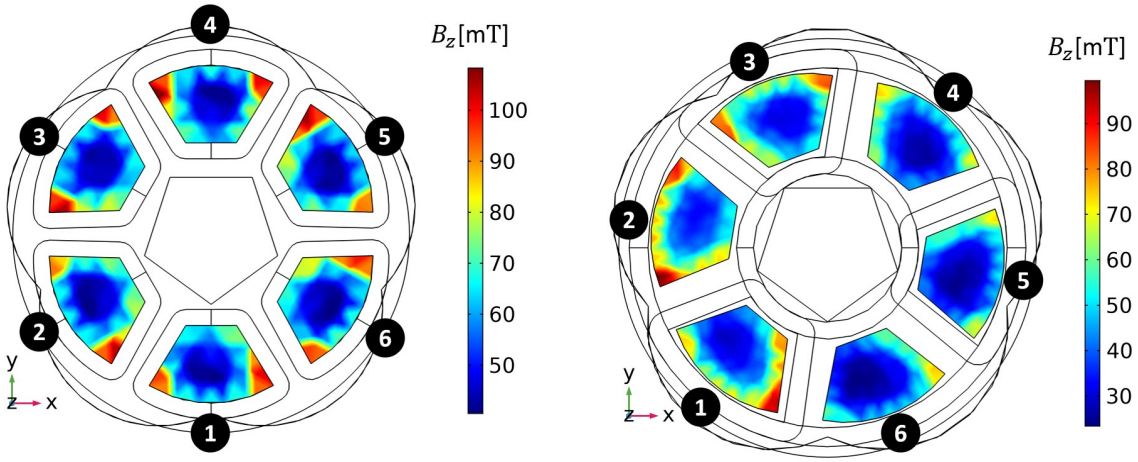

(a) new concentrated coils (b) original distributed coils

Figure 6.22: $|\mathbf{B}_z|$ top view for new (a) and original (b) coils.

From fig. 6.22 we can compare now both coil typologies, and easily observe the advantages of the new designed coils: the flux distribution in the stator surface is perfectly distributed between the teeth. This new distribution not only is more homogeneous than the original coil design, but also has a higher average flux per tooth, with all teeth having a similar higher penetration, visible in the outer corners of the teeth, with $B_z > 100$ mT in all teeth, instead of 90 mT in only 3. Figure 6.23 plots the total magnetic flux generated by each tooth for both coil designs.

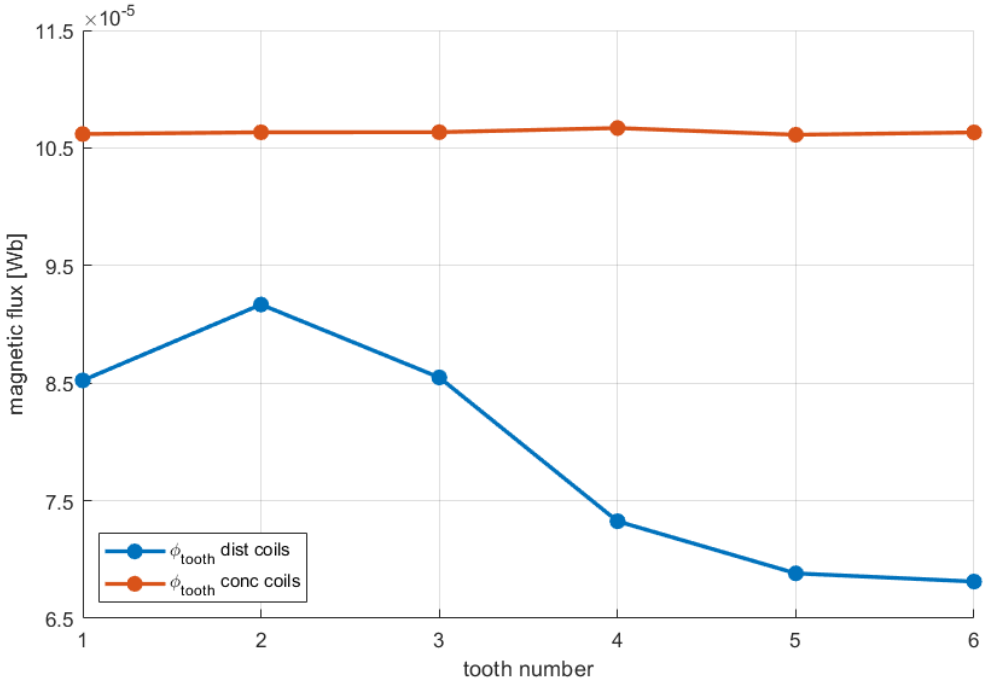

Figure 6.23: Total flux per tooth [Wb] - concentrated and original coils.

In fig. 6.23 we can now quantify how much better the new coil design is, with an almost exact flux distribution at the top of the stator, in orange, and a rather dispersed flux for the original coils, with a difference in amplitudes of 30%. Furthermore, the average total flux is 106 μWb for the concentrated coils, instead of 78.6 μWb for the distributed coils, a 35% increase. Another advantage of these coils is the maximum number of turns, that can be as high as 150, 2.5 times the original. fig. 6.24 plots the same as fig. 6.23, now with 150 turns concentrated coils, and table 6.7 compares the z-force and torque for 60 and 150 turns.

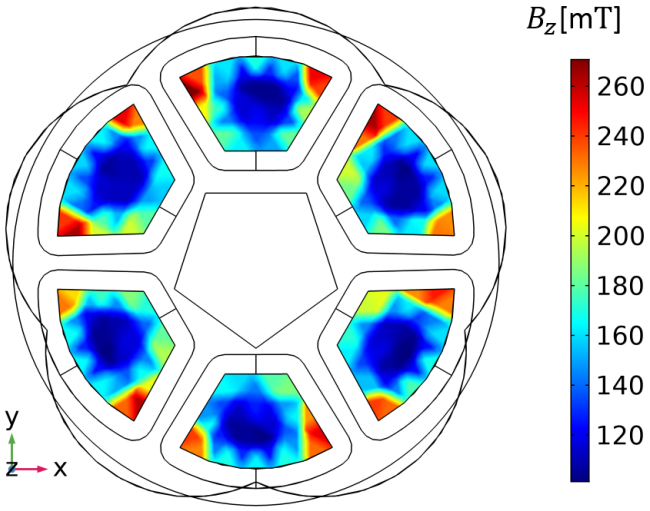

Figure 6.24: $|\mathbf{B_z}|$ top view for new 150 turns' coils.

number of turns	z-Force	axial Torque
60	8.34 N	0.1236 Nm
150	52.12 N	0.7725 Nm

Table 6.7: Rotor vertical force and axial torque for 60 and 150 turns' coils.

In fig. 6.24 we can see in the range of the scale of the flux density the values are approximately 2.5 times the ones from the 60 turns concentrated coils figure, fig. 6.23. This is consistent with the coil turns' ratio, and consequently one can relate the air-gap flux amplitudes with the number of turns. However, when relating both torque and vertical force in both 60 and 150 turns, one obtains a relation of 6.25, exactly the square of 2.5, the relation between coil turns. Section 6.8.2 shows both relations,

$$|B_z| \propto N_t \tag{6.9}$$

$$\tau \, , F_z \propto N_t^2. \tag{6.10}$$

With this new coil design in mind a new simulation was performed, like in section 6.8.2, where the new concentrated coils are compared with the previous, in different stator materials. The resulting axial torque and z-axis force on the stator for both coil typologies and stator materials are presented in table 6.8.

stator material	Coil topology	z-Force	axial Torque
Somaloy	distributed	5.6 N	0.099 Nm
	concentrated	8.34 N	**0.124 Nm**
Electrical steel	distributed	3.23 N	0.022 Nm
	concentrated	1.32 N	0.018 Nm
laminated electrical steel	distributed	5.34 N	0.073 Nm
	concentrated	8.76 N	**0.134 Nm**

Table 6.8: Rotor vertical force and axial torque for both coil configurations and different stator's core materials.

Now we can finally observe the "mechanical" influence of this new coil design, with the axial torque being the highest in both Somaloy and laminated iron stators. Consequently, this coil typology is the most appropriate for this machine: higher and better magnetic penetration, more uniform flux distribution, and finally a higher torque. Furthermore, this coil typology, by having the possibility to increase the number of turns, also has the potential to generate a higher axial torque.

In section 6.2 simulations, the electrical frequency of the motor was lowered to increase the magnetic flux generated by the coils, according to eq. (6.6). However, the output mechanical power is both a function of the output torque and the rotor velocity, so an increase in velocity, i.e. electrical frequency, causes an increase in the mechanical power. As a result, several simulations were run with a new frequency sweep, between 50 and 400 Hz. Figure 6.25 plots the total magnetic flux per tooth for both typologies, the starting axial torque and vertical force for both coil typologies are then plotted in fig. 6.26.

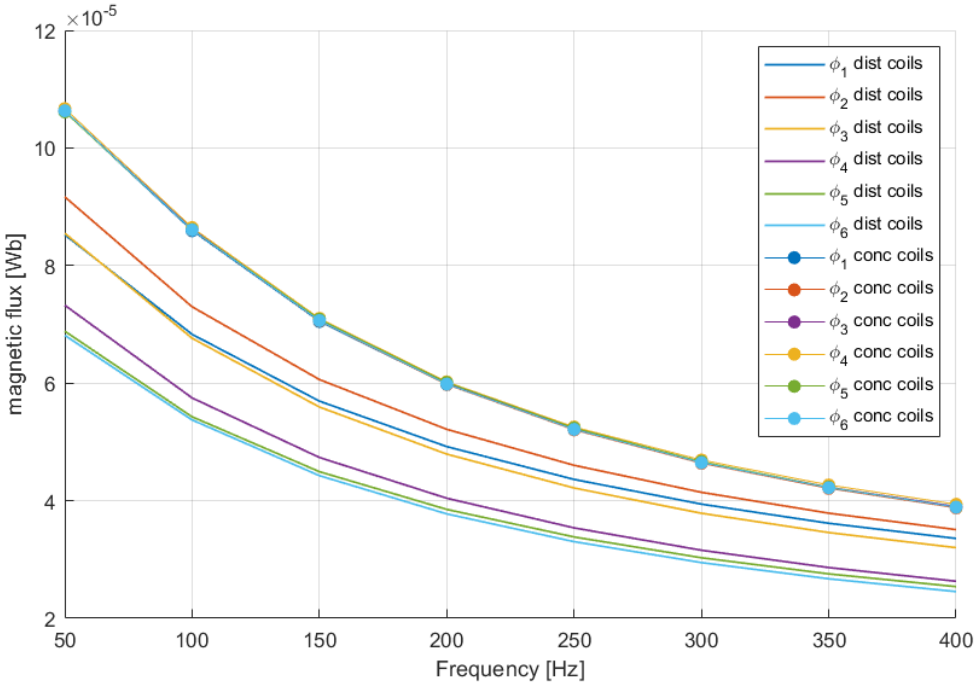

Figure 6.25: Magnetic flux per tooth for both coil typologies, 50-400 Hz.

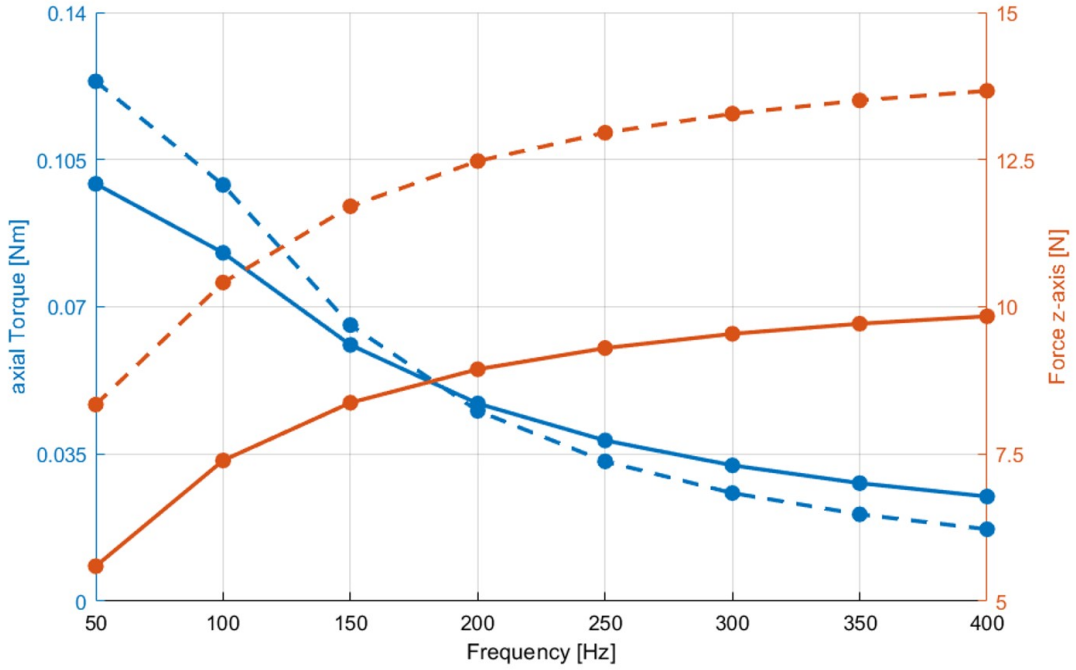

Figure 6.26: Starting torque and z-axis force for both coil typologies, 50-400 Hz.

From fig. 6.25 we verify the general decrease in flux with the increase in frequency while maintaining the phase voltages, which was expected from eq. (6.6). In the particular case of the distributed coils, besides the flux decrease, one can observe an approximation of the values with the frequency increase, and consequently a homogenization of the air-gap flux. This is a result of the *skin-effect* on the stator's teeth, where the induced currents inside the teeth penetration depth, i.e. the distance from the surface the current penetrates, decreases with the frequency, eq. (6.11). Effectively, an increase in frequency results in a decrease in the opposing induced currents, and consequently an increase in the total magnetic flux.

$$\delta = \sqrt{\frac{2\rho}{\omega\mu}}\ [m]. \tag{6.11}$$

The concentrated coils' flux also shows a similar behavior, they lower with the frequency increase, however there is no difference between the values in each tooth, they are practically the same and therefore overlap on the plot. Figure 6.26 plots the torque and vertical force evolution with the same frequency variation, and from it, we observe the decrease in the starting torque for the machine, consistent with the also decreasing flux. From these values alone, however, we cannot extrapolate the normal operating zone torque, and consequently cannot calculate the machine's output power. However, we can see from the vertical force evolution it increases alongside the frequency, which is undesired, as this force creates additional stresses on the machine on the axle and rotor supports.

Another important aspect of the coil design is their efficiency and, despite not being possible to calculate the power output of the motor, the input power is. So fig. 6.27 plots both the axial torque and the input electrical power for the motor with both coil typologies. Here we see an increase in input power alongside the frequency, the opposite of the torque. We can also observe a higher power input in the distributed coils than in the concentrated for the 2 first frequencies, 50 and 100 Hz; after these frequencies both torque and power input invert their trend and the concentrated coils become less efficient than the previous. In conclusion, for low frequencies the new coil design has a higher torque and lower power input than the original ones, but for higher frequencies this changes.

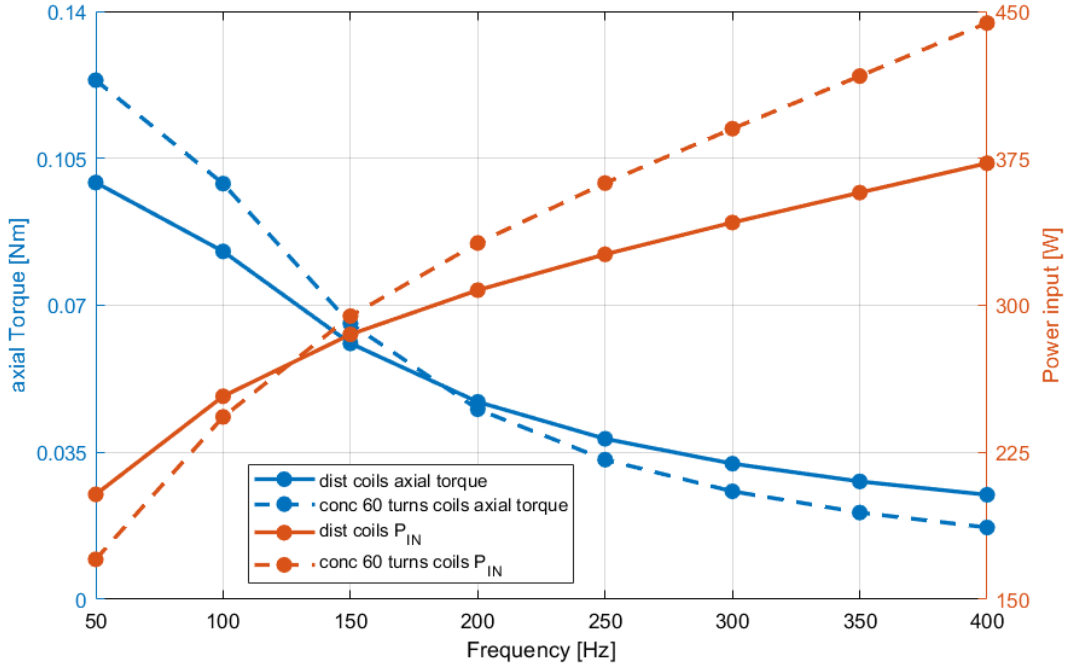

Figure 6.27: Rotor axial torque and power input for both coil typologies, 50-400 Hz.

6.8.3 Rotor modifications

With the stator and coils optimized, the final modifiable parameter is the rotor of the machine. This component is responsible for converting the air-gap flux into induced currents, and finally produce the mechanical force on the axle, delivering power to the load. This rotor can change both in material and geometry, and by fixating the diameter of the rotor, its thickness can vary. With a material like aluminum, where the magnetic permeability is very low, μ_r=1 the same as the air, it is transparent to the magnetic flux in the air-gap. For this reason, a higher thickness results in a higher flux penetration, and consequently a higher current density as well. Figure 6.28 plots the total magnetic flux on the stator surface and rotor current density for both coil typologies, at 50 Hz.

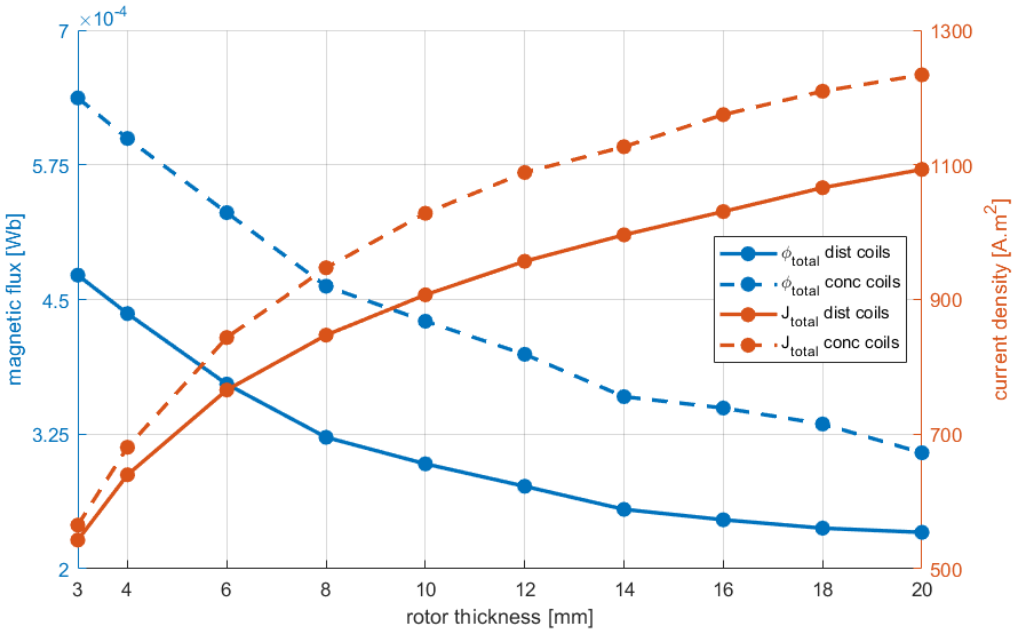

Figure 6.28: Total magnetic flux and rotor current density for both coil typologies, rotor 3-20 mm, 50 Hz.

Now we can observe that the current density in fact increases with the rotor thickness, which should be a good sign, however, there is a decrease in the total magnetic flux on the stator, and this is a result of the opposing magnetic field created by the induced currents; this new field opposes the stator-generated field and consequently reduces it. So, to optimize this rotor design, it is then necessary to also observe the resulting torque absolute value, fig. 6.29. As the figure shows the torque absolute value, after the 14 mm thickness the torque becomes ”negative”, which means the motor is now braking.

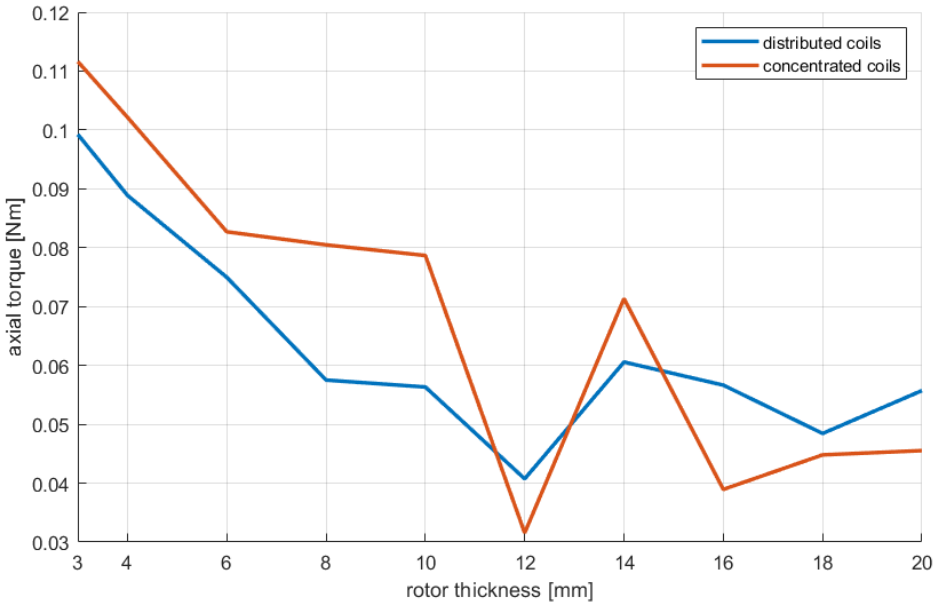

Figure 6.29: Starting torque norm for both coil typologies, rotor 3-20 mm, 50 Hz.

We now can see that the increase in current density does not compensate the total magnetic flux, and as a consequence the torque evolution is essentially negative. This means the optimal Aluminum rotor thickness for the machine is the already built, 3 mm. However, some new material could be used as to maximize the air-gap flux and current density relation. Table 6.9 shows the force and torque evolution for different rotor properties with the new coil design, as to maximize the generated flux. The varying properties are the rotor's electrical conductivity, σ_{ROTOR}, which relates to the induced current density on the rotor, and the rotor's relative magnetic permeability, $\mu_{\text{r, ROTOR}}$, whose value primarily affects the magnetic flux on the rotor.

σ [S/m]	μ_r	z-Force [N]	axial Torque [N*m]
0.1	1	4.011	$3.93 \cdot 10^{-3}$
	1500	-299.71	$84.99 \cdot 10^{-3}$
	3000	-324.35	$97.58 \cdot 10^{-3}$
	4500	-333.44	$102.29 \cdot 10^{-3}$
$5 \cdot 10^3$	1	4.0106	$3.95 \cdot 10^{-3}$
	1500	-299.71	$87.37 \cdot 10^{-3}$
	3000	-324.36	$100.25 \cdot 10^{-3}$
	4500	-333.44	$105.07 \cdot 10^{-3}$
$3.7 \cdot 10^7$	1	5.636	$92.18 \cdot 10^{-3}$
	1500	-22.126	$103.51 \cdot 10^{-3}$
	3000	-22.238	$102.81 \cdot 10^{-3}$
	4500	-22.273	$102.56 \cdot 10^{-3}$

Table 6.9: Rotor vertical force and axial torque for different rotor's properties with concentrated 60 turns coils.

With σ_{ROTOR} varying between 0.1 and $3.7 \cdot 10^7$ S/m, it simulates the conductivities of a laminated rotor and bulk aluminum, respectively; and $\mu_{\text{r,ROTOR}}$ values between 1 and 4500, the relative permeability of aluminum and electrical steel, we simulated a wide range of materials.

Firstly, when analyzing the z-Force data, we see that for a μ_r=1 the force is positive and relatively small, a repulsing force between the stator and the rotor. However, when $\mu_r >=$1500 this force becomes negative, i.e. attractive, and much higher for smaller conductivities. As the current density generated reaction field in the rotor is much smaller in comparison to stator generated field, and the magnetic permeability of the rotor is so high, the rotor acts as a perfect path for the magnetic fields to close themselves. And consequently, the flux density is much higher. For the highest conductivity, the vertical force is also attractive, however now one order of magnitude smaller, approx. 10 times smaller than those with smaller conductivities. This is a result of the opposing flux generated by the rotor's currents lowering the stator generated flux, and consequently lowering the total air-gap flux. The behavior is the same as for smaller conductivities, only with smaller values.

Finally, the torque behavior of the machine, the most important factor, is analyzed, and we can group these values in 2 different values, $4{\cdot}10^{-3}$ Nm, and $100{\cdot}10^{-3}$ Nm; the smaller torque occurs when μ_r =1 and $\sigma = \{0.1 \ ; \ 5000\}$, and the highest torque occurs in all other instances. This highest value, 0.1 Nm, is clearly a plateau of the machine, the motor cannot produce a higher torque with the available magnetic flux. This is expected as the flux density in the air-gap of the machine is much smaller when compared with similar size machines, whose air-gap flux density can be greater than 1 T. Whereas now with the new coil design, the flux density is smaller than 75 mT, so the torque limitations come from the low magnetic field, not the rotor. For this reason, a new simulation was done with the same rotor values, table 6.10, however with the 150 turns coils.

Now with the higher number of turns the rotor can generate much higher torque, with values higher than 0.6 Nm. These values are however 6.25 times the ones from the 60 turns simulations, as both are computed using the relative permeability of the material, not the effective B-H curve, and consequently saturation can never occur.

σ [S/m]	μ_r	z-Force [N]	axial Torque [N*m]
0.1	1	25.07	$24.55{\cdot}10^{-3}$
	1500	$-1.873{\cdot}10^{3}$	$531.17{\cdot}10^{-3}$
	3000	$-2.027{\cdot}10^{3}$	$609.88{\cdot}10^{-3}$
	4500	$-2.084{\cdot}10^{3}$	$639.30{\cdot}10^{-3}$
$5{\cdot}10^{3}$	1	25.07	$24.68{\cdot}10^{-3}$
	1500	$-1.873{\cdot}10^{3}$	$546.04{\cdot}10^{-3}$
	3000	$-2.027{\cdot}10^{3}$	$626.57{\cdot}10^{-3}$
	4500	$-2.084{\cdot}10^{3}$	$656.67{\cdot}10^{-3}$
$3.7{\cdot}10^{7}$	1	35.23	$576.12{\cdot}10^{-3}$
	1500	-138.29	$646.93{\cdot}10^{-3}$
	3000	-138.99	$642.57{\cdot}10^{-3}$
	4500	-139.21	$640.98{\cdot}10^{-3}$

Table 6.10: Rotor vertical force and axial torque for different rotor's properties with concentrated 150 turns coils.

Chapter 7

Thermal Experimental Results

This machine efficiency, as already proven, is very low when compared to “normal” induction machines, i.e. axial rotor machines, whose efficiency can be higher than 90%. As thermal losses are a big part of any electromechanical device, its analysis is of great importance. To analyze the thermal behavior of this machine, the rotor Joule losses were measured eq. (7.1), first in the laboratory and then with a FEM thermal study,

$$P_{Joule} = J \cdot E = \frac{J^2_{ind\,rotor}}{\sigma_{Al}} \tag{7.1}$$

7.1 Laboratory experiment

The setup of this experiment includes the full motor assembly, stator and rotor, the 3-phase excitation, a voltage meter, and a set of thermal probes and their respective multimeters for the measurement. An auxiliary fan was also utilized to cool the motor after the test. The data recording was done with a video capturing device; fig. 7.1 shows the experimental setup.

The total experiment lasted 31 minutes, and a cellphone recorded the data for all multimeters at the same time: three temperatures and one phase voltage; the latter being recorded for monitoring purposes. For an accurate measurement, the temperature at the rotor surface was measured in 2 opposing sides, T_1 and T_2, and T_3 the top-coil temperature, fig. 7.2.

Figure 7.1: Thermal lab experiment - setup.

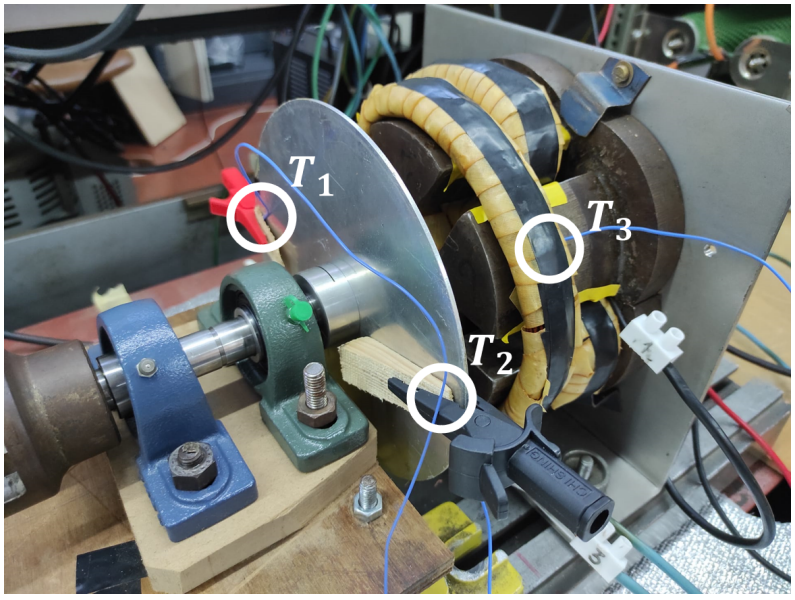

Figure 7.2: Thermal lab experiment - temperature probes detail.

The value T_3 is a control one, as the top-coil has the highest current, its temperature is critical for a normal operation as an overheating in the windings can create a short-circuit and damage them. The 3 used currents RMS values are presented in table 7.1, and the fig. 7.3 shows the thermal evolution of the coil and rotor, the last being the average between T_1 and T_2.

The test duration was 31 minutes to prevent an overheating in the coils, as the top-coil reached a temperature of 65° C. Despite the auxiliary fan could be used to cool the coils and therefore increase

coils' voltage	top coil current	middle coil current	bottom coil current
16.2 Vrms	15.25 Arms	13.16 Arms	12.62 Arms

Table 7.1: Thermal experiment 3-phase voltage and current.

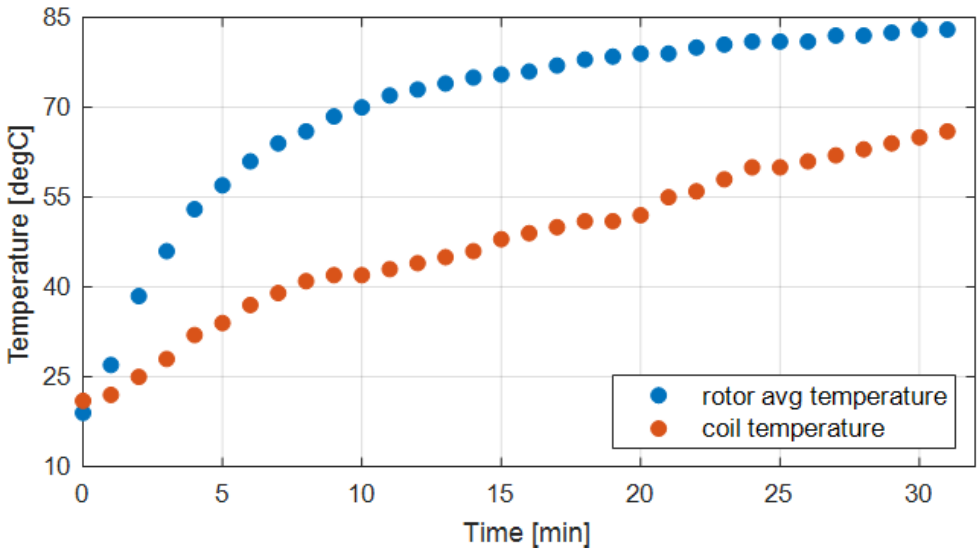

Figure 7.3: Top coil and rotor average temperature evolution.

the duration of the test, it was impossible to cool the coils without cooling the rotor.

The rotor's maximum achieved temperature is approximately 85° C for these currents, as it reaches saturation by the end of the experiment. However, as the rotor losses are a result of the induced current density, they are proportional to the input power: the higher the input power, the higher the losses and temperature, eq. (7.2)

$$\mathrm{T}_{rotor} =\propto P_{losses} =\propto P_{input} \tag{7.2}$$

7.2 FEM model simulation

Now a finite elements' simulation is developed to compare the thermal behavior in the rotor. As a time-dependent magnetic fields' simulation is very resource consuming, simulating the actual experiment, i.e. simulating the 3-phase excitation at 50Hz for 30 minutes, would require hundreds of computing hours. Therefore, a simplification is needed to circumvent this problem: separating the thermal and electromagnetic components of the model.

If we consider the rotor is blocked during the whole experiment, all its power is converted to Joule losses, and the coils' input power is constant, the rotor can be viewed as a heat source, Q_0, with a heat rate, P_0, equal to its electrical input power, eq. (7.3)

$$Q_0[Wm^{-3}] = \frac{P_{Joule}[W]}{V_{rotor}[m^3]} = \frac{P_{in}[W]}{V_{rotor}[m^3]} \tag{7.3}$$

7.2.1 Magnetic fields simulation

A blocked rotor frequency domain study is then performed, with a coil current excitation with the same values from the laboratory, table 7.1. After the study a volume integration of the electric power in the rotor is computed and the rotor volume is calculated.

P_{rotor} = 43 W
V_{rotor} = 94.25 cm^3

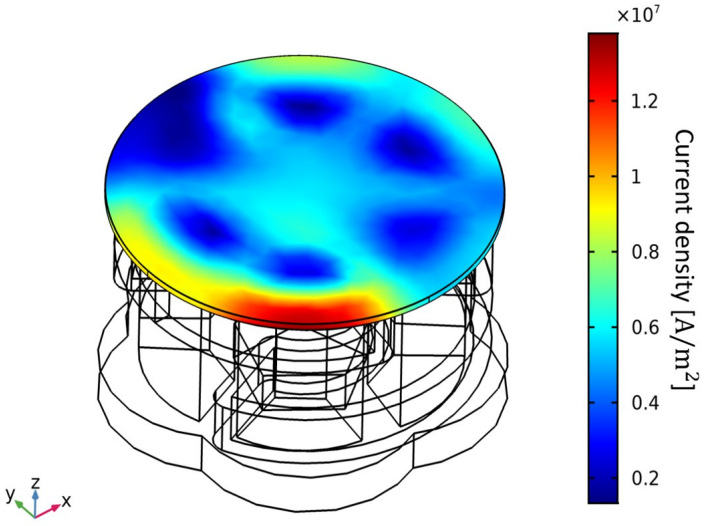

Figure 7.4: Rotor current density distribution at the thermal experiment.

In figure 7.4 it is possible to see the current density distribution in the rotor, and therefore the "power distribution" as well, as it is proportional to the square of $\mathbf{J}$. However, the first assumption mad before, where the rotor was considered a volume with a constant power output, the current density distribution is not homogeneous. This, as already explained in the Rotor Analysis section, is a result of the non-uniform flux density generated at the stator, due to very different coils' inductance. Because of this, the current output heat from the rotor won't either be homogeneous. This is the reason for the volume integration of the power losses, and not an average value, used to calculate the total power output.

7.2.2 Thermal model setup

Having now the power losses on the rotor, a new finite elements model is created, however now a thermal model, where the electromagnetic properties are neglected, and the thermal properties are the only studied. This model is then analyzed with a time dependent study with the same duration as the laboratory one.

This type of physics uses as expected a different set of conditions and equations to solve the different geometries. The first condition after the geometry and material selection, both as the other simulations, is the choice of physics used, in this case a Heat Transfer in Solids and Fluids, so that both thermal conductivity and convection occur, like in real life. The 4 created default conditions and their respective equations are: the solid and fluid domains, eq. (7.4) and eq. (7.5), the initial values, in Kelvin, and the thermal insulation, eq. (7.6),

$$\rho' C_p \frac{\partial \mathrm{T}}{\partial t} + \rho' C_p \mathbf{v} \cdot \nabla T + \nabla \cdot \mathbf{q} = Q \tag{7.4}$$

$$\mathbf{q} = -k \nabla \mathrm{T} \tag{7.5}$$

$$-\mathbf{n} \cdot \mathbf{q} = 0 \tag{7.6}$$

The solid and fluid equations, eq. (7.4) and eq. (7.6), model the heat transfer in their respective mediums and eq. (7.5) the heat conduction in media. The quantities ρ' , C_p, and k are the density, heat capacity and thermal conductivity of the materials; T the temperature in Kelvin and t is the time in seconds; **v** is the material velocity, **q** the conductive heat flux. The heat source Q, will be generated at the rotor. The initial value is the laboratory's air temperature, 18°C or 291.15 K.

As the thermal analysis main subject is the rotor, the stator coils were ignored and only the stator alloy and rotor were considered for the study; their materials' properties are listed in table 7.2 .

Material	Thermal conductivity	Heat capacity	Density
Aluminum	238 [W$\cdot m^{-1} \cdot K^{-1}$]	900 [J$\cdot kg^{-1} \cdot K^{-1}$]	2700 [kg$^{-1} \cdot m^{-3}$]
Soft composite	25 [W$\cdot m^{-1} \cdot K^{-1}$]	440 [J$\cdot kg^{-1} \cdot K^{-1}$]	7570 [kg$^{-1} \cdot m^{-3}$]

Table 7.2: FEM thermal model material's properties.

The medium involving the geometry is an 800 mm radius sphere comprised of air, however its properties are a function of the temperature and therefore are not a single value. These properties are plotted in fig. 7.5.

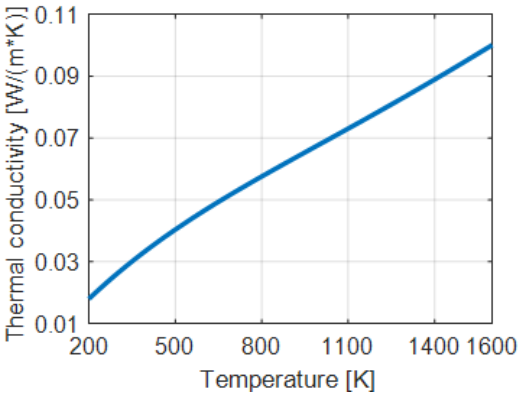

(a) Air thermal conductivity

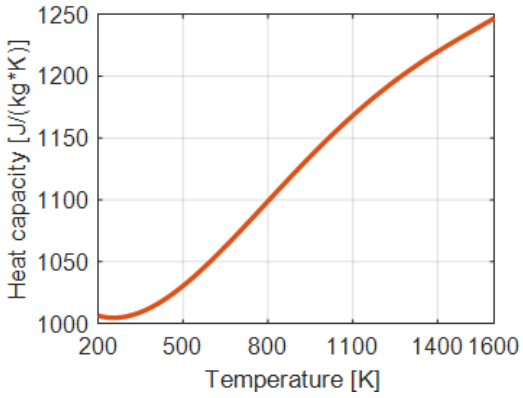

(b) Air heat capacity

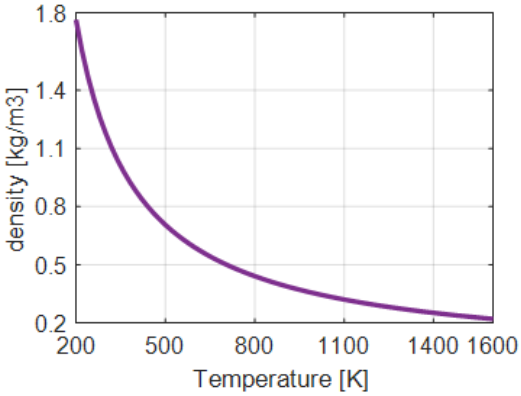

(c) Air density

Figure 7.5: Air thermal properties at 1 atm

7.2.3 Thermal simulation

Having now an assembly with 2 solids, the stator and the rotor, and a fluid, air, surrounding the geometry, a simulation is run, where the rotor is set as a heat source with an output of **43 W**. The figure show the first and last time step, t_0 and t_{31}, the same duration as the lab experiment, 31 minutes.

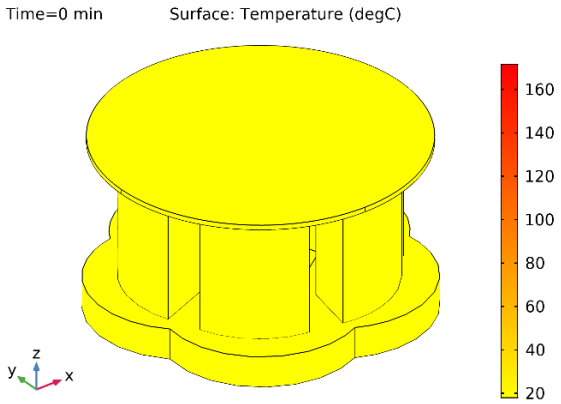

(a) t=0 min

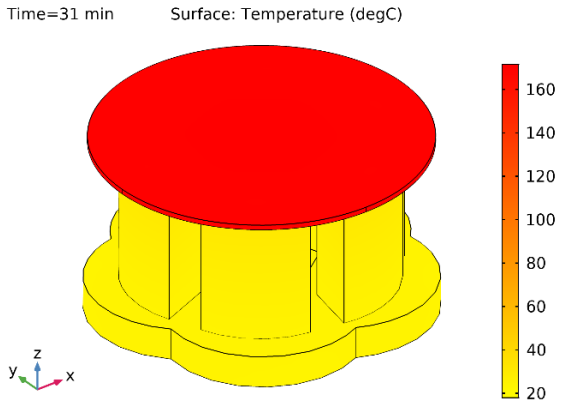

(b) t=31 min

Figure 7.6: Motor surface temperature at t=0 and 31 minutes.

From fig. 7.6 it is visible the disparity of values in comparison with the real final temperature of 84° C. The source of this disparity is connected to the geometry itself, as the rotor is considered to be floating above the stator, with no physical connections; therefore, all the heat is used to increase its temperature and the stator's. However, the final temperature on the stator surface is of 34° C, much lower than the rotor's, above 160° C. This means most of the energy is used to solely increase the rotor's temperature, thus a more accurate model is needed. This new model, fig. 7.7 considers both coupling pieces **(1,4)**, the bearings **(2,3)**, and the axle **(5)**, all with equivalent mass and volume as the real components.

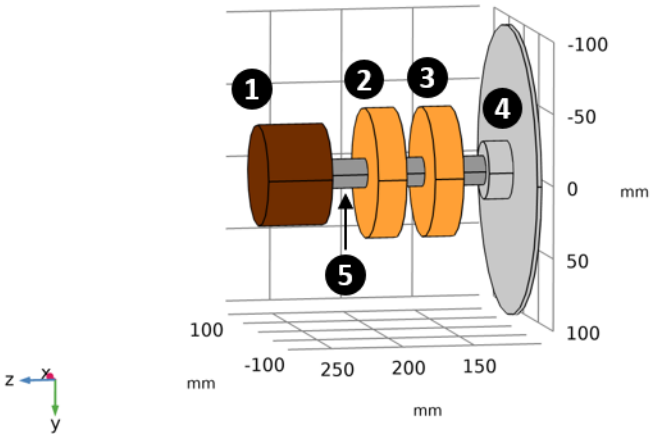

Figure 7.7: Complete FEM axle.

Besides this correction, the previous model did not consider the temperature effect on the conductivities of the coils and the rotor. However, as we know these will lower with the increase in temperature, new conductivities were calculated considering the final recorded temperature of 83°C, using the temperature coefficient, α, eq. (7.7) and eq. (7.8), of the materials

$$\alpha'(\mathrm{T}) = \frac{1}{R(\mathrm{T}_0)} \cdot \frac{\Delta R}{\Delta \mathrm{T}} \tag{7.7}$$

$$\alpha'_{Cu} = \alpha'_{Al} = 3.9 \cdot 10^{-3}[K^{-1}]. \tag{7.8}$$

With a temperature difference of 65°C, ΔT and $R(T_0)$ the reference resistance for the materials, the new conductivities of both materials are calculated, and a new rotor power is computed; table 7.3 compares the new values with the previous.

	$T=T_{ref}=20$ °C		**$T=T_{lab}=84$ °C**
copper conductivity	$5.998 \cdot 10^7$ S/m	$\rightarrow$	$4.815 \cdot 10^7$ S/m
aluminum conductivity	$3.774 \cdot 10^7$ S/m	$\rightarrow$	$3.030 \cdot 10^7$ S/m
rotor power losses	43 W	$\rightarrow$	37 W

Table 7.3: Electrical conductivities' variation with temperature.

Now, with a more realistic model geometry and power loss, several simulations were run for the optimization of the equivalent bearings position and material. The table 7.4 shows the chosen equivalent material properties for the axle, bearings, and end-coupling piece.

Material	Thermal conductivity	Heat capacity	Density
Stainless-steel	73 [W$\cdot m^{-1} \cdot K^{-1}$]	502 [J$\cdot kg^{-1} \cdot K^{-1}$]	7870 [kg^{-1} $\cdot m^{-3}$]

Table 7.4: Axial bearings thermal properties.

The final simulation was then run with the new axle and power, and the rotor's average surface temperature was plotted for the same time steps as the experimental. The fig. 7.8 shows the surface temperature distribution of the full assembly at the last time step, and fig. 7.9 compares both experimental and simulated rotor's temperatures.

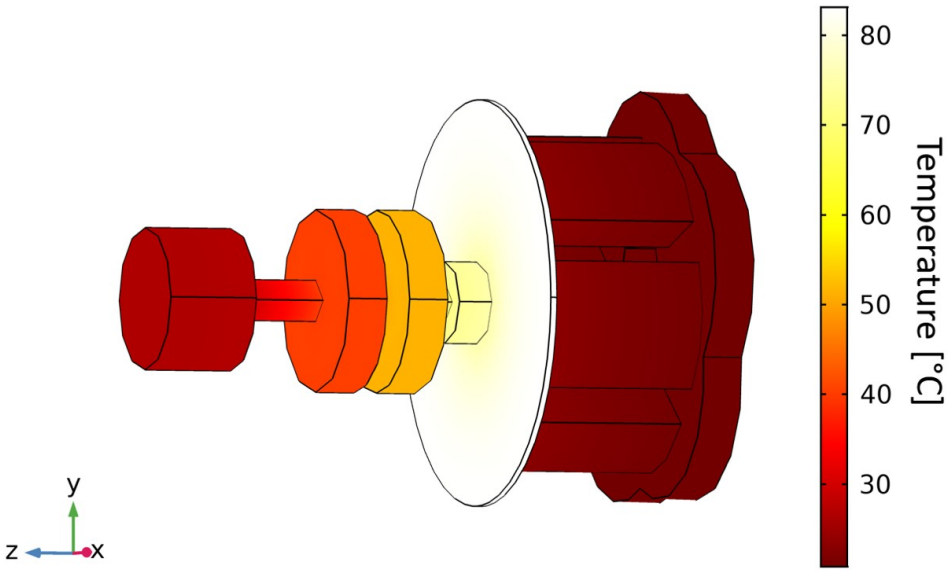

Figure 7.8: FEM simulation complete motor final temperature.

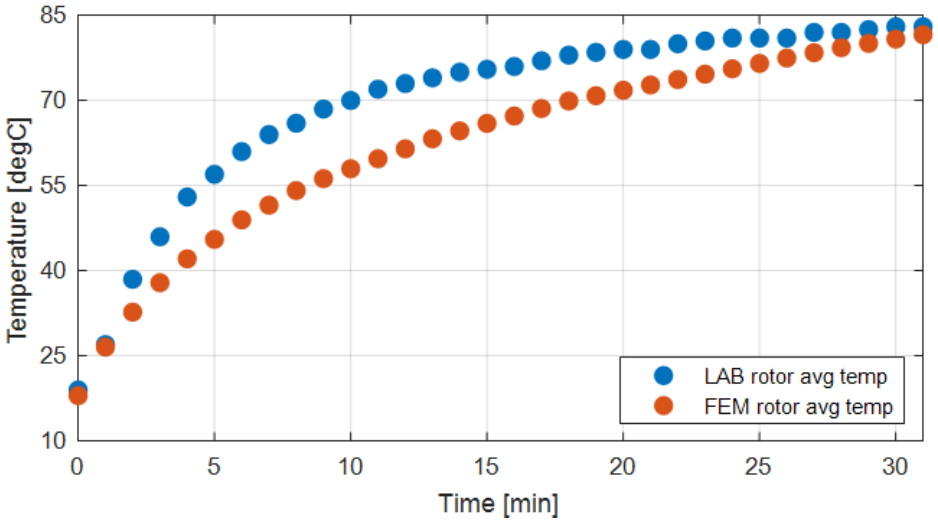

Figure 7.9: Experimental and simulated rotor temperature evolution.

7.3 Thermal Results comparison

From the 2 datasets one can easily observe that despite having very similar final temperatures, the curve aspect is different, as the experimental temperature at the rotor surface practically achieved saturation by the end of the experiment, which is another reason for the duration of it, and the simulated one did not. In fact, even with 2+ hours of simulated time, the temperature had not settled.

This disparity in results is a consequence of several differences between the real and simulated model. Firstly, and most relevant, is the assumption of the rotor as a continuous and homogeneous heat source with no decrease in power. In reality this is not true as the increase in temperature and material fatigue causes a lowering not only in the input electrical power of the stator, but also in the power transfer between stator and rotor. In reality the rotor temperature is an image of its power losses, which in turn are a result of the induced current by the stator input magnetic energy. Unlike the FEM where the rotor is considered a perfect heat source volume.

Secondly, the measurement of the power losses in the rotor, that in reality are surely different from the measured power in the FEM model, as there is no physical way to measure this total power, as it is transformed not only in heat, but also in torque, noise, and vibrations.
Thirdly, the materials' properties were assumed and approximated, as there was no possible way to measure them, as their measurement is done in specialized laboratories.

Finally, the testing equipment errors, as temperatures were measured with non-calibrated thermal probes and multimeters instead of precise thermometers; furthermore, the temperature at the laboratory was measured in 2 different points on the rotor's surface without a perfect thermal bond between the equipment, and in the FEM it was calculated as an average of 408 different points.

Chapter 8

Conclusions

The stator core of the induction machine, the most relevant component of this motor was characterized, both experimental and simulation wise. This allowed a more accurate modeling and understanding of the magnetic behavior of the soft core material.

With this characterization a new FEM model was created, much more accurate than before. This model considered the real materials and properties of the machine. After it, the modelled was validated, new types of studies were developed and compared, and new simulations were run. The machine's electromagnetic properties were mapped and its behavior understood. The full functioning principles of the machine were learned and its flaws discovered. This led to new simulations where the machine's main components, its stator, stator coils and rotor, were modified. These modifications took advantage of the existing components, optimized them, and ultimately improved its overall functioning and efficiency. The final form of the machine considered the initial stator core of the machine, as no modifications proved a significant improvement; the stator coils were completely redesigned, and the new set of 6 coils performs much better than the original; the rotor geometry needed no modifications, however a new material would bring some improvements.
Due to the global pandemic no more laboratory work was possible, and none of the improvements on the machine could be tested.

The final model of the machine regarded its thermal behavior. The machine was tested in the laboratory and with this data a thermal model was created. The model was then adjusted and finally compared with the physical behavior. Ultimately the thermal model did not prove itself very accurate due to its complexity.

8.1 Future Work

Having now an accurate simulation model of the electrical machine and a new optimized design created, several routes for future work are created.

The first route considers the construction of the new set of coils on the current motor and the testing of the same. This would further validate the FEM model and some additional improvements could arise from this work, and ultimately, a better, more efficient machine.

The other route regards solely the electromagnetic simulations. The work until here developed could serve as a blueprint to the 3D simulation of different machines. Not only the existing models could be optimized, and with a higher computing capacity new, more complex and realistic models could be developed.

References

[1] J. D. T. Guilherme. Electromagnetic design of a single-sided disk-rotor induction motor for electric propulsion. Master's thesis, Instituto Superior Técnico, 2017.

[2] Ieee spectrum website, protean electric's in-wheel motor. URL `https://spectrum.ieee.org/transportation/advanced-cars/protean-electrics-inwheel-motors-could-make-evs-more-efficient`.

[3] F. A. C. Fernandes. Design optimization of a single-sided disk-rotor induction motor for the fst in-wheel traction. Master's thesis, Instituto Superior Técnico, 2019.

[4] J. A. E. Fitzgerald, Charles Kingsley and S. D. Umans. *Electric Machinery*. McGraw-Hill, 6^{nd} edition, 2003. ISBN:0-07-366009-4.

[5] S. A. Poitout. Modelização de um sistema de trasnporte de fluidos por forças electromagnéticas. Master's thesis, Instituto Superior Técnico, 2005.

[6] J. A. B. Faria. *Electromagnetic Foundations of Electrical Engineering*. John Wiley Sons, 1^{st} edition, 2008. ISBN:978-0-470-72709-6.

[7] J. R. M. Herbert H. Woodson. *Electromechanical Dynamics, Part. I: Discrete Systems*. John Wiley Sons, Inc., 1^{st} edition, 1968. ISBN:978-0471959854.

[8] Electrical academia website, properties of magnetic materials. URL `https://electricalacademia.com/electromagnetism/properties-magnetic-materials/`.

[9] O. B. Gerhard Paoli and G. Buchgraber. Complex representation in nonlinear time harmonic eddy current problems. *IEEE TRANSACTIONS ON MAGNETICS*, 1998.

[10] G. R. Freire. Distribution transformer incipient fault automatic detection and monitoring. Master's thesis, Instituto Superior Técnico, 2020.